이학박사 학위논문

Topological Band Engineering with Neutral Ytterbium Fermions in Optical lattices

광격자 내 중성 이터븀 원자를 이용한 위상 띠 연구

2019년 2월

서울대학교 대학원

물리 · 천문 학부

한 정 호

Topological Band Engineering with Neutral Ytterbium Fermions in Optical lattices

광격자 내 중성 이터븀 원자를 이용한 위상 띠 연구

지도교수 신 용 일

이 논문을 이학박사 학위 논문으로 제출함

2018년 12월

서울대학교 대학원

물리 · 천문 학부

한 정 호

한정호의 박사 학위 논문을 인준함

2018년 12월

위 원 장	제 원 호	
부위원장	신 용 일	
위 원	강 병 남	
위 원	안 경 원	
위 원	최 재 윤	

Topological Band Engineering with Neutral Ytterbium Fermions in Optical lattices

by

Jeong Ho Han, B.S.

Dissertation

Presented to the Faculty of the Graduate School of

Seoul National University

in Partial Fulfillment

of the Requirements

for the Degree of

Doctor of Philosophy

Seoul National University

February 2019

Abstract

Topological Band Engineering with Neutral Ytterbium Fermions in Optical lattices

Jeong Ho Han
Department of Physics and Astronomy
The Graduate School
Seoul National University

Topology is a mathematical property that classifies a system's geometry and is preserved under continuous deformations. One famous example is a Möbius strip which forms a closed belt with a single twist. No continous deformation cannot remove such twist without cutting the belt. Here, the number of twists is called "topological invariant" which characterizes the topological order of a system. Recently, topology becomes an important concept in physics, ranging from cosmology to condensed matters. Especially, for electrons in solids, a Bloch band may have nonvanishing topological invariant which cannot be altered without closing the band energy gaps, stabilizing the phase. Strikingly, the topological nature enriches their exotic physical properties insensitive to microscopic details and robust against adiabatic parameter change; therefore, topological matters become candidates for novel materials. Since the discovery of integer quantum Hall effect, the idea has been widely studied over the past decades.

Quantum gases provide a nice testbed for simulating these model Hamiltonians under a well-isolated and defect-free environment with high tunability. To study the topological matter, we have developed an apparatus, which generates a degenerate fermi gas (DFG) of ^{173}Yb atoms of $T/T_{\mathrm{F}} = 0.1$ in bichromatic

crossed dipole trap within 25 s. The fermionic ytterbium, which is a heavy alkaline-earth-like element, provides favorable conditions to produce artificial gauge potentials using Raman two-photon scheme. As a first study, momentum-resolved Raman spectrum of a spin-polarized sample is measured. At certain experimental conditions, double resonance of Raman transitions is observed and the spectrum shows a doublet splitting similar to the Autler-Townes effect.

A good starting point to study the topological matter is Harper-Hofstadter (HH) Hamiltonian which describes the motion of a charged particle in a square lattice under the perpendicular magnetic field. To address HH Hamiltonian, a synthetic three-leg Hall tube is realized with ^{173}Yb in one-dimensional (1D) optical lattice using cyclic Raman couplings for commensurate flux. In synthetic dimension frame, this is equivalent to the spinless fermions in 2D HH Hamiltonian with periodic boundary condition. As boundary condition evolves from periodic to open, the Hall tube system exhibits either topological or trivial phase. Using quench dynamics, the band structure of the Hall tube system is investigated, where a critical point of band gap closing coincides with a topological phase transition predicted for the Hall tube system.

A very frontier of topological physics is the effect of interactions on the topological systems. To extend our research to include interactions, the inter-atomic potential is investigated via photoassociation (PA) spectroscopy on a DFG of ^{173}Yb near the dissociation limit using the intercombination line. The atom-loss spectrum of 80 PA resonances is measured for a spectral range down to -1 GHz with respect to the $F = 5/2 \rightarrow F' = 7/2$ atomic resonance. To obtain additional information on the excited molecular states, Zeeman effect and atom-loss rate of the PA resonances near -0.8 GHz are examined, where the quantum number of each peak is discovered using various spin mixture samples.

Contents

vi

List of Figures

ix

Chapter 1

Introduction

1.1 Quantum simulation with ultracold atoms

The realization of Bose-Einstein condensation (BEC) [1, 2] and of Fermi degeneracy [3–5] has opened a new chapter in atomic and molecular physics as well as condensed matter field [6]. This new type of matter offers a clean and nice testbed for exploring various quantum phenomena [7–9]. In particular, the high degree of controllability allows us to manipulate the physical properties in extreme regime which are hardly achievable in conventional solids. For example, the superfluid-to-Mott insulator transition has been observed in the three-dimensional (3D) optical lattices [10]. The external potential trapping the atoms can be modified to be shaped like a box [11] or even to create random disorders [12]. Also, the ability to change the dimensionality provides a platform for studying BKT physics [13, 14] and dimensional crossover [15]. Furthermore, interatomic interaction strength can be tuned via Feshbach resonance [16, 17] to explore BEC-BCS crossover [18–20]. Finally, an artificial gauge potential [21, 22]

has been generated to impart effective electric or magnetic field on the neutral atoms [23]. This artificial solid is fully described by a simple Hamiltonian which can be detected by direct imaging the wavefunction of the atomic cloud.

In addressing important problems such as high-T_c superconductivity, the required computational power increases exponentially with the number of its constituents. Therefore, the numerical approach using classical computers are limited even with the small number of constituents. As an alternative, in 1980s, R. Feynmann proposed a concept of quantum simulator as a primitive quantum computer. Instead of solving the given Hamiltonian, one can generate the effective Hamiltonian in the experimental systems [24] and study the toy model via directly "simulating" with the quantum toolbox. This concept is called an analog quantum simulator.

The state-of-art cold atom experiment is one of the promising candidate for realizing the Feynmann's quantum simulator. Recent advances in cold atom experiments reached at the level of technique of detecting [25–28] and manipulating [29] in a single-atom level. In spirit of Feynmann's proposal, the cold atom experiments become a toolbox embracing the condensed matter system of interest, allowing to probe otherwise inaccessible physical quantities. For instance, the cold atom experiments provide an artificially generated system which does not exist in our nature [30]. Furthermore, beyond atomic systems, the cold molecules are created near the quantum degeneracy to explore richer physics with large dipolar interactions [31–35]. It is also worth to mention the realiztion of optical tweezers (*Nobel prize 2018*!) for studying quantum information science and engineering applications [36].

This dissertation is mainly focused on engineering an artificial gauge potential in the cold atomic cloud. The artificial gauge potential is created

using Raman coupling scheme and exert a strong magnetic field on the cold atom sample. Together with 3D optical lattices, I studied synthetic material under this strong magnetic field, which reveals exotic quantum phases and nontrivial band topology. Since the electrons in real solids have fermionic statistics, I employ fermionic 173 ytterbium atoms. Fortunately, the fermionic ytterbium atoms have a suitable atomic energy levels to create such artificial gauge potentials.

In this chapter, I will describe basic principles of quantum degenerate Fermi gas in a harmonic potential and of optical lattices. A brief introduction on the topological band theory is also discussed.

1.2 Quantum statistics

Most of physical systems involve a number of particles of the same species. All these particles have same mass, charge, and spin. In classical mechanics, the concept of identical particles has been received less attention since the the particles are *practically* distinguishable. Since the measurement does not affect the classical system, one can label a specific particle by observing its physical quantity, for example, a trajectory. This trajectory identifies each particle in classical mechanics, making identical particles distinguishable.

In quantum mechanics, the identical particles are *indistinguishable*. It is neither impossible to label a specific particle nor to follow the trajectory of a particle. As a result, a remarkable consequence arises due to the quantum statistics in the system of identical particles.

Consider a Hamiltonian of two indistinguishable particles, say $\hat{H}_{1,2} = \hat{H}_{2,1}$ in 3D. A permutation operator $\hat{P}_{1,2}$, which swaps the two particles, does not affect the system. Therefore, $\hat{P}_{1,2}$ commutes with the Hamiltonian of the system

and is a constant of motion. Since interchanging the particles twice results in the Hamiltonian invariant, the total wavefunction $|\psi_{1,2}\rangle$ of the system has,

$$\hat{P}_{1,2}^2|\psi_{1,2}\rangle = p^2|\psi_{1,2}\rangle = |\psi_{1,2}\rangle, \tag{1.1}$$

which shows the eigenvalue of the permutation operator $p = \pm 1$. This eigenvalue is specified together with other eigenvalues λ of the Hamiltonian as $\psi_{p,\lambda}$. This is also true for an arbitrary observable $A_{1,2}$, and the system is invariant under the exchange of the two particles. As a result,

$$\langle\psi_{p,\lambda}|A|\psi_{p',\lambda}\rangle = 0 \quad \text{for} \quad p \neq p'. \tag{1.2}$$

Here, the two states form $|\psi_{p,\lambda}\rangle = \frac{1}{\sqrt{2}}(|\phi_{1,\lambda}\rangle_1|\phi_{2,\lambda}\rangle_2 \pm |\phi_{2,\lambda}\rangle_1|\phi_{1,\lambda}\rangle_2)$, where $\{|\phi_{j,\lambda}\rangle_j\}$ is a complete set of wavefunctions for particle j. Therefore, Hilbert space is separated into two subspaces: one is the symmetric states, and the other is antisymmetric states. Generalizing this concept, for a system of N identical particles, a permutation operator interchanging i-th and j-th particle act as,

$$\hat{P}_{ij}|\phi_1, \phi_2, \cdots, \phi_i, \cdots, \phi_j, \cdots, \phi_N\rangle = |\phi_1, \cdots, \phi_j, \cdots, \phi_i, \cdots, \phi_N\rangle, \tag{1.3}$$

where the label λ for other eigenstate are neglected. There exists, in general, one symmetric and one antisymmetric state, wherein all $\hat{P}_{ij}$ have the eigenvalues of ± 1, respectively.

Then why *two*? There is only one trivial perumutation operator in two-particle case. A permutation operator for *three, four*, or even N particles should work as similarly. The simplest nontrivial case of $N = 3$ have three permutation operators $\hat{P}_{ij}$ [37] and there are 3! permutations of the product states $|\phi_1, \phi_2, \phi_3\rangle$. The symmetric and antisymmetric states are,

$$|\psi_{1,2,3}\rangle_p = \frac{1}{\sqrt{6}}(|\phi_1, \phi_2, \phi_3\rangle \pm |\phi_2, \phi_1, \phi_3\rangle \pm |\phi_1, \phi_3, \phi_2\rangle$$
$$\pm |\phi_3, \phi_2, \phi_1\rangle + |\phi_3, \phi_1, \phi_2\rangle + |\phi_2, \phi_3, \phi_1\rangle) \quad \text{for } p = \pm 1, \tag{1.4}$$

respectively. The four remaining linear combinations of product states do not fall into neither totally symmetric nor antisymmetric states. (that is, all $\hat{P}_{ij}$ are not diagonal.) In general, the Hilbert space of a system of N-identical particles is divided into three subspaces: one symmetric, one antisymmetric states, and the remainder of $(N! - 2)$ linear combinations. However, to the best of our knowledge, our universe accepts only the two types of particles. No empirical evidence observed the particles under such "remainder" subspace. Rather, a strong theoretical statement which can be proved in the relativistic quantum mechanics supports the symmetric and antisymmetric Hilbert spaces: "*The wavefunction of indistinguishable integer spin particles are symmetric under pair interchange (and therefore commute), while the wavefunction of indistinguishable half-integer spin particles are antisymmetric under pair interchange (anticommute)* [37]". This is called *spin-statistics theorem*. The symmetric particles are called *bosons* and follow Bose-Einstein statistics. On the other hand, the antisymmetric particles are called *fermions* and obey Fermi-Dirac statistics. The two different quantum statistics converge into Maxwell-Boltzmann statistics as the temperature of the system increases and the system evolves from quantum to classical regime. The reader should recall that the *spin* is itself a physical "color"–like a mass or charge–unrelated to the real-space orbital motion although it shares the same generator with the angular momentum.

For a composite system like an atom, its statistics is determined by the sum of the spins of its constituents. For example, a ytterbium with mass 173 (^{173}Yb) has 70 protons, 70 electrons, and 103 neutrons. Since the net spin of ^{173}Yb is half-integer, it is a composite fermion. Likewise, ^{3}He, ^{6}Li, ^{40}K, ^{87}Sr, and ^{171}Yb are fermions, but ^{4}He, ^{7}Li, ^{39}K, ^{87}Rb, ^{86}Sr, and ^{174}Yb are bosons.

As a final remark, the linear combination of totally antisymmetric states

can be rewritten as,

$$|\psi_{1,2,\cdots,N}\rangle_{-1} = \frac{1}{\sqrt{N!}} \det \begin{vmatrix} |\phi_1\rangle_1 & |\phi_1\rangle_2 & \cdots & |\phi_1\rangle_N \\ |\phi_2\rangle_1 & |\phi_2\rangle_2 & \cdots & |\phi_2\rangle_N \\ \vdots & \vdots & \ddots & \vdots \\ |\phi_N\rangle_1 & |\phi_N\rangle_1 & \cdots & |\phi_N\rangle_N \end{vmatrix}, \qquad (1.5)$$

which is called Slater determinant. As a direct consequence, when two antisymmetric particles occupy the same individual state, the probability of finding the particle at that state vanishes. This is famous Pauli exclusion principle.

Because of the nature of the statistics, the ground state configurations of bosons and that of fermions are completely different. As the system lost its energy, the bosonic particles prefer to reside in a single energy state and the particles are described by an emergent long-range order: single macroscopic wavefunction. For a sufficient number of particles where all the excited states are saturated, the system undergoes a phase transition to a Bose-Einstein condensate (BEC). On the other hand, since the fermionic particles cannot occupy the same quantum state, they are stacked up from the lowest energy state. This is called Fermi sea. In the following section, the characteristics of fermions trapped in the external harmonic potential is explained.

1.3 Degenerate Fermions in a harmonic trapping potential

Ideal fermionic particles at a state with energy E and chemical potential μ are characterized by Fermi-Dirac distribution,

$$\bar{n}_{\mathrm{FD}}(E) = \frac{1}{e^{\beta(E-\mu)} + 1} \qquad (1.6)$$

where bar notation indicates the mean occupation number of the state, $\beta = 1/k_B T$, k_B is the Boltzmann constant, and T is the temperature. For given density of states $g(E)$, the total number of particles at spin state σ become,

$$N_\sigma = \int_0^\infty dE \, g(E) \bar{n}_{\mathrm{FD}}(E) = \int_0^\infty dE \, \frac{g(E)}{e^{\beta(E-\mu)} + 1} \qquad (1.7)$$

and the total energy of the system is,

$$E_\sigma = \int_0^\infty dE \, g(E) E \bar{n}_{\mathrm{FD}}(E) = \int_0^\infty dE \, \frac{g(E)E}{e^{\beta(E-\mu)} + 1}. \qquad (1.8)$$

For the fermionic atoms trapped in 3D harmonic potential with trapping frequency ω_j $(j \in \{x, y, z\})$

$$V(x, y, z) = \frac{1}{2} m \left(\omega_x^2 x^2 + \omega_y^2 y^2 + \omega_z^2 z^2 \right), \qquad (1.9)$$

the 3D density of states is equal to $g(E) = E^2/2(\hbar \bar{\omega})^3$, where $\bar{\omega} = (\omega_x \omega_y \omega_z)^{1/3}$ is the geometric mean of the trapping frequencies. At $T = 0$, the integration of Eq. 1.7 results in

$$E_{\mathrm{F}} = \hbar \bar{\omega} (6 N_\sigma)^{1/3}, \qquad (1.10)$$

where the Fermi energy is defined as $E_{\mathrm{F}} \equiv \mu(T = 0)$.

1.4 Principles of optical dipole trap

The harmonic trap in the former section can be realized by an optical dipole force. When a two-level atom is irradiated by a single-frequency laser source, the neutral atom experiences electric dipole interaction (E1) with the oscillating electric field [38]. The electric field $\mathcal{E}$ induces the dipole moment $\mathbf{d}$ on the neutral atom proportional to the dynamic polarizability, $\alpha(\omega)$, where ω is the frequency
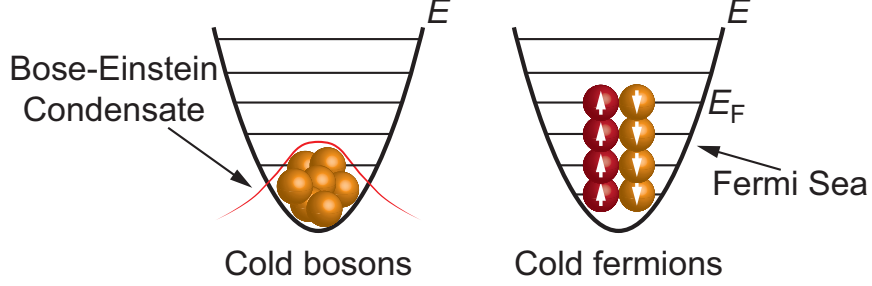
Figure 1.1: Ground state configuration of cold bosons and fermions. The bosons (left) collapse into single quantum state and show long-range order of macroscopic wavefunction called Bose-Einstein Condensation, which is expected in 1924 observed in the late 20th century [1, 2]. On the other hand, the fermions (right, two-component spin case) cannot occupy the same quantum state and fill up the confining trap, forming a Fermi sea in the degenerate regime.

of the oscillating electric field. The induced dipole re-interacts with the electric field by,

$$V_{\text{dip}}(\mathbf{r}, \omega) = -\frac{1}{2\epsilon_0 c} \text{Re}[\alpha(\omega)] I(\mathbf{r}), \tag{1.11}$$

where $I(\mathbf{r}) = 2\epsilon_0 c |\mathcal{E}(\mathbf{r})|^2$ is the light intensity, ϵ_0 is the vacuum permittivity, and c is the speed of light. This potential is known as the AC Stark (light) shift felt by the atom in the laser field. Then, the dipole potential exerts a conservative dipole force on the atom,

$$F_{\text{dip}}(\mathbf{r}, \omega) = -\nabla V_{\text{dip}}(\mathbf{r}, \omega) = \frac{1}{2\epsilon_0 c} \text{Re}[\alpha(\omega)] \nabla I(\mathbf{r}). \tag{1.12}$$

This dipole potential is proportional to the intensity of the field, $I(\mathbf{r})$, which is usually Gaussian and approximated to the harmonic trap. The explicit formula for the optical dipole potential can be calculated by expressing the dynamic polarizability in the second-order perturbation theory [39],

$$V_{mn}(\mathbf{r}, \omega) = -\sum_{m \neq n} \frac{3\pi c^2}{2\omega_{mn}^3} \left(\frac{\Gamma_{mn}}{\omega_{mn} - \omega} + \frac{\Gamma_{mn}}{\omega_{mn} + \omega} \right) I(\mathbf{r}), \tag{1.13}$$

where the summation runs over the all possible electronic states $|m\rangle \neq |n\rangle$. Here, ω_{mn} is the resonant frequency between the states $|m\rangle \rightarrow |n\rangle$ and the Γ_{mn} is the natural linewidth of the transition. When the detuning is large $|\Delta| = |\omega - \omega_{mn}| \ll \omega_{mn}$, the above equation can be approximated in a frame rotating at ω by neglecting the second term. The dipole potential becomes $V_{mn}(\mathbf{r}, \omega) \approx -\sum_{m \neq n} 3\pi c^2 / 2\omega_{mn}^3 (\Gamma/\Delta) I(\mathbf{r})$, and it is called *far-off resonance trap*, or just optical dipole trap (ODT).

It is worth to note that the dissipative process associated with the photon absorption and spontaneous emission into dipole radiation is related to the imaginary part of the dynamic polarizability. Then, in the two-level system under the rotating frame, photon scattering rate is given by,

$$\Gamma_{\text{sc}}(\mathbf{r}, \omega) = \frac{1}{\hbar\epsilon_0 c}\text{Im}[\alpha(\omega)]I(\mathbf{r}) \approx \sum_{m \neq n} \frac{3\pi c^2}{2\hbar\omega_{mn}^3}\left(\frac{\omega}{\omega_{mn}}\right)^3 \left(\frac{\Gamma_{mn}}{\Delta}\right)^2 I(\mathbf{r}). \quad (1.14)$$

The photon scattering events transfer large kinetic momentum to the atom which typically exceeds the thermal energy of the atom. Therefore, the scattering results in the heating and atom loss proportional to $(\Gamma_{mn}/\Delta)^2$. To minimize this effect, large detuning and transition lines with small linewidth are preferred.

State-dependent dipole potentials

The above equation (1.13) can be generalized when the detuning is small, which is order of hyperfine splitting of an atom ($\Delta \approx \Delta_{\text{HFS}}$). In this case, the contributions from each magnetic sublevels (hyperfine spins, m_F) are different and the light shift experienced by the atom depends on the transition strengths of each transition. The dipole matrix element in Eq. 1.11 for a transition $|m\rangle = |\gamma, J, F, m_F\rangle \rightarrow |n\rangle = |\gamma, J', F', m_{F'} = m_F + \epsilon\rangle$ (γ is some quantum

number irrelevant to the transition) is calculated using the famous Wigner-Eckart theorem, which leads to,

$$d_{mn} = \langle \gamma, J || \mathbf{d} || \gamma, J' \rangle C_{mn}. \tag{1.15}$$

Here, the first factor is called reduced dipole matrix element and is independent of magnetic substructures. It is related to the natural linewidth of the transition by $\Gamma_{mn} = \frac{\omega_{mn}^3}{3\pi\epsilon_0 \hbar c^3} \frac{2J+1}{2J'+1} |\langle \gamma, J || \mathbf{d} || \gamma, J' \rangle|^2$. The second factor is Clebsch-Gordan coefficient given by,

$$C_{mn}(\epsilon) = (-1)^{2F'+J+I+m_F} \sqrt{(2J+1)(2J'+1)(2F+1)(2F'+1)}$$
$$\times \begin{Bmatrix} L' & J' & S \\ J & L & 1 \end{Bmatrix} \begin{Bmatrix} J' & F' & I \\ F & J & 1 \end{Bmatrix} \begin{pmatrix} F & 1 & F' \\ m_F & \epsilon & -(m_F+\epsilon) \end{pmatrix}. \tag{1.16}$$

where the curly brackets and a round bracket denote $6j$-symbols and $3j$-symbol, respectively, and $\epsilon = (1, 0, -1)$ is the polarization state in spherical basis. The transition strength is defined as the absolute square of the Clebsch-Gordan coefficients, $|C_{mn}(\epsilon)|^2$. Then the state-dependent AC Stark shift becomes,

$$V_{mn}(\mathbf{r}, \omega, \epsilon) = -\sum_{m \neq n} \frac{3\pi c^2}{2\omega_{mn}^3} |C_{mn}(\epsilon)|^2 \alpha_{JJ'} \left(\frac{\Gamma_{mn}}{\omega_{mn} - \omega} + \frac{\Gamma_{mn}}{\omega_{mn} + \omega} \right) I(\mathbf{r}), \tag{1.17}$$

where $\alpha_{JJ'} = (2J'+1)/(2J+1)$ is the multiplicity factor [38], which is nothing but a normalization factor. For a far-off resonance trap, the colors become dull as $\sum_{m \neq n} |C_{mn}|^2 \alpha_{JJ'} \to 1$ and the above formula recovers the Eq. 1.13. The spin-dependent dipole potentials can be applied to create spin-dependent optical lattice [40] or to perform an optical Stern-Gerlach experiment [41].

1.5 Optical lattice and tight-binding model

One important application of the dipole traps is an optical lattice. When an atom encounters two counter-propagating laser beams, interference between the two beams results in the periodic dipole potentials. A typical way to create an optical lattice is to send a single-frequency laser (narrow enough linewidth to certainly define wavelength of the light) to the neutral atoms in the retro-reflecting configuration. The fixed-end reflection at the mirror determines the phase of the wave and resulting dipole potentials form peaks and valleys which mimics real crystalline solids. The atoms in the optical lattice experience periodic external potential like,

$$V_{\text{OL}}(r, z) = V_0 e^{-2\frac{r^2}{w^2(z)}} \cos^2\left(k_{\text{L}} z\right) \approx V_0 \cos^2\left(k_{\text{L}} z\right) + \frac{1}{2} m\omega_r^2 r^2 + \frac{1}{2} m\omega_z^2 z^2. \quad (1.18)$$

where $w(z)$ is the beam waist, k_{L} is the wavenumber of the lattice laser, and $\omega_{r,z}$ are the harmonic trap frequencies. The lattice depth V_0 is usually expressed in the unit of the recoil energy, $E_{\text{L}} = \hbar^2 k_{\text{L}}/2m$, by $s = V_0/E_{\text{L}}$. The exponential factor due to the Gaussian laser beam profile is approximated to the harmonic form. The overall harmonicity is obtained by expanding this potential around the origin,

$$
\begin{aligned}
\omega_r &= \sqrt{\frac{4V_0}{mw_0^2}} = \sqrt{\frac{4E_L}{mw_0^2}}\sqrt{s} \\
\omega_z &= \sqrt{\frac{2V_0}{mz_R^2}} = \sqrt{\frac{2E_L}{mz_R^2}}\sqrt{s},
\end{aligned}
\quad (1.19)
$$

where $w_0 = w(0)$ and $z_R = \pi w_0^2/\lambda$ is the Rayleigh range of the lattice beam.

In general, the optical lattice for the three-dimension (3D) is,

$$V_{\text{3D}} = V_x \cos^2\left(k_{\text{L}} x\right) + V_y \cos^2\left(k_{\text{L}} y\right) + V_z \cos^2\left(k_{\text{L}} z\right). \quad (1.20)$$

The mutual interferences can be eliminated by using orthogonal polarization or different frequencies of the light. In the latter case, the effect is averaged out for the fast enough (few MHz) oscillation frequency differences.

The problem of single-particle under the periodic potential has been extensively studied in the condensed matter physics. The translational symmetry implies that the atoms in the optical lattice is well described by the Bloch functions, $\psi_q^{(n)}(z) = e^{iqz}u_q^{(n)}(z)$, where the energy eigenstates are expressed in the form of Bloch bands $E^{(n)}(q)$ with band index n. Neglecting weak overall harmonic trapping effects, the Hamiltonian for a particle in one-dimensional (1D) optical lattice becomes,

$$\hat{H} = \frac{p^2}{2m} + V_0 \cos^2 (k_L z). \tag{1.21}$$

The Schrodinger equation $\hat{H}\psi_q^{(n)}(z) = E^{(n)}(q)\psi_q^{(n)}(z)$ can be reforged in the form of Mathieu's differential equation, $\psi'' + [a - 2\eta \cos(2\tilde{z})]\psi = 0$, as,

$$\left[\frac{\partial^2}{\partial \tilde{z}^2} + \left(\frac{E}{E_L} - \frac{s}{2} - \frac{s}{2} \cos (2\tilde{z}) \right) \right] \psi(\tilde{z}) = 0 \quad \text{with} \quad \tilde{z} = k_L z, \tag{1.22}$$

where standard Mathieu parameters are given by $a = E/E_L - s/2$ and $\eta = s/4$. Given lattice depth η, the solutions of the Mathieu's equation is found at many certain values of a–these values are called Mathieu characteristic value $\mathcal{A}(q/k_L, -s/4)$, which is obvious from the Bloch theorem (Mathematically, the Bloch theorem is equivalent to the Floquet's theorem). Then the eigenenergies are given by,

$$E^{(n)}(k) = \mathcal{A}\left(\nu, -\frac{s}{4}\right) + \frac{s}{2}, \quad q \in [-k_L, k_L], \tag{1.23}$$

where $\nu(q, n)$ is the characteristic exponent expressed as,

$$\nu(q, n) = \frac{q}{k_L} + (-1)^n \, \text{sgn}\left(\frac{q}{k_L}\right) (n + n \bmod 2). \tag{1.24}$$

12

The eigenenergies for different values of s are plotted in Fig. !. Also, the Bloch wavefunction $\psi_q^{(n)}(z)$ is the linear combination of the Mathieu cosine $\mathcal{C}$ (even) and sine $\mathcal{S}$ (odd) functions:

$$\psi_q(\tilde{z}) = \mathcal{C}\left(a, \eta, \tilde{z}\right) + i \operatorname{sgn}\left(q\right) \mathcal{S}\left(a, \eta, \tilde{z}\right), \tag{1.25}$$

which forms a complete orthogonal set.

Wannier functions

The motion of a particle in the optical lattice is described by these Bloch waves traveling inside the lattice. As the lattice depth s increases, the probability of finding an atom in a single lattice site increases. In this sense, the atomic wavefunction is well-localized. To illustrate this, it is convenient to bring the description into real space representation: Wannier functions. One simplest definition of Wannier functions is the Fourier transform of the Bloch waves,

$$\begin{aligned} w(z - z_i) &= \frac{1}{\sqrt{\mathcal{N}}} \sum_{q \in \text{BZ}} e^{iqz_i} \psi_q^{(n)}(z) \\ &= \frac{1}{\sqrt{\mathcal{N}}} \int_{-k_\text{L}}^{k_\text{L}} \mathrm{d}q \; e^{iqz_i} \psi_q^{(n)}(z), \end{aligned} \tag{1.26}$$

where $\mathcal{N}$ is normalization constant and z_i is the position of the i-th lattice site. The Wannier functions also form a complete orthogonal set of basis. For a separable potential (such as orthorombic potentials), the generalization to 3D case is somewhat trivial: $w_{(n_x, n_y, n_z)}(x, y, z) = w_{n_x}(x) w_{n_y}(y) w_{n_z}(z)$.

Tight-binding model

The tight-binding approximation describes particles in a periodic potential by isolated wavefunctions at each lattice site. This becomes true if the lattice depth

13

s becomes sufficient to provide orthonormal Wannier states localized in the single lattice site. The Hamiltonian in the second-quantized form can be written as,

$$\hat{H} = \sum_\sigma \int d\mathbf{r} \ \hat{\psi}_\sigma^\dagger(\mathbf{r}) \left[-\frac{\hbar^2}{2m}\nabla^2 + V_{\text{latt}}(\mathbf{r}) \right] \hat{\psi}_\sigma(\mathbf{r})$$
$$+ \frac{1}{2}\sum_{\sigma,\sigma'} \int d\mathbf{r}d\mathbf{r}' \ \hat{\psi}_{\sigma'}^\dagger(\mathbf{r}')\hat{\psi}_\sigma^\dagger(\mathbf{r})U_{\text{int}}(\mathbf{r},\mathbf{r}')\hat{\psi}_\sigma(\mathbf{r})\hat{\psi}_{\sigma'}(\mathbf{r}') \tag{1.27}$$

where $\hat{\psi}_\sigma(\mathbf{r}) = \sum_j w(\mathbf{r} - \mathbf{r}')\hat{c}_{j\sigma}$ is the field operator of the particle with spin index σ, $\hat{c}_{j\sigma}^\dagger$ ($\hat{c}_{j\sigma}$) stands for the creation (annihilation) operator, V_{latt} is the optical lattice potential, and U_{int} is the interaction potential. Here, single-band approximation is assumed, which means that the atoms play in only the lowest band of the system and the Wannier functions $w_n = w_1 \equiv w(\mathbf{r} - \mathbf{r_j})$.

When the hopping to the nearest neighbor site is dominant over the higher-order hoppings, the only nearest hopping is considered. The hopping from site $\mathbf{r_i}$ to $\mathbf{r_j}$ is described by the tunneling matrix,

$$t_{ij} = \int d\mathbf{r} \ w^*(\mathbf{r_j}) \left[-\frac{\hbar^2}{2m}\nabla^2 + V_{\text{latt}}(\mathbf{r}) \right] w(\mathbf{r_i}), \tag{1.28}$$

where $\mathbf{r_j} = \mathbf{r_i} + \mathbf{d}$ and $\mathbf{d}$ is the lattice unit vector.

For ultracold atomic system, the interparticle interaction is described only by the s-wave contact interaction, and $U_{\text{int}}(\mathbf{r},\mathbf{r}') = g\delta(\mathbf{r}' - \mathbf{r})$ with $g = 4\pi\hbar^2 a_s/m$. In the lattice systems, the on-site interaction energy becomes,

$$U_{\text{int}} = \frac{4\pi\hbar^2 a_s}{m} \int d\mathbf{r} \ |w(\mathbf{r})|^4 \tag{1.29}$$

where a_s is the s-wave scattering length.

The above derivations are independent of particle statistics. For bosonic (fermionic) particles, the operators follow bosonic (fermionic) commutation rules,

respectively. In case of bosons, the spin index diminishes and the final Hamiltonian becomes,

$$\hat{H}_{\mathrm{BH}} = -\sum_{ij} t_{ij}\hat{c}_i^\dagger\hat{c}_j + \frac{U_{\mathrm{int}}}{2}\sum_i \hat{n}_i\left(\hat{n}_i - 1\right), \quad \hat{n}_i = \hat{c}_i^\dagger\hat{c}_i \qquad (1.30)$$

which is called Bose-Hubbard model (neglecting the chemical potential term). In case of fermions, the on-site interaction energy is only applicable for the different spin fermions. The Hamiltonian describing fermionic system is the Fermi-Hubbard model [42]:

$$\hat{H}_{\mathrm{FH}} = -\sum_{ij} t_{ij}\hat{c}_{i\sigma}^\dagger\hat{c}_{j\sigma} + \frac{U_{\mathrm{int}}}{2}\sum_{j,\sigma\neq\sigma'} \hat{c}_{j\sigma}^\dagger\hat{c}_{j\sigma'}^\dagger\hat{c}_{j\sigma'}\hat{c}_{j\sigma}. \qquad (1.31)$$

The tight-binding approximation is a powerful tool for studying crystalline physics. For instance, the ground band of noninteracting particles inside the infinite one-dimensional optical lattice can be easily calculated,

$$E(q) = -2t\cos\left(qd_{\mathrm{L}}\right). \qquad (1.32)$$

Conversely, the tunneling t can be determined by $t = \left(E(q = k_{\mathrm{L}}) - E(0)\right)/4$.

1.6   Topological band theory

When Berry phase associated with a Bloch band shows nontrivial value, the band is called topological in the sense that its physical property cannot be changed without closing the band gap [43]. Consider an insulator filled below the certain energy gap. By the principle of adiabatic continuity, any two insulators are equivalent as long as one can be smoothly deformed into one another by adiabatically modifying the given Hamiltonian. However, this cannot happen if Berry phase of two states are different, since their topology is uncommon. To

do so, the system undergoes a topological phase transition which is known to be necessarily involve closing the band gap. The ground state of such topological bands has been earned a great attention, since their phase transition seems to become exceptions of conventional Landau theory of phase transition.

The general theory to classify all the topological Hamiltonians is not yet understood. It is more interesting and complicated if the interaction between particles are turned on. The relation between the topology and the band theory is explained in Ch. 4.

1.7 The outline of the thesis

Throughout the dissertation, the most of sentences use "we", instead of I, to dedicate for the contribution to the works done by my dear colleagues: M.-S. Kim, M. Lee, and J. H. Kang.

This dissertation is organized as follows. In chapter 2, the details of our ytterbium machine is illustrated. In chapter 3, basic principles of Raman two-photon transition and generation of artificial gauge potential are explained. In chapter 4, a quick overview of the quantum Hall physics is placed. The chapter 5 describes the main results of this thesis: the realization of synthetic Hall tube (cylinder) using cyclic coupling scheme. Finally, the chapter 6 is devoted to depict the photoassociation experiment performed with ultracold fermionic 173 ytterbium (^{173}Yb) atoms.

Chapter 2

The Ytterbium machine

Most of my graduate years had been devoted to building an experimental apparatus for cooling ytterbium atoms. The machine is divided into three parts: Laser system, Vacuum system, and Control system. In this section, I will discuss fundamental properties of ytterbium atoms and how to reach the quantum degeneracy (ultracold temperatures). This chapter is mostly related to the following paper.

- M.-S. Kim, M. Lee, J. H. Han, and Y. Shin, *"Experimental apparatus for generating quantum degenerate gases of Ytterbium atoms,"* Jour. Kor. Phys. Soc. **67**, 1719 (2015).

2.1   Fundamental properties of ytterbium atoms

Ytterbium is one of the alkaline-earth-like element with two valence electrons. In the periodic table, it is located in the fourteenth and penultimate element in lanthanide series. Its name is derived from the name "Ytterby", the village in

Sweden famous for having rich source of chemical elements. Ytterbium is a soft, malleable, and ductile metal with bright and silvery color. Like other alkali and alkaline-earth-like metals, the ytterbium quickly oxidizes when exposed to the oxygen (or in the air). In the room temperature, it has melting point around 824°C (1097 K) and boiling point 1196°C (1469 K). The typical temperatures required to produce a sufficient vapour pressure more than 10^{-3} torr for successful creation of degenerate gases is in the range of $400-500$°C (≈ 720 K) [44,45]. Ytterbium is highly reactive at this temperature range; severe chemical reaction to silica glass as well as sapphire, which are frequently used for vacuum viewports, are reported. Therefore, a care must be taken with dealing with the viewports, which should not be exposed to direct flux without any safety feature such as heating the viewport. Moreover, copper gaskets are necessary, because of the corrosive characteristics of the element.

Natural ytterbium has seven stable isotopes with five bosonic species (^{168}Yb, ^{170}Yb, ^{172}Yb, ^{174}Yb, and ^{176}Yb) and two fermionic ones (^{171}Yb and ^{173}Yb). The first quantum degeneracy of the ytterbium atoms is reported by Kyoto group [46]. Since then, six of the isotopes are cooled down to the degenerate temperature [47–50]. In 2011, Paris (ENS) and Washington (Gupta) group [51,52] also succeeded to create quantum degenerate gases of ytterbium. Especially, Washington group cooled the ytterbium atoms together with ^{6}Li atoms to study physics of interspecies interaction [53]. The quantum degeneracy of Bose-Bose, Bose-Fermi, and Fermi-Fermi mixtures have been demonstrated [54,55]. After 2013, Hamburg (Sengstock) [56], München (Bloch) [57], Firenze (LENS) [58], Maryland (JQI NIST) [59], Seoul (Shin) [60,61], Daejeon (Mun) [62], and Hongkong (Jo) [63] group have been achieved to trap cold atoms of ytterbium in degenerate temperatures.

Table 2.1: Isotopes of ytterbium atoms

Isotopes	Mass (m_0)	Nucler spin $(\mathcal{I})$	Natural abundance $(\%)$	Magnetic moment $(\mu_{\mathcal{I}})$
^{168}Yb	167.933894	0	0.13	
^{170}Yb	169.934759	0	3.05	
^{171}Yb	170.936323	1/2	14.3	+0.4919
^{172}Yb	171.936378	0	21.9	
^{173}Yb	172.938208	5/2	16.12	-0.6776
^{174}Yb	173.938859	0	31.8	
^{176}Yb	175.942564	0	12.7	

One great motivation of generating quantum degenerate gas of ytterbium atoms is the SU($\mathcal{I}$) interaction in the ground state fermions. Unlikely to the fermionic alkali atoms, which are stable mostly for the two component case, alkaline-earth-like atoms including ytterbium are useful to study multi-component physics such as SU($\mathcal{I}$) Hubbard and Heisenberg model. Also, the presence of the metastable clock transition (^{3}P$_0$) with SU($\mathcal{I}$) interactions offers an opportunity for implementing artificial gauge potentials [64] with Harper-Hofstadter Hamiltonian [65, 66], including the non-Abelian gauge fields [67]. It is also promising to study SU($\mathcal{I}$) Kondo physics [68] as well as Kugel-Khomskii model [30] using state-dependent optical lattice with magic and anti-magic wavelengths [69]. The ytterbium quantum gas takes these two distinct features in the price of lack of modifying interaction strength via magnetic Feshbach resonance; however, very recently, changing interaction strengths using the interplay between the ground state and the clock states become available via orbital Feshbach resonance [70–72], which is only applicable to the ytterbium atoms (not alkaline-earth-like atoms). Since these topics are beyond the scope of this thesis, they will not be discussed further.

Table 2.2: Isotope shifts of frequently used transitions of ytterbium atoms. The frequency shifts are represented with respect to ^{174}Yb. The data are taken from Refs. [73–77]

| Transition | | Isotope shift (MHz) | | |
Isotope	$F \to F'$	$^1\mathrm{S}_0 \to{}^1\mathrm{P}_1$	$^1\mathrm{S}_0 \to{}^3\mathrm{P}_1$	$^1\mathrm{S}_0 \to{}^3\mathrm{P}_0$
^{168}Yb		1887.40	3655.13	
^{170}Yb		1192.39	2286.35	
^{171}Yb	centroid	939.52	1825.72	1811.28164
	$1/2 \to 3/2$	832.44	3804.61	
	$1/2 \to 1/2$	1153.70	-2132.06	
^{172}Yb		533.31	1000.22	
^{173}Yb	centroid	291.52	555.78	551.53839
	$5/2 \to 3/2$	515.98	3807.28	
	$5/2 \to 5/2$	-253.42	2311.41	
	$5/2 \to 7/2$	587.99	-2386.70	
^{174}Yb		0	0	0
^{176}Yb		-509.31	-954.83	

2.1.1 Atomic level structure of ytterbium atoms

The ground state electronic configuration of the ytterbium is $[\mathrm{Xe}]4f^{14}6s^2$. Because the f-shell is completely occupied, the atomic properties are mainly determined by the two valence electrons and are very similar to the alkaline-earth atoms such as calcium or strontium. This is why we call the ytterbium as a member of alkaline-earth-like elements.

The Hamiltonian of an alkaline-earth-like atom with Z total electrons is,

$$\hat{H} = \sum_{i=1}^{Z} \left[-\frac{\hat{\mathbf{p}}_i^2}{2m} + V(r_i) \right] + \hat{H}_{\mathrm{ee}} + \hat{H}_{\mathrm{LS}}, \tag{2.1}$$

20

where $\hat{\mathbf{p}}_i$ is the momentum of i-th atom, m is the atomic mass, and $V(r_i)$ is the electrostatic potential between the closed shell and the valence electrons. To proceed, the central field approximation is assumed, where the large part of the closed shell within the core has spherical charge distribution. The interactions between the shells depend only on the radial coordinate, which is given by $V(r_i) = -Ze^2/4\pi\epsilon_0 r_i$ [78], where e is the electron charge and ϵ_0 is the vacuum permittivity. Also, $\hat{H}_{\text{ee}} = \sum_{i<j=1}^{Z} e^2/4\pi\epsilon_0 r_{ij}$ is the electron repulsion between i-th and j-th electrons. Finally, $\hat{H}_{\text{LS}} = \sum_{i=1}^{Z} \alpha_i \mathbf{l}_i \cdot \mathbf{s}_i$ is the spin-orbit interaction.

To diagonalize the above Hamiltonian, the good quantum number is chosen by the relative strength between the electron repulsion term and spin-orbit interaction term. In case of light atoms with low Z, like helium or magnesium, the electron repulsion term dominates and the small spin-orbit interaction leads to poor fine structure splitting. The eigenstates of the Hamiltonian is described by $\{\mathbf{L}^2, L_z, \mathbf{S}^2, S_z\}$ (the principal quantum number n_i is neglected), where $\mathbf{L} = \sum_i \mathbf{l}_i$ and $\mathbf{S} = \sum_i \mathbf{s}_i$. Then, the $\hat{H}_{\text{LS}}$ is treated as perturbative manner with $\mathbf{J} = \mathbf{L} + \mathbf{S}$ basis. The final eigenbasis of the system become $\{\mathbf{L}^2, \mathbf{S}^2, \mathbf{J}, J_z\}$. This is called LS or $Russel\text{-}Saunders\ coupling$ scheme and the term symbol is described in the form of $^{2S+1}L_J$.

On the other hand, heavy atoms have large spin-orbit interaction term and the spin-orbit interaction term is no more a mere perturbation. Instead, the Hamiltonian is diagonalized by introducing $\mathbf{j}_i = \mathbf{l}_i + \mathbf{s}_i$ for the two valence electrons $i = 1, 2$. Therefore, total eigenbasis becomes $\{\mathbf{j}_1, \mathbf{j}_2, \mathbf{J}, J_z\}$ with $\mathbf{J} = \mathbf{j}_1 + \mathbf{j}_2$. This is called $JJ\ coupling$ scheme.

For an ytterbium atom, strong spin-orbit interaction mixes the LS-coupling basis. One important result is the presence of clock transition and intercombination line. The standard selection rules for electric dipole (E1) transitions are

given by $\Delta J = 0, \pm 1 (0 \to 0$ forbidden$)$ with $\Delta L = \pm 1$ and $\Delta S = 0$. This is because a photon (or an electron dipole operator, μ) does not act on the electron spin itself. Therefore, spin singlet and triplet states describe different set of energy levels. However, in the heavy atoms, the wavefunctions of $^1P_1$ and $^3P_1$ get mixed, which contributes small portion of transition probability between the singlet and triplet states. This is called a multiplet mixing. As the atomic mass grows, the spin-orbit interaction increases as well as the transition probability (proportional to the natural linewidth). The transition linewidth of intercombination line ($^1S_0 \to ^3P_1$) is $\Gamma(^3P_1)/(2\pi) = 182.4$ kHz for an ytterbium, 7.5 kHz for a strontium, and 0.47 kHz for a calcium. Similarly, the mixing between $^1S_0$ and $^3P_0$ leads to the presence of a clock transition ($^1S_0 \to ^3P_0$), which has sub-Hz linewidth and useful to develop an atomic clock [75, 79–82].

The atomic transition lines are depicted in Fig. 2.1. For laser cooling of ytterbium atoms, two major transition lines are used: one is dipole-allowed $^1S_0 \to ^1P_1$ (398.9 nm, blue transition) and another is aforementioned intercombion line $^1S_0 \to ^3P_1$ (555.8 nm, green transition). The blue transition has large linewidth about $\Gamma(^1P_1)/2\pi = 29.1$ MHz and therefore the photon scattering force is strong. Hence, the blue transition is suitable for the Zeeman slower and imaging. It is worth to be noted that the blue transition is not completely closed–some portion about few % of population leaks into $^3P_0$ and $^3P_2$ states. The green transition has sub-MHz narrow linewidth ($\Gamma(^3P_1)/2\pi = 182.4$ kHz), which provides less photon scattering force, but has lower Doppler cooling limit, $T_{\rm D}$. Therefore, the basic strategy for laser cooling is to slow down the atomic beam from the oven using the blue transition and then capture the magneto-optical trap (MOT) with the green transition. It is also possible to cool down the atoms using the blue and green beams at the same time, where the blue

Table 2.3: Basic parameters of frequently used transitions of ytterbium atoms, where λ wavelength, Γ natural linewidth, τ lifetime, I_{sat} saturation intensity, T_{D} Doppler temperature, and v_{R} is the recoil velocity of corresponding transition. Here, g_J is Landé g-factor of the relevant excited state. [45, 83, 84]

Parameters	$^1S_0 \to {}^1P_1$	$^1S_0 \to {}^3P_1$	$^1S_0 \to {}^3P_0$
λ	398.9 nm	555.8 nm	578.4 nm
$\Gamma/(2\pi)$	29.1 MHz	182.4 kHz	$\leq$ 10 mHz
$\tau = 1/\Gamma$	5.464 ns	866.1 ns	$\geq$ 20 s
$I_{\mathrm{sat}} = \pi hc/(3\lambda^3\tau)$	59.97 mW/cm^2	0.139 mW/cm^2	$\leq$ 10 pW/cm^2
$T_{\mathrm{D}} = \hbar\Gamma/(2k_{\mathrm{B}})$	699 μK	4.4 μK	$\leq$ 1 nK
$v_{\mathrm{R}} = \hbar k_{\mathrm{R}}/m$	5.8 mm/s	4.2 mm/s	4.0 mm/s
g_J	1.035	1.493	- ($J=0$)

transition dominates at the outer shell to improve the loading rate [62]. The intercombination line is one of the most important transition in this thesis, since it is employed for spin manipulation/detection techniques, Raman transitions, and photoassociation transtions. Some relevant parameters of frequently used transitions of ytterbium atoms are summarized in Table 2.3.

2.1.2 Scattering properties and emergent SU($\mathcal{I}$) symmetry

The collisional properties of ultracold atoms are typically scaled in terms of s-wave scattering length a_s. Since the atoms at degenerate regime have not enough kinetic (thermal) energy to overcome higher-order centrifugal barriers, a_s is the only parameter to be considered. When the atomic cloud is dilute enough to be described by the effective interaction range, which is much shorter than the

6s7s

³S₁

$\lambda = 770.2$ nm
$\Gamma_d/2\pi = 3.7 \times 10^7$ s⁻¹

$\lambda = 1479.3$ nm
$\Gamma_d/2\pi = 2.0 \times 10^6$ s⁻¹

$\lambda = 1388.8$ nm
$\Gamma_d/2\pi = 2.0 \times 10^6$ s⁻¹

6s5d

¹D₂

6s5d

³D$_J$ —— J=2

J=1
J=0

6s6p

¹P₁

$\Gamma_d/2\pi = 11.8$ s⁻¹

$\lambda = 680.1$ nm
$\Gamma_d/2\pi = 2.7 \times 10^7$ s⁻¹

³P$_J$ —— J=2

$\lambda = 649.1$ nm
$\Gamma_d/2\pi = 9.6 \times 10^6$ s⁻¹

Zeeman slower
and Imaging

J=1 6s6p
J=0

$\lambda = 398.9$ nm
$\Gamma/2\pi = 29.1$ MHz

Ultranarrow transition
$\lambda = 507.3$ nm
$\Gamma/2\pi < 15$ mHz

Magento-Optical Trap
$\lambda = 555.8$ nm
$\Gamma/2\pi = 182$ kHz

Ultranarrow (clock) transition
$\lambda = 578.4$ nm
$\Gamma/2\pi < 10$ mHz

¹S₀

6s²

Singlet states (S=0)

Triplet states (S=1)

Figure 2.1: Energy level diagram of an ytterbium atom with various optical transitions. Two frequently used optical transitions are depicted: ¹S₀ →¹P₁ (blue) is employed for Zeeman slower and absorption imaging, while ¹S₀ →³P₁ (green) is used to capture Magneto-Optical Trap (MOT) and to carry out various spin-dependent manipulations of the fermionic atoms. Γ is the natural linewidth of corresponding (closed) transition and Γ_d is the decay rate (red lines).

24
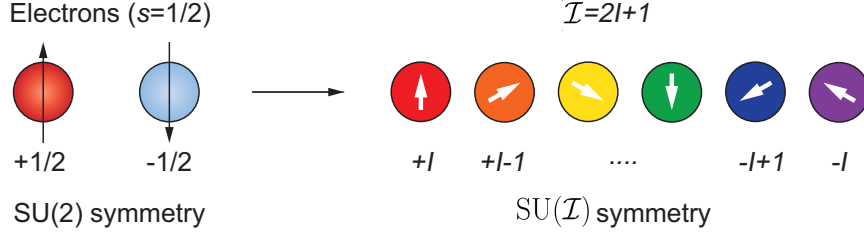
Figure 2.2: Emergent $SU(\mathcal{I})$ symmetry in the ground states of alkaline-earth-like atoms such as ^{173}Yb and ^{87}Sr.

interparticle distance, the interatomic potentials are well approximated by the pseudopotential [85],

$$V(\mathbf{r}) = \sum_{\text{even } j=0}^{2F-1} \frac{2\pi\hbar^2 a_s^{(j)}}{\nu} \delta(\mathbf{r}) \frac{\partial}{\partial r}[r\cdot] \, \mathcal{P}_j \qquad (2.2)$$

where $r = |\mathbf{r}|$ is relative distance between the colliding atoms, μ is their reduced mass, and $\mathcal{P}_j$ is the projection operator onto the states with $j = 0, 2, \cdots, 2F-1$. Note that the quantum statistics allows only the symmetric wavefunctions of the even F terms. In general, the s-wave scattering lengths are different for each spin state, which stems from different electronic configurations of the colliding atoms.

For an alkaline-earth-like atom such as ytterbium or strontium, the electronic configuration of the ground state ($^1S_0$) has zero electronic angular momentum ($J = 0$). This is because of the Hund's rule, which implies that the spins of two valence electrons should be antiparallel. Instead, the absence of hyperfine interaction makes the nuclear spins (I), which are nonzero only for fermionic isotopes, almost perfectly decoupled from the electron spins. Therefore, the nuclear spin states formulate a set of good quantum numbers $\{F = I, m_F = m_I\}$. This electronic-nuclear spin decoupling establishes the s-wave scattering lengths

be independent of the the nuclear spin, $a_s^{(j)} = a_s$. The variation of the scattering lengths for different nuclear spin states is estimated as $\delta a_s / a_s \sim \Delta\phi = \Delta V \Delta t / \hbar$, where $\Delta\phi$ is shift of semiclassical phase of the atomic wavefunction and $\Delta t \sim 1$ ps is the typical interaction time [30]. For $^1S_0$ state, the potential difference between different nuclear spin projections ΔV can be calculated by $\Delta V / h \sim E_{\mathrm{hf}}^2 / (E_{\mathrm{opt}} h) \sim 200$ Hz, where $E_{\mathrm{hf}} \sim 300$ MHz is hyperfine splittings in $^3P_1$ and $E_{\mathrm{opt}} / h \sim 400$ THz is the optical energy in the $^1S_0 \rightarrow ^3P_1$ transition. Therefore, $\delta a_s / a_s \sim 10^{-9}$, which leads to the emergent $SU(\mathcal{I} = 2F + 1)$ symmetry for the nuclear spin states of ground state alkaline-earth-like atomic species [86].

In case of ytterbium fermions, ^{173}Yb has six ground spin states and ^{171}Yb has two ground spin states. The scattering lengths for intra/inter-isotopes in the ground state are summarized in the Table 2.1.2, which are measured via two-color photoassociation (PA) spectroscopy. The PA resonances near the ground state gives the knowledge of interatomic potential, which is crucial for determining the scattering lengths. The two most abundant species of ytterbium, bosonic ^{174}Yb and fermionic ^{173}Yb, carries good scattering length to perform evaporative cooling. For fermionic isotope, the evaporation works for only when the sample composes multiple spin components. In case of the other isotopes, sympathetic cooling with other atoms with good scattering property is necessary. For instance, ^{171}Yb is typically cooled with ^{173}Yb, which has $a_s \approx 200 a_0$ and $a_{171-173} \approx -578 a_0$.

Surprisingly, the alkaline-earth-like atoms have another $J = 0$ state for excited $^3P_0$ manifold. For the $^3P_0$ states, the decoupling still serves vanishing hyperfine interaction to the leading order; however, in this case, the decoupling is slightly broken by the admixture with higher-lying P states with nonzero

Table 2.4: s-wave scattering length between the isotopes of ytterbium atoms in units of a_0 (Bohr radius). The numbers are taken from Ref. [87]

	^{168}Yb	^{170}Yb	^{171}Yb	^{172}Yb	^{173}Yb	^{174}Yb	^{176}Yb
^{168}Yb	**252.0(34)**	117.0(15)	89.2(17)	65.0(19)	38.6(25)	2.5(34)	359.2(30)
^{170}Yb		**63.9(21)**	36.5(25)	-2.1(36)	-81.3(68)	-518.0(51)	-209.5(23)
^{171}Yb			**-2.8(36)**	-84.3(68)	-578(60)	-429(13)	141.6(15)
^{172}Yb				**-599(64)**	418(13)	200.6(23)	106.2(15)
^{173}Yb					**199.4(21)**	138.8(15)	79.8(19)
^{174}Yb						**104.9(15)**	54.4(23)
^{176}Yb							**-24.2(43)**

$J \neq 0$, which brings $\delta a_s / a_s \sim 10^{-3}$ [30]. Hence, the $^1\mathrm{S}_0$ and $^3\mathrm{P}_0$ manifold exhibit two-orbital SU($\mathcal{I}$) symmetry, which can be interest in other research fields of physics beyond ultracold quantum gases [88–91].

2.1.3 Interaction with weak magnetic field

The magnetic dipole interaction (M1) Hamiltonian leads to the Zeeman shift,

$$\hat{H}_\mathrm{Z} = -\mu \cdot \mathbf{B} = \frac{1}{\hbar}\mu_B g_F \hat{\mathbf{F}} \cdot \mathbf{B}$$
$$= \mu_B g_F m_F B, \tag{2.3}$$

where μ_B is Bohr magneton, g_F is combined (effective) Landé g-factor, and m_F is the magnetic quantum number, which is a projection of $\hat{\mathbf{F}}$ along the quantization axis. The Zeeman shift splits the hyperfine states into magnetic sublevels (spins) linearly for weak magnetic fields, unless LS-coupling is broken in the Paschen-Back regime. The combined g-factor leads to,

$$g_F = g_J \frac{F(F+1) - I(I+1) + J(J+1)}{2F(F+1)} + g_I \frac{F(F+1) + I(I+1) - J(J+1)}{2F(F+1)}, \tag{2.4}$$

where $g_I = \mu_I/(I\mu_B)$ and μ_I is the nuclear magneton. Especially, owing to the decoupling of nuclear spin from that of electrons, $\hat{\mathbf{F}} = \hat{\mathbf{I}}$ ($J = 0$ for $^1\mathrm{S}_0$) and

the Zeeman shift of the ground state ytterbium atoms arises solely due to the nuclear spins. Therefore, for the bosonic isotopes, the absence of nuclear spins implies that their ground states are insensitive to the external magnetic field. The magnetic moment of bosonic isotopes depends fully on the excited state. The Landé g-factor is $g_J = 1.035$ for $^1S_0 \rightarrow {}^1P_1$ and $g_J = 1.493$ for $^1S_0 \rightarrow {}^3P_1$.

For the fermionic isotopes, the nuclear spin degree of freedom needs to be considered. Since $\mu_I = \mu_B(m_e/m_p)$, where $m_{e,p}$ are electron and nuclear magneton, respectively, the nuclear magneton is smaller than the Bohr magneton in three orders of magnitude ($m_e/m_p \approx 1/1836$). The splitting can be calculated based on the g-factor values $g_I = 0.6776$ for $^1S_0$ and $g_I = 1.493$ for $^3P_1$. For example, the Zeeman effect for $^1S_0$ state results in the linear splitting of 207 Hz/G. The magnetic substructure of ^{173}Yb is depicted in the Fig. 2.3.

Miscellaneous

The lack of magnetic moment in the ground manifold hinders the use of magnetic Feshbach resonance, which is a classic method to modify interatomic interactions. Alternatively, the scattering lengths are tuned by means of optical Feshbach resonance (OFR) [92–97], where the open and closed channels are coupled via resonant light instead of Zeeman energy. However, because of the harsh photon scattering events (heating from spontaneous emission) as well as the severe N-body losses, OFRs are not applicable for alkali atoms and still require further development. Especially, OFRs are better suited for alkaline-earth-like atoms because of their small scattering rates owing to the narrow transition linewidths. To implement OFR, it is necessary to know interatomic potentials in detail by PA spectroscopy, which is explained in Section 6. Recently, the control of interaction strength via mixing different orbital states $^1S_0$ and $^3P_0$
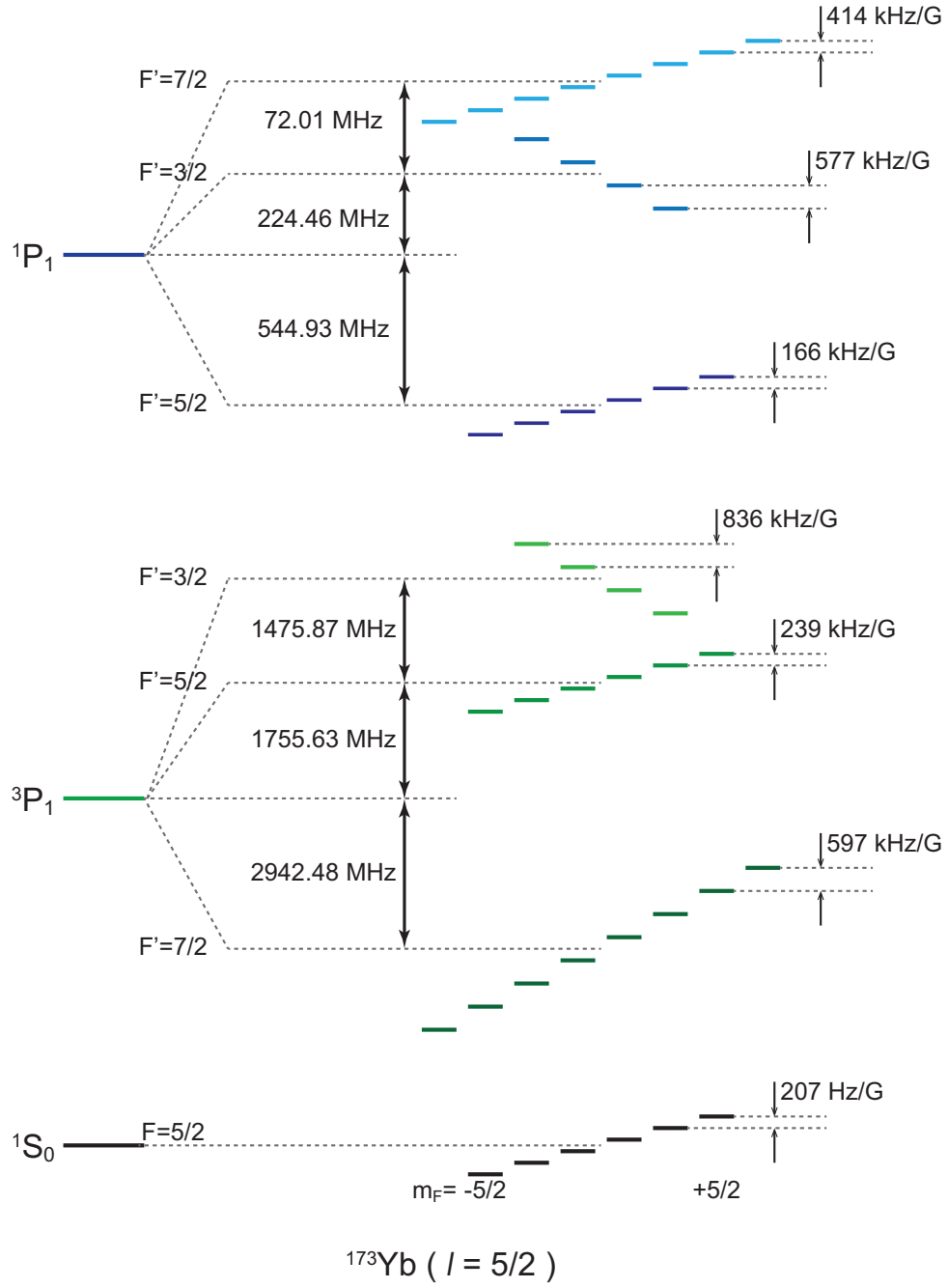
Figure 2.3: Magnetic sublevels of the most frequently used states, $^1S_0$, $^1P_1$ and $^3P_1$ of ^{173}Yb. The hyperfine splittings and corresponding Zeeman shifts are illustrated.

by using Zeeman energy become available [70–72]. Note that this is "magnetic" resonance, not the optical one.

2.2 Laser system

The two major transition lines for laser cooling ytterbium atoms have blue (398.9 nm) and green (555.8 nm) wavelengths. Unfortunately, the lasers at these two wavelengths are not commercially available. Alternatively, we decided to generate the proper laser lights using the fundamental laser and corresponding second harmonic generator (doubling cavity). This section describes how to create suitable laser lights for cooling the ytterbium atoms.

2.2.1 Laser for blue transition

We began with a blue laser diode (Nichia) to build ECDL(External Cavity Diode Laser) system at Littrow configuration [98]. The first strategy was to use one master ECDL and separately implement slave ECDLs via injection lock. This master-slave ECDL system for blue laser system had been used in Kyoto group, who guided the ytterbium quantum gas experiment since born. The scheme is cost-effective as well as less complicated. However, the blue laser diodes were unstable to support frequency lock and suffered severe mode-hoppings. The situation went even worse when the diode was subjected to operate at high input current: the single mode operation vanishes under the lab environment, which was quite as possible. It was almost like a lottery to find the acceptable product from the single die. Therefore, to overcome these problems, we decided to modify our plan to frequency doubling scheme, where a second harmonic generator (SHG) with fundamental laser is exploited.

Second Harmonic Generator

The fundamental laser light at 798.6 nm is emitted by a commercial diode-TA system (Toptica TA pro 798). To generate laser light at 398.9 nm, the fundamental laser beam is carefully shaped with anamorphic prism pairs and then incident to the SHG cavity. The principles of SHG system is discussed in M. Lee's thesis [99] (It is a nonlinear effect). The simple rule for constructing SHG is that the maximum conversion efficiency is achieved if the total loss per single round trip equals to the transmission of the input coupling mirror.

The SHG is composed of a bow-tie cavity with a AR coated LBO crystal (Raicol company). Since the LBO crystal degrades under humid environment, the complete cavity system is sealed with an acryl box filled with pure oxygen and frequently re-filled the gas with the new one. The dehumidifying agents (silica gel) are also put in the box. After the oxygen injection, we observed a slight increase in the total output power < 10 mW. For the future upgrade, it is recommended to use other gas because oxygen is dangerous for burning and explosion (although it never happened). The temperature of the LBO crystal is actively stabilized for some selected value near the room temperature ($21.5 \sim 23.2$ °C). Since the LBO crystal for blue transition takes angle-phase matching, which draws walk-off angle, the output beam has horizontally long slanted shape. A careful beam shaping is thus required for the output beam.

The cavity length is also stabilized by using Hänsch-Couillaud scheme, where the error signal is obtained by differentiating the absorption spectrum from different polarizations. To implement this scheme, the fundamental laser should be polarization maintaining and have well-defined single frequency mode along the frequency of interest ($\omega_{798.6} = 2\pi \times 375764$ GHz). The parameters of

cavity lock critically depend on the optics alignment and piezo length, which affect the quality of the error signal. Especially, a neutral density filter (Thorlabs NDC-50C-2-B), which reduces reflected beams in front of the input coupling mirror, gives small but observable drift in the error signal. The cavity lock is achieved by a PID of few tens of kHz bandwidth (SRS, SIM960) and is stable against typical noise sources in the lab for a day. The cavity lock is fast enough to follow the scanning speed of fundamental laser at few Hz rate for the frequency lock at the atomic reference. For fixed optimum cavity length, the conversion efficiency reach about 20%, where 270 mW of 398.9 nm light is obtained from 1.3 W input of 798.6 nm beam. Recent upgrade replaced the TA chip with the new one from Toptica, which emits CW 798.6 nm laser up to 2.8 W. The maximum achievable blue laser power using the new system is about 500 mW, which is five times larger than our required power for laser cooling.

The cavity optics were made of ultrastable mounts with low temperature drift hysteresis (Thorlabs 0.5 inch Polaris). Almost no significant alignment correction has been required over several months. Rather, the most drifting part was the optics inside the fundamental TA laser.

Because of UV nature of the blue laser lights, the system often suffered the damage from highly-energetic photons on the optics. Two critical parts were polarizing beam splitter cubes (PBSs) and optical fibers. The PBSs were burnt and showed yellow bright spot inside the cube interface although they were optical contact products (PBS25-405-HP). We occasionally replaced the PBSs before the input fiber (which reduces the fiber coupling efficiency) and before the input of Zeeman slowing (which diminishes the slowing efficiency) per 6 months of daily operation. The optical fibers also degraded at the end of the fiber tip by the power-induced long-term damage. To protect the fiber end from

32

the detrimental effect, it was managed with coreless end cap finish (OZ optics QPMJ-A3HPCA3HPC-400-3/125-3-7-1).

Spectroscopy

The stabilization of the blue laser frequency at the atomic reference is accomplished by performing modulation transfer spectroscopy (MTS), where the sidebands of the pump beam is transferred to the probe beam mediated by the atoms. The modulation (sideband) frequency for blue laser system is chosen to $2\pi \times 25$ MHz (Photonic technologies, EOM-02-25-U), which is similar to the atomic linewidth $\Gamma = 2\pi \times 29.1$ MHz. The transferred signal is detected by a home-made lock box. The error signal is delivered to the auxiliary port of Thorlabs Digilock system where the frequency lock is achieved. As an atomic source, hollow cathod lamp (HCL, Hamamatsu, L2738 Yb-Ne) operated by a high voltage power supply (SRS, PS310/1250V-25W) is employed. The typical runnning condition for the HCL is 177 V, 1 mA.

The blue laser lights are adopted for Zeeman slowing, which is detuned by ≈ 1 GHz from the atomic resonance $|^1S_0, F = 5/2\rangle \rightarrow |^1P_1, F' = 7/2\rangle$. To save the laser power resource from the loss due to AOMs, we take advantage of isotope shifts. For example, the error signal for ^{174}Yb is exploited to collect ^{173}Yb, where isotope shift grants ≈ 588 MHz shift. The details of the optics alignment and diagram of the blue laser system are illustrated in Figure 2.4.
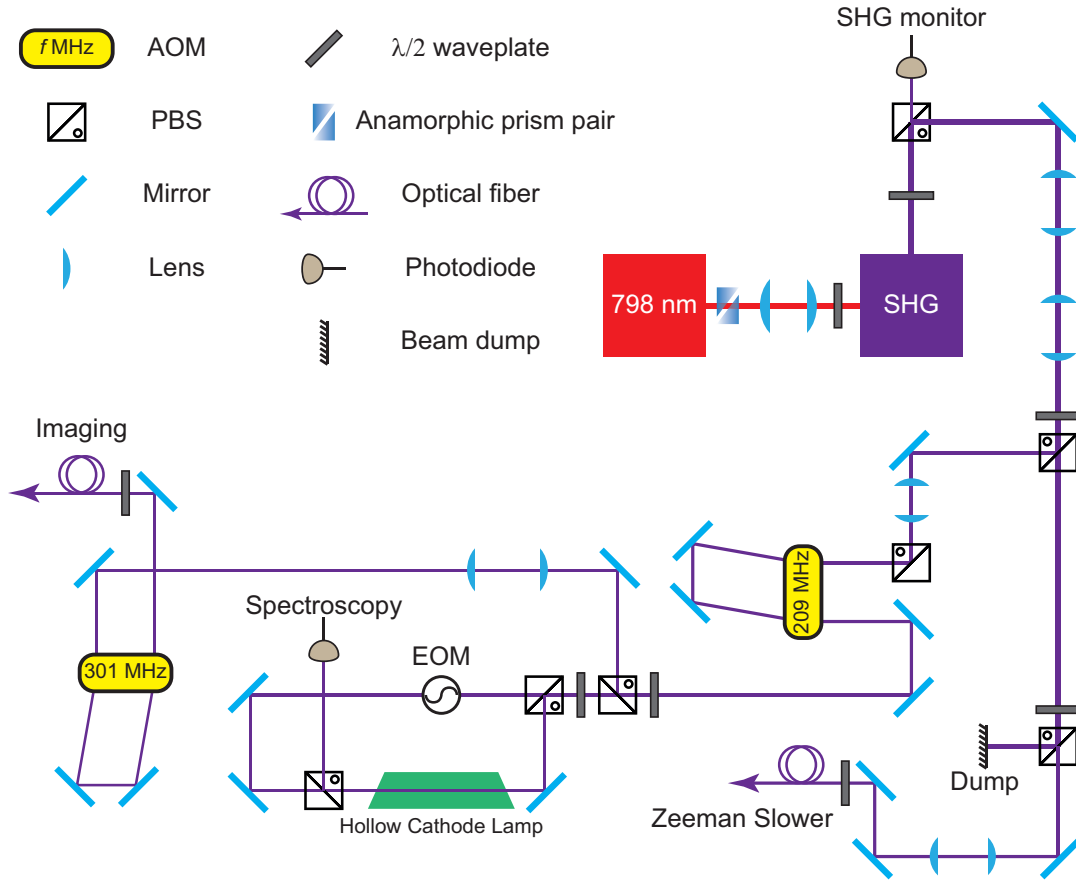
Figure 2.4: A schematic diagram for generating laser for the blue transition line. The fundamental TA laser beam is frequency-doubled by a second harmonic generator to create 398.9 nm laser, which is employed for Zeeman slower, spectroscopy, and imaging. In the above diagram, the frequencies of the AOMs are tuned to ^{173}Yb experiment. Since the AOMs are polarization dependent deflection efficiency, inconvenient double-pass configuration is employed.

2.2.2   Laser for green transition

Second Harmonic Generator

Similarly, we built another home-made SHG cavity system for the green transition of the ytterbium. The AR coated LBO crystal (Castech company) converts 1111.6 nm IR light generated by a commercial fiber laser (Menlo systems, Orange-1) into 555.8 nm. The linewidth of the fundamental laser is guaranteed to be $< 2\pi \times 50$ kHz, which is less than the natural linewidth of the green transition. Instead of angle phase matching, the temperature phase matching near 105 °C is adopted with absence of walk-off angle. The cavity length stabilization is achieved by Hänsch-Couillaud scheme as for the blue cavity and the typical conversion efficiency attains $\approx 20\%$, where the cavity output is 220 mW for 1.1 W of IR light. Recently, we purchased a new fundamental laser from Quantel (EYLSA-L-1111.6-3-P-SN-W-CO v2.0), which provides 2 W of IR light.

Spectroscopy

The MTS again fixes the frequency of the fundamental laser to the atomic reference. An EOM driven by a modulation frequency of 3 MHz (Photonic technologies EOM-02-3-U) is employed to obtain an error signal from the narrow intercombination transition. Because of small saturation intensity I_{sat} of the green transition, the portion of transferred signal is hard to detect. It is also significant to keep quite electronic environment, since small fluctuation of order of few mV may disrupt the lock (and therefore the sample) quality. We implemented a photomultiplier tube (Hamamatsu, PMT H10492) with 8 MHz bandwidth and carefully guarded the unwanted scattered lights. Since the atomic flux fogging inside the HCL was insufficient to produce error signal, we built an atomic cell

operated around 460 °C. The typical error signal appeared as peak-to-peak voltage scale of $\approx$ 400 mV for ^{173}Yb resonance. To prevent deposition of ytterbium atoms, the viewports were heated up to 150 °C and Ar gas ($\approx 10^{-6}$ torr to avoid pressure broadening) was filled as a buffer gas. The details of the green laser system are depicted in Fig. 2.5.

2.2.3 Laser for optical dipole trap

To perform an evaporation cooling, the ytterbium atoms are loaded into bichromatic crossed optical dipole trap consists of two CW high power lasers. First, the atoms collected in the MOT are transferred to the IR dipole trap, which has wavelength of 1070 nm and maximum power of 100 W (IPG photonics, multimode frequency, YLR-100-1070-LP). The beam power of the IR dipole trap laser is monitored by two battery-powered photodiodes (Thorlabs, DET36A/M), each of which regulates the laser for different power range via a PID feedback servo (SRS, SIM960). Because the IR laser has minimum emission power ($\approx$ 1 W), the overall power range is modified by a motorized rotating waveplate (Newport, PR50CC). To switch the dynamic range, a multiplexer (Analog devices, ADG5209) is employed. The focus of the IR dipole trap is designed to have elliptic beam waists of 26×72 μm to provide high trapping frequency against the gravity and to enhance transfer efficiency from the MOT by spatial mode-matching. Two cylindrical lenses are placed to shape this beam waist (See Fig. 2.10).

Another auxiliary, single frequency laser, which has wavelength of 532 nm (IPG photonics, GLR-20), is applied to create crossed dipole trap in the science chamber. The auxiliary trap has beam waist of 60 μm and PID-controlled by an
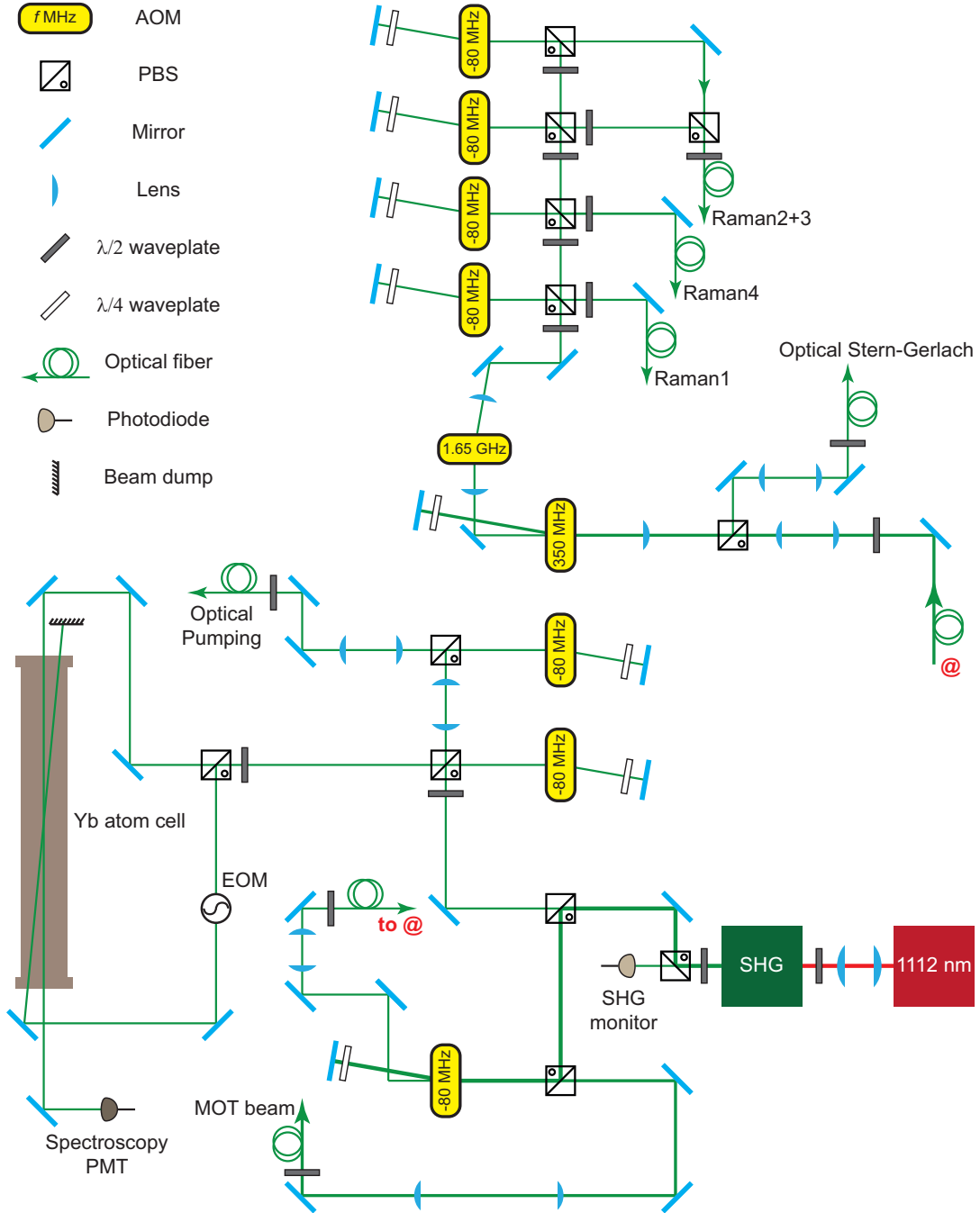
Figure 2.5: A schematic diagram for generating laser for the green transition line. Similar to the blue laser system, 555.8 nm laser is created by a second harmonic generator. The frequencies of the beams are manipulated for various purposes.

37

80 MHz AOM (AA optoelectronic, MT80-B30A1,5-VIS). The laser is delivered through the fiber to the science chamber. Later, we adopt another laser with the same frequency to create accordion optical lattice.

Because of high power nature of the dipole trap lasers, careful handle of optics should be required. To reduce thermal lensing, we tried to minimize the thickness of the optics component. For example, a thin plate polarizer was employed (CVI Melles-Griot, TFPN-1064-PW-1025-UV for IR, TFPN-532-PW-1025-UV for 532 nm) instead of a cube PBS. Also, it was helpful to use the optics made of fused silica instead of NK-7 materials. One of the critical part that may burnt was the fiber tip. The non-high power fibers (Thorlabs, P3-488PM-FC) suffered this issue and the coupling efficiency decreased daily; however, the fibers survived up to < 2 W of input power. For future perspective, it is beneficial to replace the fibers with the high-power end finish. Again, be careful when dealing with high power lasers; it may burn your AR coating of the viewport. Put on the protective glasses, although I have burnt some of my lab clothes.

2.2.4   Laser for optical lattice

Unwanted interferences between the lattice beams at each axis are alleviated by slightly shifting the frequencies of the lasers by tens of MHz. We employ four AOMs (two for 80 MHz, ± 110 MHz) where one of them has 80 MHz to generate aforementioned crossed dipole trap and another one with the same frequency for the lattice $1(\hat{y})$. Remaining two other AOMs produce ± 110 MHz lights for lattice $2(\hat{x})$ and $3(\hat{z})$, respectively. Each beam power is monitored by the battery-powered photodiodes (Thorlabs, DET series) and is actively stabilized by the servo (SRS, SIM960). The beam waists of the lattice beams are ≈ 85 μm and

the maximum applicable trap depths are 50 E_{R}. The lasers are derived from the same source (IPG photonics, GLR-20) and delivered to the science chamber through the fibers.

2.3 Vacuum system

In this section, the vacuum system of our ytterbium cold atom apparatus is described. In order to produce atomic samples with sufficiently long lifetime up to several seconds, UHV ($< 10^{-11}$ torr) is required to prevent one-body loss due to the background scattering from residual particles such as hydrogen, nitrogen, and etc. Although most of the experiments are done within 100 ms, because of harsh three-body loss mechanism for ytterbium cold atoms, our setup consists of UHV vacuum system with main and science chamber.

2.3.1 History of the system

In Nov. 2014, Bose-Einstein condensation of ^{174}Yb was produced. However, we were unhappy with the machine for three reasons: 1) The old machine had no science chamber and lacked optical access (viewports). Also, the old machine had no bucket window, which was necessary to implement high-resolution imaging system due to short working distance of an objective lens. 2) The vacuum measurement using ytterbium MOT showed strong one-body loss with short lifetime ≈ 25 s. We suspected that the outgassing from custom-made Zeeman slower tube and pumping body (Jeongmin Vacuum) was the main reason for bad vacuum status. 3) Due to the unstable support of ion pump magnet at the oven part, a critical leak was found (by He leak detection) and the pressure at the oven suddenly increased from 1×10^{-11} to 10^{-7} torr. Therefore, the replace-

ment of whole vacuum system was inevitable. At the turn of the year, M. Lee and I started to build a new machine from the ashes. The new design included science chamber with non-evaporative getter (NEG) pump (SAES CapaciTorr D50). In Apr. 2015, we successfully observed MOT again in the main chamber. In the fall of 2015, the degenerate Fermi gas of ytterbium atoms was created in the science chamber.

At Christmas of 2015, our master laser (1112 nm, Menlosystem Orange-1) was broken because its electronic board was burnt without any incident. M. Lee and I manually replaced the board at Feb. 2016. Since then, we started to study the effect of artificial gauge potentials on the ytterbium fermionic atoms.

But sadly, the joy did not last long. The lattice laser (532 nm, IPG GLR-20) was broken without any reason, and we were unable to maintain the experiment. We doubted that the alignment of harmonic generator at the end of the master laser was broken, but the only thing we could do is to send the laser back to the factory. We sent the lattice laser to the U.S. for repairs and it took more than a year (!). During the period, J. H. Kang and I studied photoassociation spectrum of bulk ytterbium atoms and M. Lee tried to realize dark-state optical lattice [100], which was later published first by NIST group [101]. It was not surprising that the atom shutter was broken twice by incorrect assembly of the rotational feed-through. The atom shutter was replaced with a new one and is now working correctly.

At the fall of 2017, the lattice laser came back and J. H. Kang and I started to reconstruct the whole system of the machine again. In that winter, we were able to begin the experiment about topological matters in synthetic lattices. Very recently, during preparing this dissertation, NI chassis, which controls all the apparatus, was naturally broken by aging. It was replaced with a new
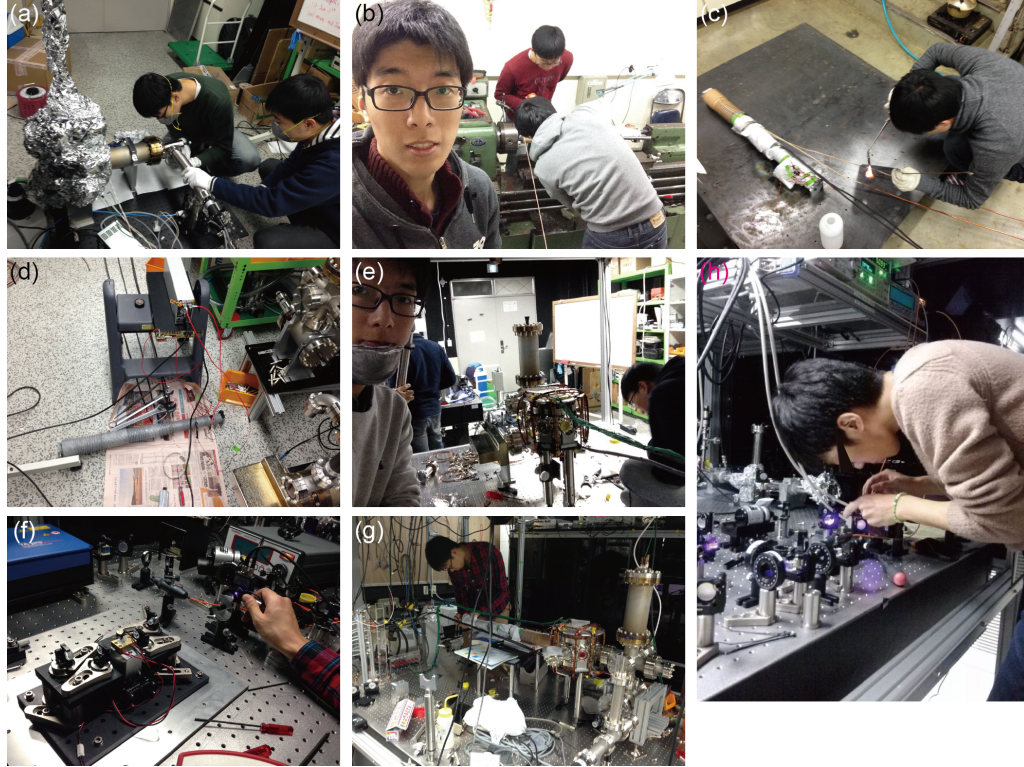
Figure 2.6: Photographs of the development of the machine. (a) Pre-baking of vacuum parts [Dec. 2014]. (b) Ytterbium team making Zeeman slower [Jan. 2015]. (c) M.-S. Kim welding copper water cooling pipes to Zeeman slower [Jan. 2015]. (d) Zeeman slower magnetic field test [Feb. 2015]. (e,f) Assembling the vacuum parts [Jan. 2015]. (g) M. Lee aligning the frequency doubling cavity [Apr. 2014]. (f) J. H. Han testing the blue laser system [Feb. 2015].

one, but the experiment had been stopped for several weeks.

2.3.2 Main machine

Most of the vacuum parts are made of the off-the-shelf products from the MDC vacuum. The main machine is composed of oven, Zeeman slower, and main/science chambers.

The bulk ytterbium chunk is located inside the cup made of stainless steel, which is boiled up to $\approx 390°$C. To prevent adhesive congelation of ytterbium atoms, the elbow is boiled up to $\approx 420°$C. At this temperature, the atomic beam bursts out from the nozzle at the average speed nearly ≈ 300 m/s. The nozzle is composed of a thin stainless steel plate with a hole diameter of 12.7 mm. Together with the differential pumping tube, the nozzle guides the atomic beam flux, which is carefully aligned to the center of the main chamber. The alignment of the flux direction was very critical to generate a large MOT, especially to the fermionic ytterbium isotopes, where the Zeeman slowing beam blows off the atoms. The on-and-off of the atomic beam is controlled by an atom shutter.

Oven has one Titanium sublimation pump (Agilent, 9160050) and one ion pump (Gamma Vacuum, 75L/s). Typical pressure reading at the ion pump is 8×10^{-11} torr at 190°C, while it is nominally 1×10^{-10} torr when the oven is operating (390°C).

The atomic beam reaches the Zeeman slower where the atoms began to slow down. The Zeeman slower is about 1 m long and has increasing magnetic field design toward the main chamber. An ion pump (45 L/s) is attached between the differential pumping tube and the entrance of the Zeeman slower. Typical pressure reading at this pump is about 7×10^{-11} torr (at 190°C, 1×10^{-10}

torr when operating). The magnetic coils are wrapped around a 0.75 m long hollow stainless tube, which fits to the 1.33 inch end of the Zeeman slower. The coils are water-cooled and separated to the laser system by a sorbothane sheet, which protects the machine against the vibrational noise. This vibrational noise from the water-cooling was the second most critical obstacle to attain quantum degenerate temperatures.

The main chamber is a spherical octagon chamber made from Kimball physics (MCF800-ExtOct-G2C8A16). Since it is the place where atoms are collected to the MOT and loaded into the dipole trap, three vacuum pumps–one Titanium sublimation pump (Agilent) with large pumping body, one NEG pump (SAES CapaciTorr D50), and one ion pump (Gamma Vacuum 75L/s) support the vacuum status inside the chamber. Typical pressure reading at the ion pump is 3×10^{-11} torr (at 190°C, 7×10^{-11} torr when operating), while the reading at an ion gauge (Agilent UHV-24, this cannot read below 10^{-10} torr) is 7×10^{-10} torr. In the new machine, the lifetime measured with the ytterbium MOT showed ≈ 40 s. The top and bottom viewports are AR coated for blue (399 nm) and green (532, 556 nm) lasers, and the side viewports are AR coated for green and IR (1064, 1070 nm) lasers.

2.3.3   Science chamber

The hexagonal science chamber (Kimball Physics, MCF275-SphHex-Cc2A6) is attached to the main chamber for better optical access and imaging. The quantum degeneracy of ytterbium atoms are achieved in this science chamber. The distance between the center of the main chamber and that of the science chamber is about 345 mm. Again, the water-cooled high magnetic field coils, which
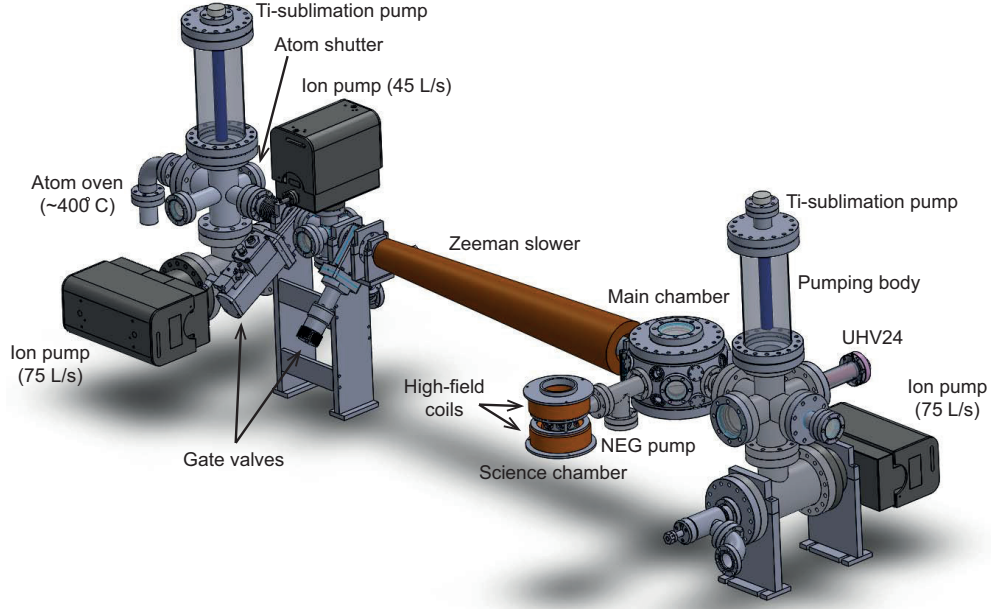
Figure 2.7: CAD diagram of vacuum apparatus for generating ytterbium quantum gas.

can produce the magnetic field up to 0.166 T, are located outside the chamber, where sorbothane sheets absorb vibrational noise from it. Similar to the main chamber, the top and bottom viewports are AR coated for blue (399 nm) and green (532, 556 nm) lasers, and the side viewports are AR coated for green and IR (1064, 1070 nm) lasers.

2.4 Control system

Thanks to A. Keshet, we have been implemented Cicero and Wordgenerator to control over the apparatus for various experimental sequence. The sequential

orders are programmed to National Instrument (PXI-1033) digital/analog cards (PXI-6534/6713), where each order runs at the exact time within a resolution below < 1 μs. The FPGA (Opal Kelly Xilinx 11480002CN) is used as a base clock of the system.

2.5   Preparation of cold ytterbium quantum gas

This section illustrates the typical experimental procedure to reach quantum degeneracy of ytterbium atoms. The experimental cycle begins with decelerating down the atoms using Zeeman slower and magneto-optical trap (MOT). After the transport of atomic cloud into the science chamber, evaporation cooling by decreasing the trap depth is employed to generate ultracold ytterbium quantum gases.

2.5.1   Zeeman slower

The atomic flux ejected from the oven gets slow down by unidirectional photon scattering along the Zeeman slower. The resonance condition is always maintained by compensating Doppler shift with Zeeman effect. The velocity profile of the atomic beam, which has Boltzmann distribution with average velocity 300 m/s, accumulates below the final target velocity about 10 m/s within a distance of 1 m.

The optimum velocity profile $v(z)$ can be obtained by considering the magnetic field profile using the energy conservation law,

$$\frac{m}{2} \left(v^2(z) - v_0^2 \right) = \int \hbar k R(z) dz, \qquad (2.5)$$

where m is atomic mass, $v(z)$ is the velocity of the atom at z, k is the photon

momentum, and $R(z) = \frac{\Gamma}{2}\frac{I/I_{\text{sat}}}{1+I/I_{\text{sat}}}$ is the scattering rate. The intensity of the laser increases as $I(z) = P/(\pi r^2(1+\kappa z)^2)$, where P and r are the incident laser power and radius, respectively, and κ is the slope of the ray. Then the magnetic field should satisfy $\mu_{\text{B}}g_F m_F B + kv + \hbar\Delta\omega_{\text{ZS}} = 0$, where $\Delta\omega_{\text{ZS}}$ is the detuning of the Zeeman slowing light. In our experiment, we use σ^- polarized $P = 55$ mW of $\lambda = 398.9$ nm blue beam, which is detuned by $\Delta\omega_{\text{ZS}}/(2\pi) = -1$ GHz to the $|^1\text{P}_1, F' = 7/2\rangle$ resonance. For ^{173}Yb, this detuning is closely located to $F' = 5/2$ state and this unusual hyperfine structure of the fermionic ytterbium scatters the atoms captured in MOT. This detrimental effect is amended by placing a dark spot (≈ 4 mm diameter) at the Zeeman slowing beam center to suppress the scattering event on the atoms.

It is worth to mention that as the radius of the Zeeman slower coils grows, the residual magnetic field smearing out to the main chamber increases as well. We reduced this unwanted magnetic fields by operating slower compensation coil together with several mu-metals located in between the Zeeman slower and the main chamber.

2.5.2 Magneto optical trap

The decelerated atoms are then captured in the magneto-optical trap (MOT), where its basic principle is just 6-way extension of the Zeeman slower. Key feature of the MOT is to make atoms scatter photons in a position-sensitive manner where an atom deviating from the center of the zero magnetic field point is pushed back to the center. To do this, the laser beams with proper polarizations are irradiated from 6 directions and an anti-Helmholtz magnetic field is adopted. The minimum "theoretically" achievable temperature is lower-bounded
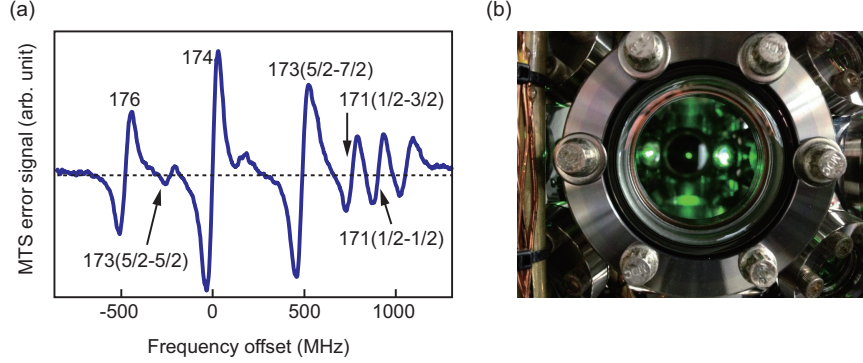
Figure 2.8: (a) The error signal obtained from modulation transfer spectroscopy (MTS) using 398.9 nm blue transition of ytterbium atoms. To save the laser beam power, isotope shifts are exploited instead of using AOMs. (b) Magneto optical trap (MOT) of ^{174}Yb atoms.

by a unit photon recoil momentum and is estimated to $T_{\mathrm{D}} = \hbar\Gamma/(2k_{\mathrm{B}}) = 4.4\ \mu\mathrm{K}$ for green MOT of the ytterbium. Because of small linewidth of the green transition $\Gamma(^3\mathrm{P}_1)/(2\pi) = 182$ kHz, the Doppler temperature is small, but provides slow loading rate. To enhance the loading rate, we modulate the frequency of the green MOT beams (dithering) by 25 Γ with speed of 200 kHz to increase the trapping volume and capture velocity [47]. As a result, more than 10^8 atoms are collected in the MOT within 15 s. For your information, a powerful method called core-shell scheme to boost up the loading rate by utilizing both blue and green transition is developed recently [62]. To increase phase space density, we cool the MOT by simultaneously decreasing the MOT beam intensity, reducing the dithering amplitude, and approaching the detuning of MOT beams toward the resonance. At the final stage, the atomic cloud is compressed by increasing magnetic field gradient to 7.9 G/cm to have temperature about 20 $\mu\mathrm{K}$. The details of the experimental sequence is summarized in the Fig. 2.9.
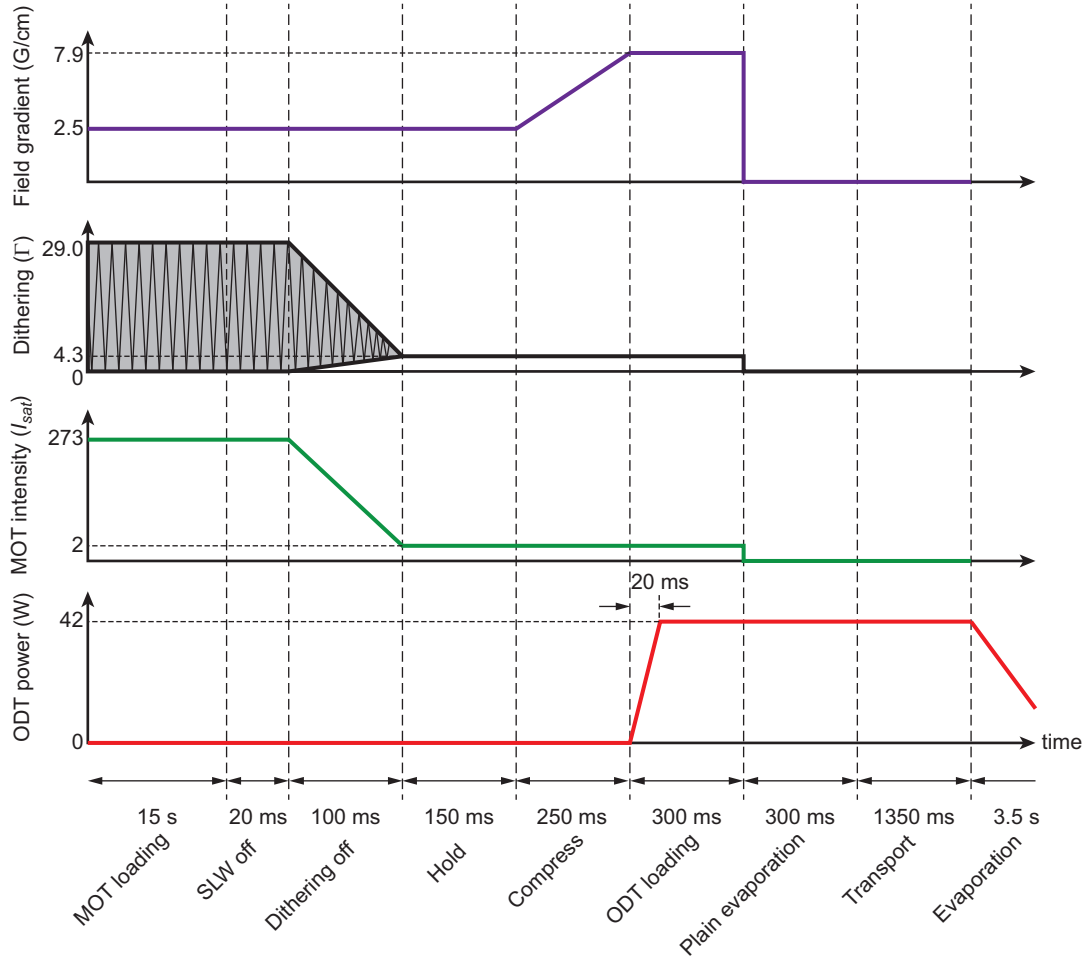
Figure 2.9: Schematic diagram of early part of the typical experimental sequences, when the apparatus collects atoms in a MOT and load the atomic cloud into an IR ODT. The figure is not to scale.

2.5.3 Transport and crossed dipole trap

The compressed atoms are transferred to an IR optical dipole trap (ODT) formed by a focused 1070 nm laser beam, where the transfer efficiency is $\approx 13\%$. The 1×10^7 atoms of ^{173}Yb are held in the 42 W of IR ODT. Then, the atoms are transported to the science chamber, which is appendant to the main chamber, for better optical access and capability of high magnetic field. The transport system is composed of three parts: a pair of cylindrical lens to make elliptical Gaussian beam, a lens to make tight focus, and another pair of lens comprising 4-f system with magnification $M = 400/175 \approx 2.3$ to project the focus. In this system, the focus is shifted by $M^2 d$ as the focusing lens moves by d and the beam waist is kept constant during the transport [99]. To transport the atoms, the focusing lens is mounted on an air-bearing translational stage (Aerosystem, ABL1000), which smoothly shifts the trap center by mechanically moving the lens. The PID values and velocity profile of the moving translational stage is empirically found. The transport system shifts the ODT focus within 1.65 s to a science chamber with the transport efficiency about 85%.

After the transport, an additional 2 W of 532 nm auxiliary dipole trap beam is focused to the atomic sample horizontally. The angle between the two dipole trap beams is 60°.

2.5.4 Bose-Einstein condensation and degenerate Fermi gas

The quantum degeneracy is achieved by evaporative cooling the atoms inside the crossed dipole trap. To decrease the temperature of the total system, the trap depth is slowly reduced to selectively release highly energetic atoms in the trap.
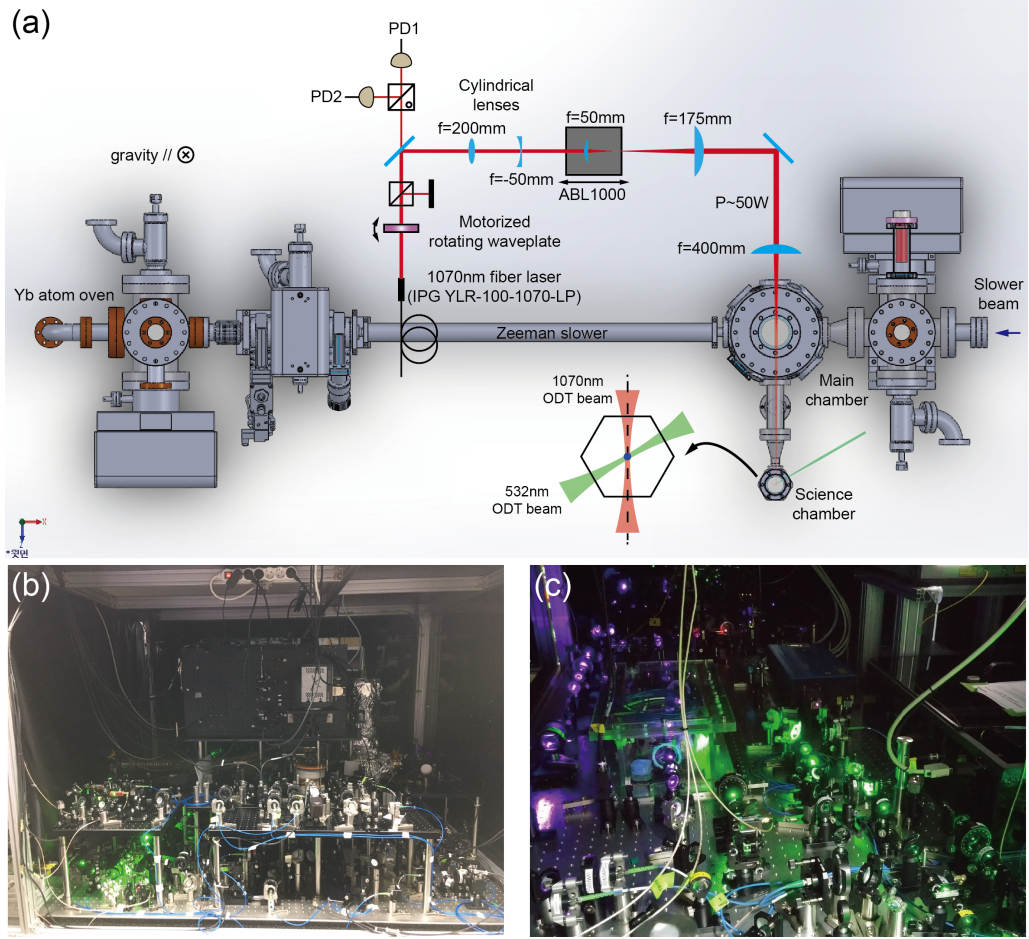
Figure 2.10: Images of the ytterbium machine. (a) 3D CAD image (topview) of the apparatus. A scheme to transport atoms into the science chamber and crossed dipole trap is illustrated. (b) A photograph (side view) of the vacuum system. (c) A photograph of the laser system.

The elastic collision between the atoms redistribute the thermal energy of the atoms to have certain distribution (Maxwell-Boltzmann for classical temperature regime, Bose-Einstein/Fermi-Dirac for quantum degenerate temperatures) after getting rid of hot atoms. We empirically found the optimum evaporation curve by following the rule: looking for the time duration with maximum phase space density when the trap depth is linearly decreased by half. After 6 to 7 steps, which take ≈ 3.5 s, Bose-Einstein condensation of ^{174}Yb is created below the critical temperature of $T_c = 700$ nK. Similarly, unpolarized degenerate Fermi gas of ytterbium of atom number 10^5 and temperature $T/T_F = 0.1$ is successfully generated, where $T_F \approx 200$ nK is the Fermi temperature of the trapped sample. The temperature of the Fermi gas is obtained by Thomas-Fermi fit of momentum distribution (measured by time-of-flight) of the atomic cloud, which deviates from the ordinary Gaussian wing fit. We also verified Eq. 1.10 safely holds by measuring the temperature manually using the size of the cloud for different time-of-flight durations. The typical trapping frequencies are estimated to $\omega_{x',y',z} = 2\pi \times (30, 105, 146)$ (Here, $\hat{x}'$ is chosen along the direction of green dipole trap.), which is measured by kicking the atoms by suddenly moving one of the trap using the PZT attached to the mirror.

2.5.5   Optical lattice

The optical lattice is constituted by two orthogonal retroreflected beams ($\hat{x}$ and $\hat{z}$) and one in an accordion style ($\hat{y}$). The auxiliary dipole trapping beam and additional lattice 1 beam, both of which have $\lambda_L = 532$ nm, interfere to create the lattice, where the intersection angle is 60° and the lattice spacing is increased to $d_y = \lambda_L/\sqrt{3}$ ($d_{x,z} = \lambda_L/2$). To load the atoms into the optical lattices,
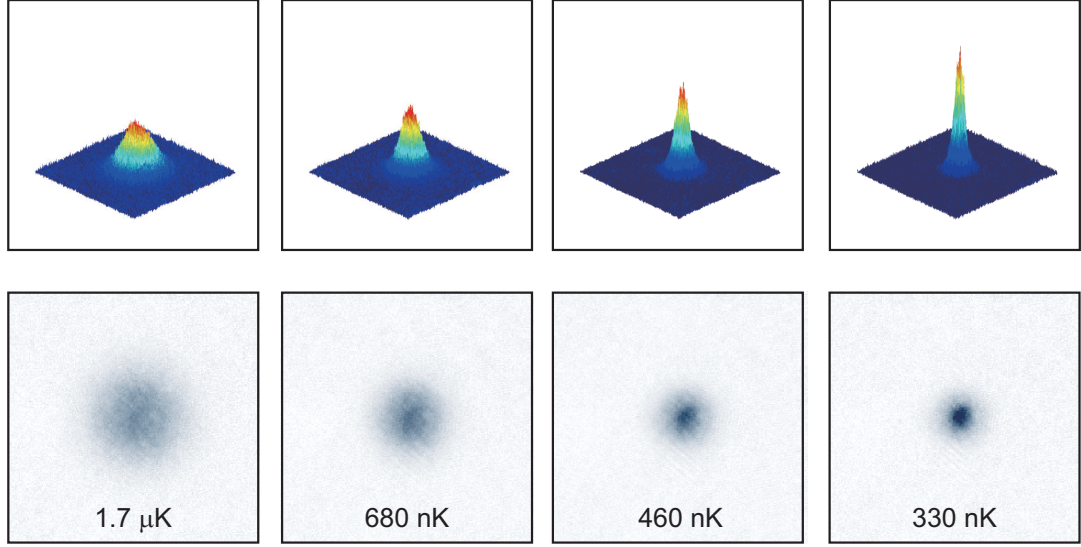
Figure 2.11: Bose-Einstein condensation of ^{174}Yb, where the transition takes place near $T_{\mathrm{c}} = 700$ nK. The momentum distribution is obtained by an absorption image taken after 15 ms of time-of-flight. The cloud exhibits bimodal density distribution since all the excited states are saturated by quantum statistics and the ytterbium atoms below T_{c} occupy the same momentum state.

the lattice beams are exponentially ramped to the target value within 70 ms and $\tau = 0.05$ s. The adiabaticity is guaranteed by measuring the population occupying excited bands, which is less than 3%. To ensure thermal equilibrium, the lattice depth is typically held for another 20 ms. During the lattice ramp up, the ODT depth is linearly decreased to counterbalance the overall trapping potential.

To detect momentum distribution (Brillouin zone) of atoms in the optical lattice, especially for fermionic isotopes, usual band-mapping technique is employed [6]. The lattice depths are linearly ramped down to zero for 1 or 2 ms, where the absorption image of the cloud is taken after the 15 ms of free
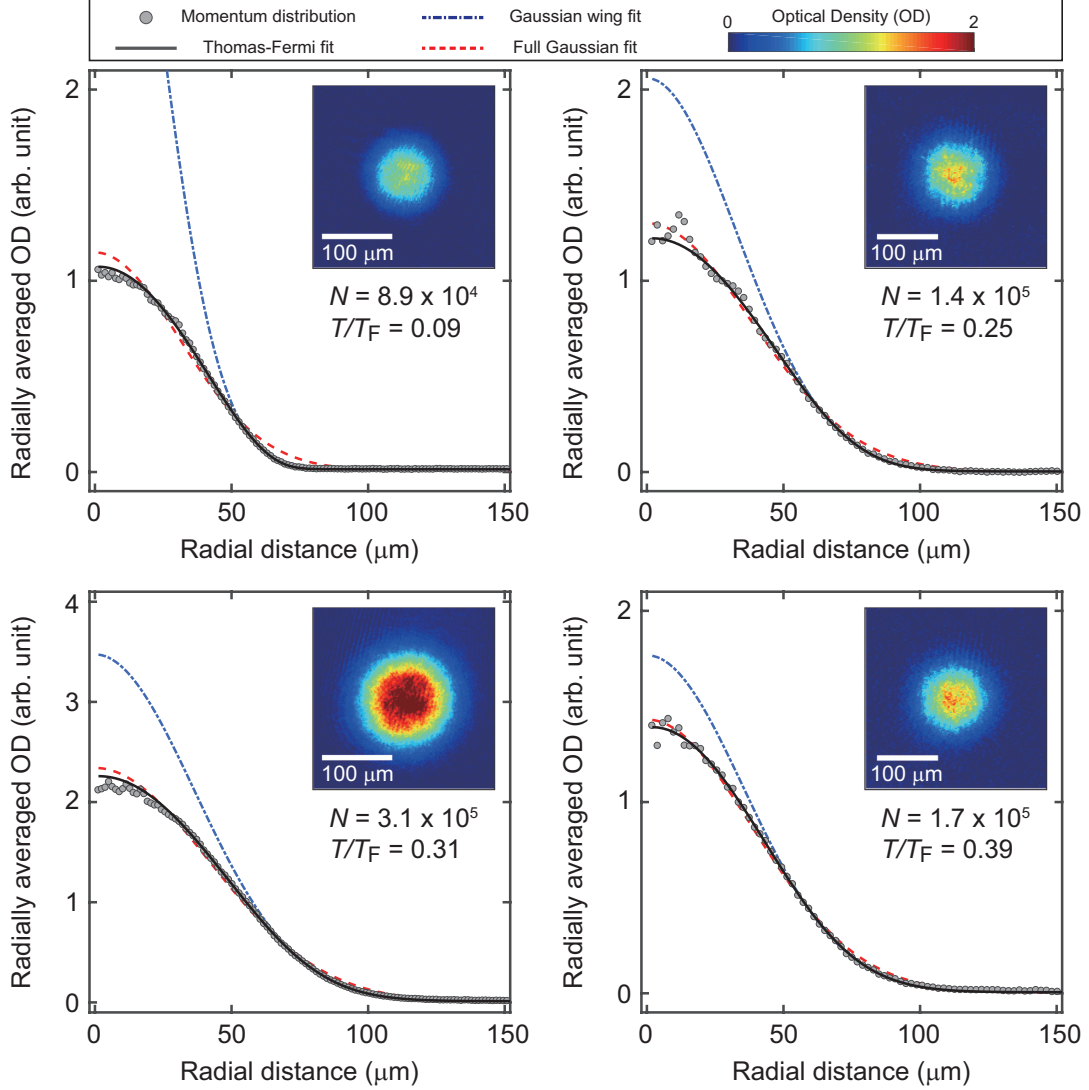
Figure 2.12: Degenerate Fermi gas of ^{173}Yb with six spin components. The momentum distribution is obtained by an absorption image taken after 15 ms of time-of-flight. In contrast to the bosonic gases, the radially averaged optical density (OD) of fermions is fitted with a Thomas-Fermi distribution, which assigns suppression of atomic density in the center of the cloud due to Pauli exclusion. The temperatures of the gases are estimated by these fittings. Notice that the momentum distribution deviates from either full or wing Gaussian fit.
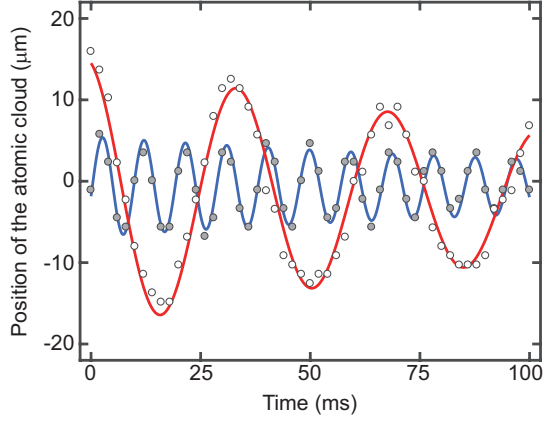
Figure 2.13: Measuring trapping frequencies of bichromatic crossed dipole trap by kicking the ^{173}Yb atomic cloud and observing its center-of-mass oscillation in the $\hat{x}$-$\hat{y}$ plane. Each data for $\hat{x}'$ (empty circles) and for $\hat{y}'$ (filled circles) is fitted with an equation $\tilde{x}(t) = \tilde{a}e^{-t/\tau}\cos(2\pi\omega_j t + \tilde{\phi})$ (red and blue lines, respectively), where ω_j are the trapping frequencies along the principal axis (x', y', z). The trapping frequencies are estimated to $\omega_{x',y'} = 2\pi \times (30, 105)$.

expansion. The mapping rate is chosen to be faster than the harmonic trapping potential to prohibit distortion from it and to be slower than the energy gap of the lattice to preserve the momentum space information.

2.6 Detecting and manipulating nuclear spin states

The atomic cloud is detected by employing the standard absorption imaging technique and its spin components are controlled by using optical pumping method. This section describes how to detect and manipulate nuclear spin states of fermionic ytterbium atoms in the degenerate temperatures.
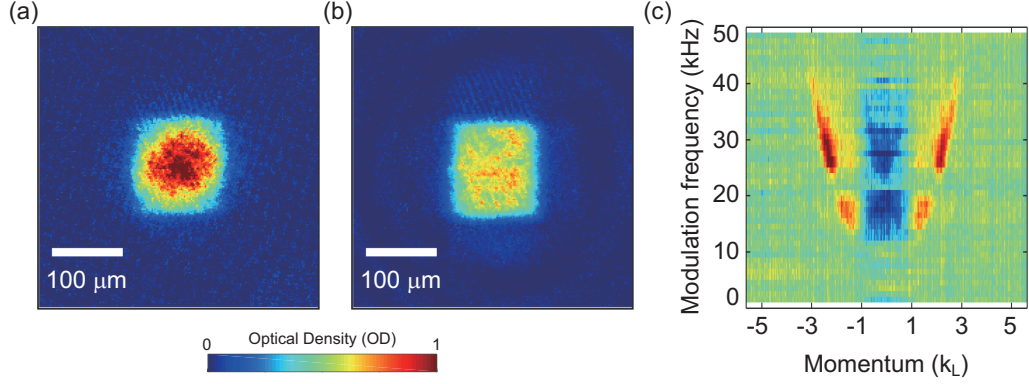
Figure 2.14: Momentum space (Brillouin zone) distribution obtained by a band-mapping sequence, where the lattice potentials are adiabatically turned off. (a) The Brillouin zone of atoms loaded in the 3D lattice of depths $5E_{\mathrm{R}}$. Only the lowest Bloch band is populated. When the lattice depth is low, the atoms become metallic and the edge of the Brillouin zone is not completely occupied. (b) The Brillouin zone of 3D lattice of depths $20E_{\mathrm{R}}$. The aspect ratio is due to the different lattice spacings because of the accordion style alignment. (c) The lattice depths of each direction are calibrated by fitting multiband modulation spectroscopy [102] signal, which is obtained by stacking up the BZ sum for different modulation frequencies, to the known band dispersion.

2.6.1 Absorption imaging

One way to detect the atomic sample is to take an absorption image of the cloud. It is a destructive method, which produces a quick and clear signal. The principle of absorption imaging is to record a shadow of the atomic sample on a CCD camera (Andor iXon ultra 888 for science chamber and PCO pixelfly USB for main chamber) after the cloud is exposed to laser irradiation. The resonant photons are scattered from (absorbed to) the atoms and the intensity of the light is reduced at the sample position. To shorten the interrogation time, closed dipole-allowed transition is preferred, such as blue transition ($\lambda =$

398.9 nm, $|^1S_0, F = 5/2\rangle \rightarrow |^1P_1, F' = 7/2\rangle$ although it is approximately cyclic) for ytterbium atoms. The intensity of the transmitted light can be calculated using the Beer-Lambert law,

$$I(x, y) = I_0(x, y)e^{-\sigma \int n(x,y,z)dz}, \tag{2.6}$$

which assumes the low intensity limit. Here, $I_0(x, y)$ is the initial intensity profile of the probe beam, $\sigma = 3\lambda^2/(2\pi)$ is the resonant scattering cross section, and $n(x, y, z)$ is the density of the atomic sample. To minimize noise, an absorption imaging takes three shots: 1) imaging with atoms S_{ij}, 2) without atoms N_{ij}, and 3) without imaging beam itself for background noise calibration B_{ij}. Then the column density integrated along the axis of the probe beam appears on the screen as,

$$\tilde{n}(x, y) = \int n(x, y, z)dz = -\frac{A}{\sigma} \ln\left(\frac{S_{ij} - B_{ij}}{N_{ij} - B_{ij}}\right), \tag{2.7}$$

where A is the total pixel area (13 μm×13 μm for Andor and 6.45 μm×6.45 μm for PCO) taking the magnification of the imaging system into account. The magnification of our imaging system in science chamber is about ×6.5 (×2 for main chamber), which is calibrated using the Raman pulse. The resolution of our imaging system is determined by an objective lens (Mitutoyo telecentric) below 2.18 μm, which is measured by USAF1951 test pattern. The typical exposure time for ^{173}Yb is 100 μs per a shot and the intensity of the imaging beam is $\approx 0.02\ I_{\text{sat}}$, which safely admits the low intensity approximation. Depending on the polarization and the external magnetic field, the transition line strengths $|C_{F',m_F}(\epsilon)|^2 \alpha_{JJ'}$ should be considered as a multiplicity factor to correctly detect the number of the atoms in the specific spin component.
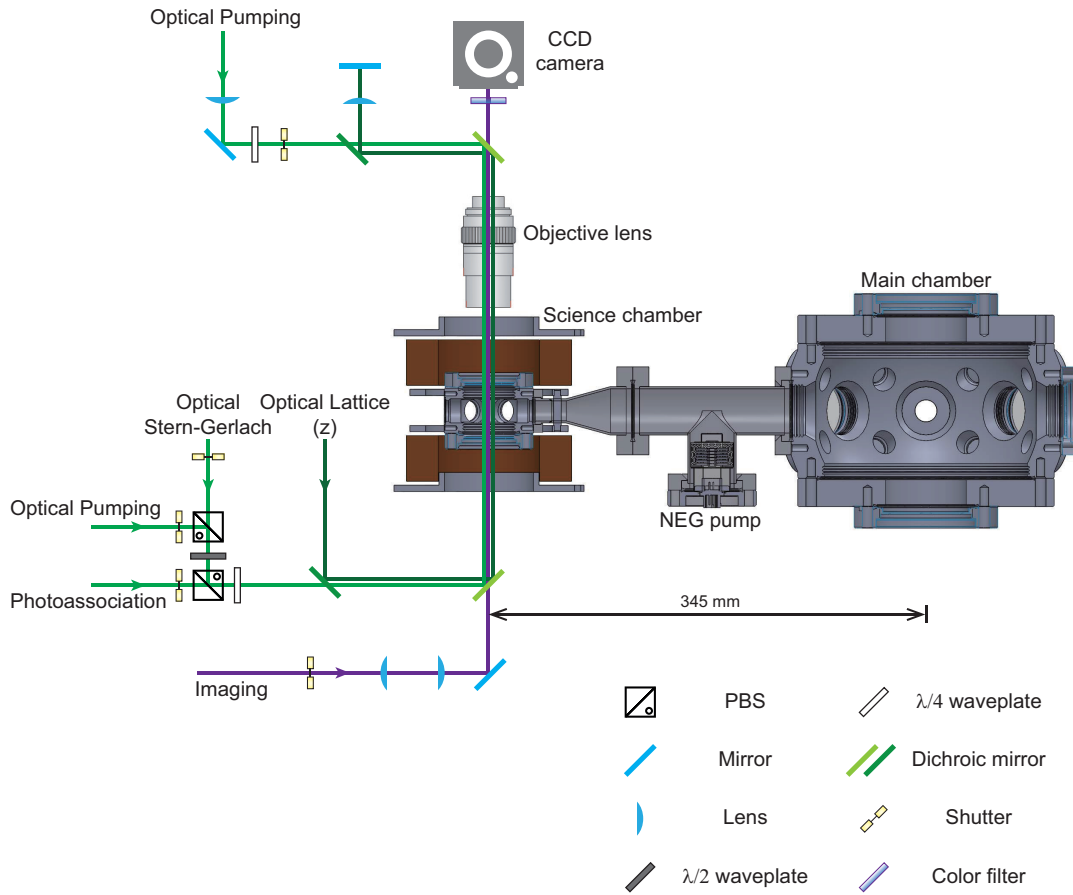
Figure 2.15: Schematic diagram of vertical alignment in science chamber. The beams are distinguished by several dichroic mirrors. To avoid detrimental effect due to high intensity of the optical lattice beam, the reflective side is exploited for dichroic mirrors.

2.6.2 Optical Stern-Gerlach effect

The absence of (electronic) magnetic moment in the $^1S_0$ ground state makes difficult to resolve each nuclear spin component using ordinary magnetic Stern-Gerlach method. A simple calculation estimates that the required magnetic field gradient is 10^3 times larger than the case of an alkali atom. Instead, for ytterbium atoms, an optical Stern-Gerlach (OSG) method is used to separate out the nuclear spin components of the atomic sample.

The principle of the OSG is to take advantage of differential AC Stark shift between the spin components. For a near resonant lights, the AC Stark shift is different for each spin state, which produces spin-dependent optical potential. When an atomic cloud is located at the side of Gaussian intensity profile, the atoms perceive spin-dependent dipole force, which resolves each spin component in the cloud. The spin state-dependent AC Stark shift can be calculated by using Eq. 1.17 and corresponding numerical code is provided in the Appendix D.

In our experiment, the atomic cloud is illuminated by 4 ms of OSG beam which is detuned by $+860$ MHz from the green transition line, $|^1S_0, F = 5/2\rangle \rightarrow |^3P_1, F' = 7/2\rangle$, after switching off all the trapping beams. Then, the atoms are allowed to expand freely for 6 ms and detected by the absorption imaging. Typical images for various spin mixture samples are displayed in Fig. 2.16.

2.6.3 Optical pumping method

It is also possible to initialize the composition of nuclear spins in the atomic cloud by using optical pumping method. In this method, the atoms in spin state $|^1S_0, F = 5/2, m_F\rangle$ are transferred to the excited state $|^3P_1, F' = 7/2, m_{F'} = m_F + \epsilon\rangle$ depending on a polarization of the optical pumping beam $\epsilon = \pm1$ or 0.
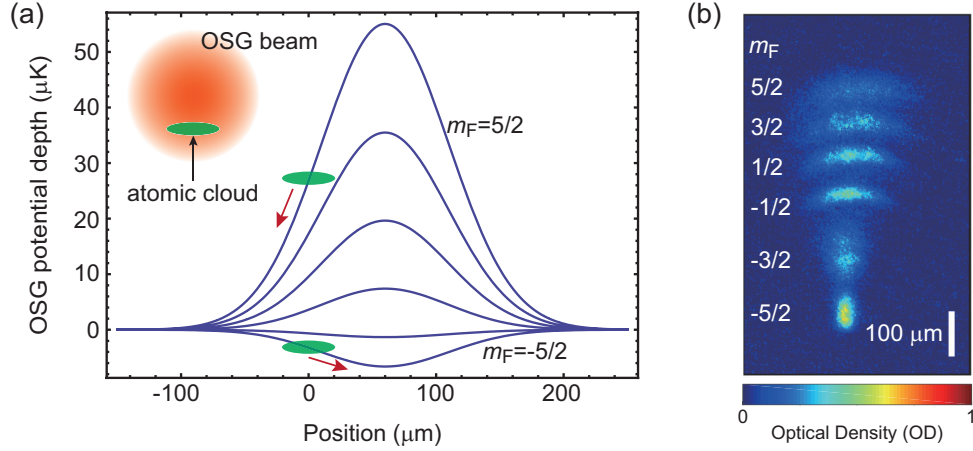
Figure 2.16: The principle of optical Stern-Gerlach (OSG) effect. (a) Calculated differential dipole potentials for each spin component induced by an OSG beam of waist 100 μm and power 5 mW. The atomic cloud (green) experiences spin-dependent dipole force (red arrow) and is spatially resolved by each spin component. (b) Typical experimental absorption image taken after radiation of OSG beam by 4 ms and then 6 ms of free expansion of the atomic cloud.

Then, the atoms fall back into the target spin state in the ground manifold via spontaneous emission under the general selection rule. The narrow transition linewidth of $^1S_0 \rightarrow ^3P_1$ allows us to manipulate spin components with arbitrary ratio by using the optical pumping protocols.

In our experiment, we adopt a pair of optical pumping beams each of which has $\sigma^\pm$ polarization to selectively excite specific spin state. The pumping beams propagate along the vertical axis ($\pm\hat{z}$, respectively), which coincides with the imaging and the quantization axes. The two pumping beams are independently controlled, where σ^- beam is acquired from the MOT beam. An external magnetic field of $B \approx 16.6$ G is sufficient to resolve excited spin manifold ($^3P_1, F' = 7/2$) which has Zeeman splitting of each level by $\Delta_Z/(2\pi) =$

$0.597 \cdot B$ kHz.

To avoid heating from the scattered photons, it is beneficial to apply the optical pumping beams before the evaporation stage. However, for some circumstances, we implement additional optical pumping beams after the evaporation sequences to clear out residual spin components. The optical pumping beams illuminate the *in situ* atoms with a typical pulse length 25 ms per a pulse in the early stage of evaporation while it shrinks down to 2 ms after the evaporation. The atomic cloud produced in this way has slightly higher temperature than the original sample. As the number of spin components in the atomic cloud decreases, efficiency of the evaporation cooling drops because of Pauli exclusion. Therefore, to create a spin-polarized sample, for example, we prepare two component mixture and then perform evaporation cooling. After the evaporation stage, we get rid of the unwanted spin component by applying a blowing off pulse. In this method, we were able to generate spin-polarized ytterbium fermions at $|F = 5/2, m_F = -5/2\rangle$ with the atom number 10^4 and the temperature $T/T_{\mathrm{F}} = 0.2$.

2.6.4 Spin-selective imaging

The inhomogeneous intensity profile of the OSG beam destroys the momentum space information of the atomic cloud, which can be measured by a spin-selective imaging. There are two ways to adopt the spin-selective detection of the atomic sample: 1) To take an absorption image which is resonant only to the target spin state and 2) to blow off the unwanted spin components by a blast pulse. In the former case, a large magnetic field of ≈ 350 G is necessary to resolve adjacent spin components by at least 5Γ for imaging blue transition line, which
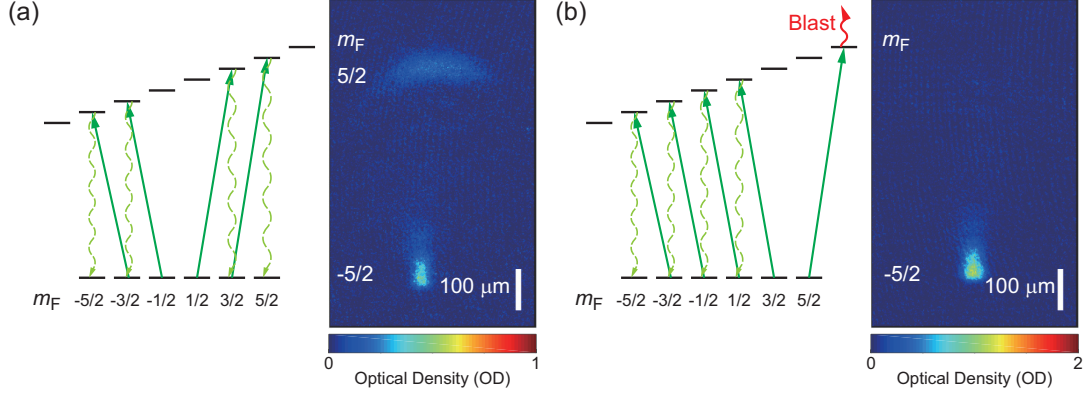
Figure 2.17: Exemplary OSG images of atoms optically pumped to initialize various spin mixture samples. (a) Two spin mixture ($m_F = \pm 5/2$) sample. (b) Spin-polarized ($m_F = -5/2$) ^{173}Yb sample.

bears $\Gamma(^1P_1)/(2\pi) = 29.1$ MHz. We also tried to implement $^3P_1$ spin-selective imaging, but weak saturation intensity of the dipole-forbidden transition yielded a poor signal-to-noise ratio of the absorption image.

In the latter case, a blast pulse of 2 ms duration is applied at the early stage of time-of-flight expansion to selectively eliminate unwanted spin components in the cloud. In this way, a clear momentum space information of specific spin is obtained. One drawback of this method is that the signal from different spin states cannot be measured at the same time. In our experiment, a series of experiments has been carried out to capture every data. It is also worth to be noted that the eddy current around the metallic chamber, due to the abrupt change in external magnetic field, produces residual magnetic field, which impedes the blast pulse not to be resonant to the target state. The eddy current can be ameliorated by implementing the science chamber made of nonconductive material such as a glass cell.

Chapter 3

Raman two-photon transition

Fermionic ytterbium atoms provide a perfect platform for studying topological matters. To realize, one needs to generate artificial gauge potentials (fields) on the neutral atoms. A typical way is to implement Raman two-photon transition between given quantum states (psuedospins) of the atoms. The hyperfine spins of ground manifold of fermionic ytterbium, which have sub-MHz narrow linewidth for the transitions to intercombination line, can afford new type of Raman-dressed synthetic material with low heating rate. In this chapter, I discuss basic principles of Raman two-photon transition and its applications. This work is mostly related to the published results in the following papers.

- M. Lee, J. H. Han, M.-S. Kim, and Y. Shin, *"Gauge Field for Neutral Atoms near a Current Loop,"* Jour. Kor. Phys. Soc. **65**, 2053 (2014).

- M. Lee, J. H. Han, J. H. Kang, M.-S. Kim, and Y. Shin, *"Double resonance of Raman transitions in a degenerate Fermi gas,"* Phys. Rev. A **95**, 043627 (2017).

Table 3.1: Fine structure splitting of various atoms [21]

Elements	^{87}Rb	^{40}K	^{6}Li	^{173}Yb
Fine structure (Δ_{FS}/h)	7.1 THz	1.8 THz	10 GHz	$\gg 100$ THz

3.1 Basic principles of Raman transition

Raman two-photon transition is a spin-changing Bragg transition between the two inner quantum states, or pseudospins, of an atom. Two Raman photons induces transition probability between these pseudospins, mediated by a virtual excited state. The hyperfine spins of a cold atom is a useful candidate for realizing a Raman two-photon transition. Since a photon can alter only the angular momentum $\mathbf{L}$ of the atom, the strength of Raman coupling is proportional to the LS-coupling Δ_{FS}, which increases as atomic mass gets bigger. Thus, atomic candidates with large fine structure splitting is preferred to generate proper strength of Raman coupling. The Raman coupling strength is $\propto \Delta_{\mathrm{FS}}/\Delta^2$, where Δ is the detuning from the excited states [21]. In table 3.1, the values of fine structure splitting of major elements used in cold atom society is presented.

It is also worth to note that small linewidth of ytterbium atom provides low heating loss due to the spontaneous emission after the Raman process. As mentioned in Eq. 1.14, the off-resonant photon scattering rate is $\propto \Gamma/\Delta^2$, where Γ is the natural linewidth of the transition [21, 103].

In this section, a system which have two long-lived ground states (in most cases, hyperfine Zeeman sublevels of an atom) are coupled via an radiative excited state is introduced. In the following descriptions, many types of rotating frames (nothing but the gauge transformations) are adopted–so stay focused and do not get dizzy!
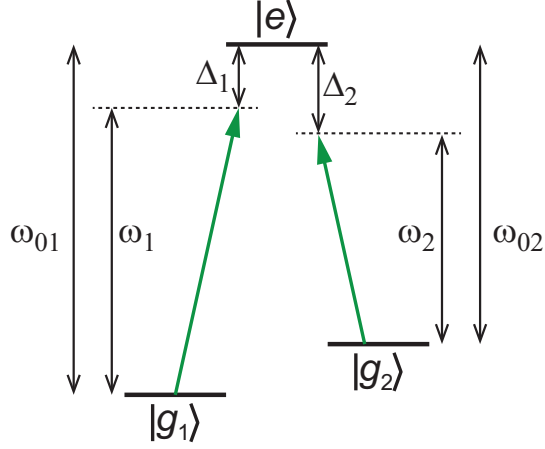
Figure 3.1: Schematic diagram of Raman two-photon transition in the simple Λ-type atom. The two ground states $|g_1\rangle$ and $|g_2\rangle$ are coupled to the excited state $|e\rangle$ by a pair of Raman beams of frequency ω_1 and ω_2.

3.1.1 Two-level approximation

Suppose an atom with three Λ-type energy levels is irradiated by two laser fields of frequencies ω_1 and ω_2 (see Fig. 3.1),

$$\mathcal{E}(\mathbf{r}, t) = \hat{\mathbf{e}}_1 \mathcal{E}_1 \cos\left(\mathbf{k_1} \cdot \mathbf{r} - \omega_1 t\right) + \hat{\mathbf{e}}_2 \mathcal{E}_2 \cos\left(\mathbf{k_1} \cdot \mathbf{r} - \omega_2 t + \Delta\phi\right), \qquad (3.1)$$

where $\hat{\mathbf{e}}_{1,2}$ are the unit polarization vectors of the two fields. Without loss of generality, the global phase is neglected. When the phase difference between the two laser fields $\Delta\phi$ is independent of the pseudospin defined (Here, the Zeeman sublevels of an atom)

The free atomic Hamiltonian can be written as,

$$\hat{H}_A = \frac{p^2}{2m} - \hbar\omega_{01}|g_1\rangle\langle g_1| - \hbar\omega_{02}|g_2\rangle\langle g_2|, \qquad (3.2)$$

where the excited energy is taken as the energy reference. In the frame rotating with $|g_j\rangle \to |g_j\rangle e^{-i\omega_j t}$ $(j = 1, 2)$ and $|e\rangle \to |e\rangle$,

$$\hat{H}_{\mathrm{A}} = \frac{p^2}{2m} + \hbar\Delta_1 |g_1\rangle\langle g_1| + \hbar\Delta_2 |g_2\rangle\langle g_2|, \tag{3.3}$$

where $\Delta_j = \omega_j - \omega_{0j}$ $(j = 1, 2)$ are the detuning of each field from the excited state $|e\rangle$. In the dipole approximation, the Hamiltonian describing atom-field interaction becomes $\hat{H}_{AF} = -\hat{\mathbf{d}} \cdot \mathcal{E}$, where $\hat{\mathbf{d}}$ is the dipole operator. In the rotating wave approximation, this can be written as,

$$\begin{aligned}
\hat{H}_{\mathrm{AF}} &= \sum_{j=1,2} -\frac{1}{2}\langle g_j|\hat{\mathbf{e}}_{\mathbf{j}} \cdot \hat{\mathbf{d}}|e\rangle \mathcal{E}_j \left(|g_j\rangle\langle e|e^{-i\mathbf{k_j}\cdot\mathbf{r}} + \mathrm{h.c.}\right) \\
&= \sum_{j=1,2} \frac{\hbar\Omega_j}{2} \left(|g_j\rangle\langle e|e^{-i\mathbf{k_j}\cdot\mathbf{r}} + \mathrm{h.c.}\right).
\end{aligned} \tag{3.4}$$

Here, $\Omega_j = -\frac{1}{2}\langle g_j|\hat{\mathbf{e}}_{\mathbf{j}} \cdot \hat{\mathbf{d}}|e\rangle \mathcal{E}_j/\hbar$ are the singe-photon Rabi frequencies of respective transitions.

Now, the Schrödinger equation for the total Hamiltonian $\hat{H} = \hat{H}_{\mathrm{A}} + \hat{H}_{\mathrm{AF}}$ is used to describe the system. To solve the equations of motions, the ansatz $|\Psi\rangle = \psi_{g_1}|g_1\rangle + \psi_{g_2}|g_2\rangle + \psi_e|e\rangle$ is chosen. For sufficient large excited state detunings $\Delta_j \gg \sqrt{|\Omega_1|^2 + |\Omega_2|^2}, \Gamma$, the population at the excited state $|e\rangle$ is almost unchanged $(\partial_t\psi_e = 0)$. This is called adiabatical elimination of the excited state. Furthermore, for the most of cold atom case, the kinetic term is much less than the excited detuning $p^2/2m \ll \hbar|\Delta|$, which results in,

$$\psi_e = \frac{\Omega_1}{2\Delta}e^{-i\mathbf{k_1}\cdot\mathbf{r}}\psi_{g_1} + \frac{\Omega_2}{2\Delta}e^{-i\mathbf{k_2}\cdot\mathbf{r}}\psi_{g_2}, \tag{3.5}$$

where $\Delta = (\Delta_1 + \Delta_2)/2$ exploiting the two detunings are nearly equal. The Eq. (3.5) results in the effective Raman Hamiltonian,

$$\hat{H}_{\mathrm{R}} = \frac{p^2}{2m} + \hbar(\Delta_1 + \xi_1)|g_1\rangle\langle g_1| + \hbar(\Delta_2 + \xi_2)|g_2\rangle\langle g_2| + \frac{\hbar\Omega_{\mathrm{R}}}{2}\left(|g_1\rangle\langle g_2|e^{i(\mathbf{k_2}-\mathbf{k_1})\cdot\mathbf{r}} + \mathrm{h.c.}\right) \tag{3.6}$$

or, in the matrix form,

$$\hat{H}_{\rm R} = \begin{pmatrix} \frac{p^2}{2m} + \hbar\xi_1 & \frac{\hbar\Omega_R}{2}e^{i(\mathbf{k_2}-\mathbf{k_1})\cdot\mathbf{r}} \\ \frac{\hbar\Omega_R^*}{2}e^{-i(\mathbf{k_2}-\mathbf{k_1})\cdot\mathbf{r}} & \frac{p^2}{2m} + \hbar(\xi_2 - \delta_{\rm R}) \end{pmatrix} \tag{3.7}$$

where $\delta_{\rm R} = \Delta_1 - \Delta_2$ is the detuning with respect to the two-photon resonance and ξ_j are the AC Stark (light) shift of each level. Here, $\Omega_{\rm R} = \Omega_1\Omega_2^*/2\Delta$ is the Raman two-photon Rabi frequency.

3.1.2 Dark state description

The above description is approximately correct in the sense that the excited state is adiabatically eliminated. When the detuning from the excited state Δ_j is small, the exact description of the system is done by 3×3 matrix. From now on, the kinetic energy is assumed to be small (similar to above) compared to other energy scales. The starting point is the free-atomic Hamiltonian in the rotating frame is given by Eq. 3.3. One amazing feature of the system emerges from a transformation (change of basis),

$$\begin{aligned} |g_+\rangle &= \frac{1}{\sqrt{\Omega_1^2 + \Omega_2^2}} \left(\Omega_1|g_1\rangle + \Omega_2|g_2\rangle\right) = \cos\theta|g_1\rangle + \sin\theta|g_2\rangle \\ |g_-\rangle &= \frac{1}{\sqrt{\Omega_1^2 + \Omega_2^2}} \left(-\Omega_2|g_1\rangle + \Omega_1|g_2\rangle\right) = \sin\theta|g_1\rangle + \cos\theta|g_2\rangle, \end{aligned} \tag{3.8}$$

which mixes the ground states by a rotation angle $\theta = \tan^{-1}(\Omega_2/\Omega_1)$. Then the free-atomic Hamiltonian becomes,

$$\hat{H}_{\rm A} = \hbar\Delta_+|g_+\rangle\langle g_+| + \hbar\Delta_-|g_-\rangle\langle g_-| + \hbar\Omega_g\left(|g_+\rangle\langle g_-| + |g_-\rangle\langle g_+|\right), \tag{3.9}$$

where the rotated detunings are defined by $\Delta_+ = \Delta_1\cos^2\theta + \Delta_2\sin^2\theta$ and $\Delta_- = \Delta_1\sin^2\theta + \Delta_2\cos^2\theta$, and the new coupling Rabi frequency is given by $\Omega_g = (\Delta_2 - \Delta_1)\sin\theta\cos\theta$. At the Raman resonance $\Delta_1 = \Delta_2 = \Delta$, the coupling

66

between $|g_\pm\rangle$ is absent ($\Omega_g = 0$) and the above Hamiltonian becomes $\hat{H}_A = \hbar\Delta\left(|g_+\rangle\langle g_+| + |g_-\rangle\langle g_-|\right)$. On the other hand, the atom-field Hamiltonian in this basis becomes,

$$\hat{H}_{\mathrm{AF}} = \frac{\hbar\Omega_+}{2}|g_+\rangle\langle e| + \frac{\hbar\Omega_-}{2}|g_-\rangle\langle e| + \mathrm{h.c.}, \tag{3.10}$$

where the new Rabi frequencies are

$$\begin{aligned}
\Omega_+ &= \Omega_1\cos\theta + \Omega_2\sin\theta = \sqrt{\Omega_1^2 + \Omega_2^2} \\
\Omega_- &= -\Omega_1\sin\theta + \Omega_2\cos\theta = 0.
\end{aligned} \tag{3.11}$$

Surprisingly, the coupling between $|g_-\rangle$ and $|e\rangle$ vanishes. Therefore, at Raman resonance, $|g_-\rangle$ is a dark state, which does not scatter any photon from the field. (The other state $|g_+\rangle$ is called bright state.) This is because of the destructive interference between two dipoles in the original basis, acting on the dark state. This effect is called coherent population trapping (CPT), where the population is trapped in the dark state due to the quantum interference.

If one takes the kinetic energy into account, the dark state is described together with the momentum basis. Similar to the discussion in section 3.1, the resonance condition now includes momentum states. This results in velocity-selective coherent population trapping (VSCPT) [104], which is useful for sub-Doppler cooling such as gray molasses [105–107]. In this method, the cold atoms are trapped in the dark state to scatter no light at all, while the hot atoms experience collisional cooling from the photons. Since the linewidth of the dark state is smaller than the original atomic natural linewidth, the VSCPT gives rise to sub-Doppler cooling scheme, which becomes powerful tool for atomic species with low evaporative cooling efficiency (not good collision property) such as bosonic ^{7}Li.

So far, many more applications of CPT effect have been studied. For in-

stance, when one of the two transition fields are stronger than the other, the absorption rate for the weak transition drops to zero. At Raman resonance, the medium (atom) does not see the photons and become "transparent". This effect is called electromagnetic-induced transparency (EIT) [108–113]. In this phenomena, (sub-Doppler) narrow linewidth of absorption spectrum yields the abrupt change in the dispersion relation, which results in the slow group velocity of the photons. The lowest speed of photons has been recorded down to 17 m/s [114], which is surprisingly slower than the speed of a human running. Once, this effect "had been" received a wide attention, because of its applications such as storage unit in the area of quantum information.

Moreover, it is possible to transfer the population from one ground state to another by using stimulated Raman adiabatic passage (STIRAP) [115, 116]. Initially, the atoms begin with the dark state. If one adiabatically changes the dark state composition from one ground state to the another (equivalently, changing θ), the population is transferred. One strong benefit of this method is that the population never interacts with the photon, which helps maintaining the cold degenerate temperature of atomic cloud.

Recently, a dark state optical lattice has been proposed [100, 117] and realized [101] using [171]Yb atoms. When the dark state is a function of spatial parameter, the atoms experience photons only at some selected positions. Taking the advantage of ultranarrow linewidth of the dark state resonance, this allows to manipulate the trapping potential with sub-μm resolution.

3.2 Raman transition and artificial gauge fields

3.2.1 Spin-orbit coupling (SOC)

The Eq. 3.7 describes the atom with Raman beams. In this section, we will see
how this off-diagonal phase term act as an artificial gauge potential. Without
loss of generality, we choose a reference frame $(\mathbf{k_2} - \mathbf{k_1}) \cdot \mathbf{r} = 2k_{\mathrm{R}}x$ for simplicity.
Then the Hamiltonian becomes,

$$\hat{H}_{\mathrm{R}} = \frac{p^2}{2m}\hat{1} + \frac{\hbar\Omega_{\mathrm{R}}}{2}\left[\hat{\sigma}_x\cos(2k_{\mathrm{R}}x) - \hat{\sigma}_y\sin(2k_{\mathrm{R}}x)\right] + \frac{\delta}{2}\hat{\sigma}_z, \qquad (3.12)$$

where the detunings from Raman resonance is redefined as $\delta = \delta_{\mathrm{R}} - (\xi_2 - \xi_1)$. In
the rotating frame $\mathcal{U} = e^{ik_{\mathrm{R}}x\hat{\sigma}_z}$, the complex off-diagonal terms are equivalent
to the momentum shift,

$$\hat{H}_{\mathrm{R}}' = \mathcal{U}^\dagger \hat{H}_{\mathrm{R}} \mathcal{U} = \begin{pmatrix} \frac{(p - \hbar k_{\mathrm{R}})^2}{2m} + \frac{\hbar\delta}{2} & \frac{\hbar\Omega_R}{2} \\ \frac{\hbar\Omega_R^*}{2} & \frac{(p + \hbar k_{\mathrm{R}})^2}{2m} - \frac{\hbar\delta}{2} \end{pmatrix}$$
$$= \frac{(p\hat{1} - \hbar k_{\mathrm{R}}\hat{\sigma}_z)^2}{2m} + \frac{\delta}{2}\hat{\sigma}_z + \frac{\Omega_{\mathrm{R}}}{2}\hat{\sigma}_x, \qquad (3.13)$$

where the momentum along $\hat{y}$ and $\hat{z}$ are ignored. Therefore, the Raman two-
photon transition in two-level approximation gives rise to a constant artificial
vector potential (or gauge field) $q\hat{A} = \hbar k_{\mathrm{R}}\hat{\sigma}_z$. The motion of an neutral atom
under the Raman field mimics that of a charged particle under the vector poten-
tial [21]. This is equivalent to the Peierls substitution in the solid state physics,
where complex tunneling amplitude is later turns out to be the same as ex-
ternal magnetic field (or gauge flux) in the lattice systems. To see why, since
the momentum operator is a derivative, the exponential term which yields itself
after the differentiation gives the phase factor as the synthetic momentum. It
is deeply studied in bosonic ^{87}Rb system by I. Spielman's NIST group that one

can engineer an uniform vector potential [118], a synthetic electric field [119], and a magnetic field [120] implementing the Raman scheme.

One important feature of Eq. 3.13 is the spin-momentum locking [23], where the artificial gauge potentials tie up the spin states and the momentum states. If the two ground states $|g_j\rangle$ ($j = 1, 2$) are regarded as pseudospins, each ground state experiences the artificial gauge potentials with opposite momentum kick. This is called spin-orbit coupling (SOC), which is one significant constituent realizing the topological matter preserving a time-reversal symmetry. In solid state physics, the SOC originates from the relativistic effect of electrons moving inside the potential gradient due to the host crystal. The SOC is expected to establish new class of topological matters even without extreme external fields [121], which is hard to be achieved in the typical lab environments and makes difficult to future application. In real materials, however, the SOC is highly limited in tunability and strength: $\approx 10^4$ m/s, which is much less than the Fermi velocity $\approx 10^6$ m/s. Instead, a cold atom system under suitable Raman transitions can provide a platform to study these effect with exquisite controllability. The Hamiltonian in Eq. 3.13 result in a one-dimensional (1D) equal Rashba-Dresselhaus coupling. The main topic of this dissertation is study of topological phases of cold atoms in the optical lattices implementing variations of the above Raman scheme, as we will see below.

3.2.2 Raman transitions in multi-level atoms

A system of real atom is more complicated than the aforementioned description of simple Λ-type scheme; a real atom possesses multiple excited states as well as many ground hyperfine spins. The strength of Raman transition which coher-

ently couples two spins m_F and m'_F can be calculated by just simply summing over all the possible transitions in the excited states. For instance, in the case of ${}^1S_0 \to {}^3P_1$ transitions ($\lambda = 555.8$ nm) of an ^{173}Yb atom, it is always $\alpha_{JJ'} = 3$ and the three excited manifolds $F' = 7/2, 5/2$ and $3/2$ contributes to the Raman Rabi frequency as,

$$
\begin{aligned}
\Omega_{\mathrm{R}} &= \sum_{F'} \frac{\Omega_1 \Omega_2}{2\Delta_{F'}} \\
&= \frac{3\pi c^2}{2\omega_0^3}\, 3\Gamma \sum_{F'} \left(\frac{C_{F',m_F}(\epsilon) C_{F',m'_F}(\epsilon')}{\Delta_{F'}} \right) \sqrt{I_1 I_2},
\end{aligned}
\tag{3.14}
$$

where the atomic frequency $\omega_0 = 2\pi c/\lambda$ and the natural linewidth Γ is almost constant over the various F'. $C_{F',m_F}(\epsilon)$ is the Clebsch-Gordan coefficient defined in Eq. 1.16, ϵ is the polarization vector, and I_j ($j = 1, 2$) is the intensity of each Raman field. Here, the contributions from the other states (${}^1P_1$, ${}^3P_0$, etc...) are negligible. Depending on the polarization of the Raman beams, the selection rule affords one to choose whether the Raman process flips one (π-σ transition for $\Delta m_F = 1$) or two (σ-σ transition for $\Delta m_F = 2$) units of magnetic quantum number. Amazingly, in typical alkali atoms such as ^{87}Rb, the latter has almost negligible transition probability, which makes hard to realize a periodic Raman structure, while the σ-σ transition in alkaline-earth-like atoms can be easily adopted. We will discuss this feature later.

In the Raman experiment given in this thesis, we implement Raman detuning $\Delta_{F'=7/2} = 1.97$ GHz by using an AOM (Brimrose TEF-1700-200-556) changing the frequency by 1.65 GHz and then using another 80 MHz AOM in double-pass configuration. (See the chapter 2 and Fig. 2.5 for more details) In this detuning, the ratio between Raman coupling strength and off-resonant photon scattering rate gives affordable magnitude [122].

3.2.3 Double resonance of Raman transitions

In this section, momentum-resolved Raman specta of a spin-polarized degenerate Fermi gas of ^{173}Yb atoms are depicted, which are measured in the Raman laser configuration of the conventional SOC scheme. The details of the experiment is well-established in the thesis of my colleague M. Lee [99]. In this experiment, the Raman spectra over a wide range of magnetic fields as well as laser intensities are studied to investigate the interplay of multiple Raman transitions in the SOC scheme. For the fermionic ^{173}Yb, it is possible that two Raman transitions become simultaneously resonant at a certain magnetic field and a doublet structure develops in the spectrum for strong Raman laser intensities. We find that the spectral splitting at the double resonance quantitatively resembles the Autler–Townes doublet effect [123].

In the conventional SOC scheme, since one of the Raman laser beams has both of σ^+ and σ^- polarization components with respect to the quantization axis defined by the magnetic field, the Raman transition from one spin state to another, if any, can be made to impart momentum in either direction along momentum transfering axis $\frac{\mathbf{k}_1 - \mathbf{k}_2}{|\mathbf{k}_1 - \mathbf{k}_2|}$ where $\mathbf{k}_{1,2}$ is the wavevector of the Raman beams. In typical SOC experiments, the system parameters are set to make unwanted transitions energetically unfavorable, but the double resonance observed in this work results from involving both of the possible Raman transitions. When all the Raman transitions are taken into account, the effect of the Raman laser fields is represented by a spatially oscillating effective magnetic field [124]. Our measurement results is consistent with the spinful band structure of the Fermi gas under the effective magnetic field.

Sample preparation

The quantum degenerate sample of ^{173}Yb is generated as described in the section 2.5. For an equal mixture of the six spin components, the total atom number is $N \approx 1.0 \times 10^5$ and the temperature is $T/T_{\mathrm{F}} \approx 0.1$, where T_{F} is the Fermi temperature of the trapped sample. The spin composition of the sample can be manipulated with optical pumping and blowing (applying blast pulse) in the course of the evaporation cooling. For the case of a fully spin-polarized sample in the $m_F = -5/2$ state, $N \approx 1.2 \times 10^5$ and $T/T_{\mathrm{F}} \approx 0.35$. The final trapping frequencies of the crossed dipole trap are $(\omega_r, \omega_z) = 2\pi \times (52, 450)$ Hz.

Experiment

In Fig. 3.2(a), the experimental setup is illustrated. A pair of counter-propagating laser beams are irradiated on the sample in the $\hat{x}$ direction and an external magnetic field B is applied in the $\hat{z}$ direction. The two laser beams are linearly polarized in the $\hat{y}$ and $\hat{z}$ directions, which results in the both of σ^+ and σ^- polarization components and π polarization, respectively. Thus, a two-photon Raman process, e.g., imparting momentum of $+2\hbar k_{\mathrm{R}}\hat{x}$ by absorbing a photon from the one Raman beam and emitting a photon into another occurs to change the spin number by either ± 1, where k_{R} is the wavenumber of the Raman beams [23, 125–127].

 The Raman lasers are blue-detuned by 1.97 GHz from the $|{}^1S_0, F = 5/2\rangle$ to $|{}^3P_1, F' = 7/2\rangle$ transition [Fig. 3.2(b)], which is beneficial to induce spin-dependent transition strengths for the $F = 5/2$ hyperfine spin states [128]. The frequency difference of the two Raman beams is denoted by $\delta\omega$. The two beams are set to have a same power and focused to the sample with $1/e^2$ radii of
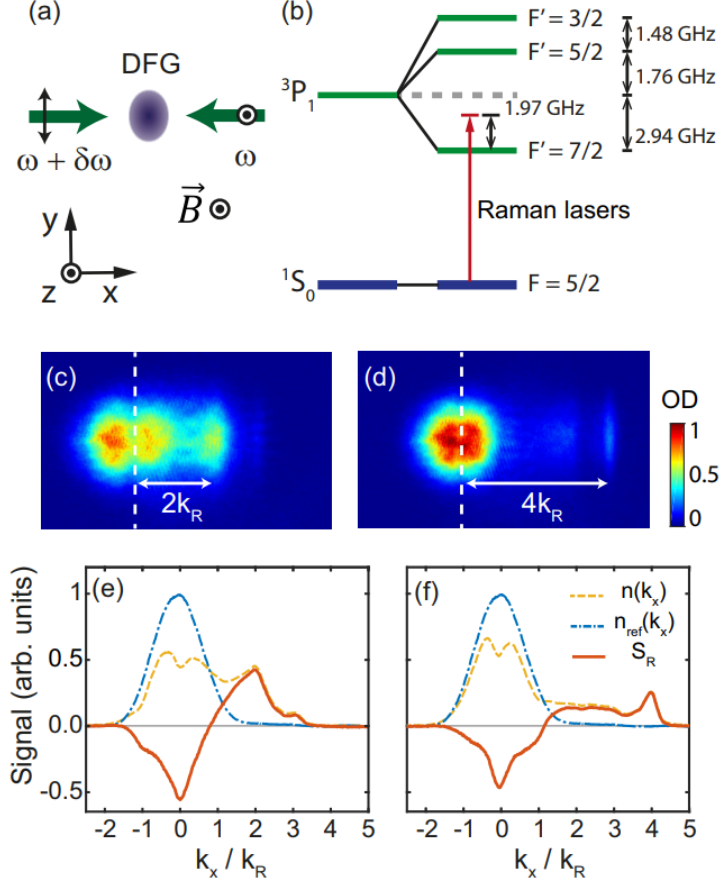
Figure 3.2: Raman spectroscopy of a DFG. (a) Raman coupling setup with a pair of counter-propagating laser beams, whose frequency difference is denoted by $\delta\omega$. (b) Energy diagram of the $^3P_1$ state of ^{173}Yb and the relative detuning of the Raman laser. (c, d) Examplary time-of-flight images of Fermi gases after applying a pulse of the Raman beams for $\delta\omega/2\pi = 14.8$ kHz (c) and 29.6 kHz (d). The vertical dashed lines indicate the center of the unperturbed sample. (e, f) 1D momentum distributions $n(k_x)$ of the samples (yellow) obtained by integrating the images along the y direction. The normalized Raman spectra $S_R(k_x)$ (red) are measured as $S_R(k_x) = [n(k_x) - n_{ref}(k_x)]/n_{ref}(0)$, where $n_{ref}(k_x)$ is the reference distribution (blue) obtained without applying the Raman beam pulse.

$\approx 150~\mu$m, which is much larger than the trapped sample size of 30 μm.

Raman spectroscopy is performed by applying a pulse of the Raman beams and taking a time-of-flight absorption image of the sample. Two exemplary images are shown in Fig. 3.2(c) and 3.2(d), showing that atoms are scattered out from the original cloud with different momenta for different $\delta\omega$. Since the expansion time τ is sufficiently long such that $\omega_r\tau \approx 5$, the time-of-flight image is regarded as the momentum profile of the atoms. The 1D momentum distribution $n(k_x)$ is obtained by integrating the image along the $\hat{y}$ direction [Fig. 3.2(e) and 3.2(f)], where $k_x = mx/(\hbar\tau)$ with m being the atomic mass and x the displacement from the center of mass of an unperturbed sample.

The normalized Raman spectrum is measured as $S_{\mathrm{R}}(k_x) = [n(k_x) - n_{\mathrm{ref}}(k_x)]/n_{\mathrm{ref}}(0)$, where n_{ref} is the reference distribution obtained without applying the Raman beams. Therefore, Raman transition appears as a pair of dip and peak, which correspond to the initial and final momenta of the transition, respectively. The spectral peaks and dips exhibit slightly asymmetric shapes, which is due to elastic collisions of atoms during the time-of-flight expansion [129]. The Fermi momentum of the sample is $k_F/k_{\mathrm{R}} \approx 1.2$ in units of the recoil momentum.

Raman Rabi oscillations

The atomic state in an ideal Fermi gas is specified by wavenumber k and spin number m_F. For a Raman transition from $|k_i, m_i\rangle$ to $|k_f = k_i + 2rk_{\mathrm{R}}, m_f = m_i + \Delta m_F\rangle$, which changes the momentum by $2r\hbar k_{\mathrm{R}}$ and the spin number by Δm_F, the energy conservation requires $E(|k_f, m_f\rangle) - E(|k_i, m_i\rangle) = r\hbar\delta\omega$, which

gives the resonance condition for the initial wavenumber k_i as

$$k_i = k_{\rm R}\left[\frac{\hbar\delta\omega}{4E_{\rm R}} - \frac{\Delta m_F}{r}\frac{B}{4B_{\rm R}} - \frac{1}{r}\frac{\Delta E_S}{4E_{\rm R}} - r\right], \tag{3.15}$$

where $E_{\rm R} = (\hbar k_{\rm R})^2/2m = h \times 3.7$ kHz is the atomic recoil energy, B is the external magnetic field, $B_{\rm R} = E_{\rm R}/(g_F\mu_B) = 17.9$ G, $\Delta E_S = E_S(m_f) - E_S(m_i)$ and E_S denotes the spin-dependent AC Stark shift induced by the Raman lasers. The quadractic Zeeman effect and the atomic interactions are negligible in our experimental conditions.

Firstly, the resonance condition of Eq. 3.15 is investigated by measuring its dependence on various experimental parameters. Fig. 3.3(a) shows a $\Delta m_F = 0$ Raman (Bragg) spectrum as a function of Raman pulse duration for $\delta\omega = 4E_{\rm R}/\hbar$ at $B = 16.6$ G on the spin-polarized samples. Both of the Raman beams were set pi polarization. Momentum-dependent Rabi oscillations are clearly observed and the Rabi frequency is found to be well described with a form of $\Omega(k) = \sqrt{\Omega_0^2 + (\hbar k_{\rm R}k/m)^2}$ with $\Omega_0 \approx 2\pi \times 7$ kHz. The decoherence time is measured to be ≈ 1 ms, which seems to be understandable with the characteristic time scale for momentum dephasing in the trap, $\pi/(2\omega_r) \approx 5$ ms.

Figure 3.3(b) displays a spectrum of the equal mixture sample in the plane of wavenumber k and frequency difference $\delta\omega$ for $B = 0$ G. The $r = 1$ and $r = 2$ transitions are identified in the spectrum with their spectral slope of $\frac{dk}{d\delta\omega} = \frac{\hbar k_{\rm R}}{4E_{\rm R}}$ and different offsets as predicted by Eq. 3.15. The $(k, \delta\omega) \leftrightarrow (-k, -\delta\omega)$ symmetry of the spectrum indicates that the differential AC Stark shift is negligible in the measurement.

Figure 3.3(c) shows the Raman spectrum of the $m_F = -5/2$ spin-polarized sample over a range of magnetic fields from $B = 100$ G to 195 G for $\delta\omega = 13.4E_{\rm R}/\hbar$. In the spectral plane of k and B, the Raman transition with $(r, \Delta m_F) =$
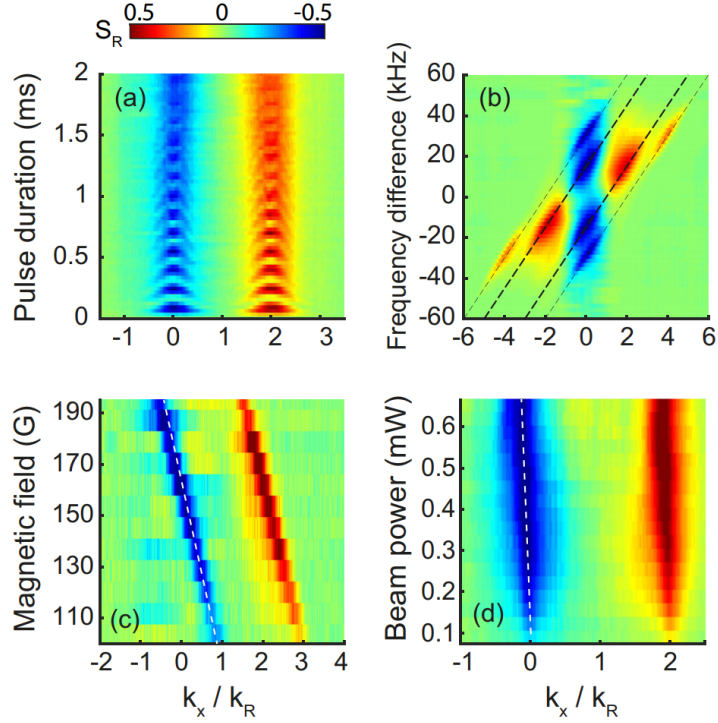
Figure 3.3: Raman spectra measured with scanning various experimental parameters including Raman beam pulse duration t, frequency difference $\delta\omega$, magnetic field B, and Raman beam power P: (a) $\delta\omega = 4E_{\mathrm{R}}/\hbar$, $B = 16.6$ G, $P = 0.47$ mW; (b) $t = 2$ ms, $B = 0$ G, $P = 1.1$ mW; (c) $t = 2$ ms, $\delta\omega = 13.4E_{\mathrm{R}}/\hbar$, $P = 0.21$ mW; (d) $t = 2$ ms, $\delta\omega = 13.4E_{\mathrm{R}}/\hbar$, $B = 133$ G (see the text for details of the sample condition and the polarization configuration of the Raman beams). The dashed lines in (b) indicate $k = k_{\mathrm{R}}(\frac{\hbar}{4E_{\mathrm{R}}}\delta\omega - n)$ for $n = -2, -1, 1,$ and 2, and those in (c) and (d) are guides for the eyes having slopes of $\frac{dk}{dB} = -\frac{k_{\mathrm{R}}}{4B_{\mathrm{R}}}$ and $\frac{dk}{dP} = -0.3k_{\mathrm{R}}/$mW.

$(1, 1)$ appears as a line having the slope of $\frac{dk}{dB} = -\frac{k_R}{4B_R}$ as expected from Eq. 3.15. A linear spectral shift is observed with increasing the Raman beam power [Fig. 3.3(d)], which demonstrates the effect of the differential AC Stark shift ΔE_S. In our experiment, $\Delta E_S = E_S(-3/2) - E_S(-5/2) \approx 1.2 E_R$ for 1 mW, which is in a good agreement with the Raman beam intensities estimated from the Rabi oscillation frequency.

Double resonance

Next, a situation where one spin-momentum state is resonantly coupled to two final states simultaneously is investigated, which we refer to as a double resonance. When the two corresponding Raman processes are characterized with $(r_1, \Delta m_{F1})$ and $(r_2, \Delta m_{F2})$, we see from Eq. 3.15, neglecting the small ΔE_S term, that the double resonance occurs when

$$\frac{B}{4B_R} \frac{\Delta m_{F1}}{r_1} + r_1 = \frac{B}{4B_R} \frac{\Delta m_{F2}}{r_2} + r_2. \tag{3.16}$$

For the primary transition with $(r_1, \Delta m_{F1}) = (1, 1)$, the double resonance condition is satisfied at $B = \frac{4r_2(r_2-1)}{r_2 - \Delta m_{F2}} B_R$.

To observe the double resonance of the $(r, \Delta m_F) = (1, 1)$ and $(2, 0)$ transitions at $B = 4B_R \approx 72$ G, the Raman spectra of the spin-polarized sample in the k-B plane over a range from $B = 0$ G to 140 G [Fig. 3.4] is obtained. Here, the parameters are set $\delta\omega = 8E_R/\hbar$ to have $k_x = 0$ atoms on resonance for the $(2, 0)$ transition, which is insensitive to B for $\Delta m_F = 0$. For low beam intensity, the $(1, 1)$ transition appears with the spectral slope of $-\frac{k_R}{4B_R}$ as observed in Fig. 3.3(c) and the double resonance is indicated by a small signal at $(k, B) = (4k_R, 4B_R)$ [Fig. 3.4(a)], because of enhancement of the second-order Raman transition from $|k = 0, -5/2\rangle$ to $|k = 4k_R, -5/2\rangle$ due to its intermediate

78

state $|k = 2k_R, -3/2\rangle$ being resonant. As the Raman beam power increases, a spectral splitting at the resonance develops [Figs. 3.4(b) and 3.4(c)]. For high Raman beam intensities, the overall spectrum shows the avoided crossing of the spectral lines corresponding to the two $(1,1)$ and $(2,0)$ transitions.

Near the double resonance, the system can be considered as a three-level system consisting of $|0\rangle = |k, -5/2\rangle$, $|1\rangle = |k + 2k_R, -3/2\rangle$ and $|2\rangle = |k + 4k_R, -5/2\rangle$ [Fig. 3.5(a)]. In our case with ^{173}Yb atoms in the $m_F = -5/2$ state, the coupling strength becomes asymmetric, $\Omega_- = 5.3\ \Omega_+$. Since the coupling between $|1\rangle$ and $|2\rangle$ are much stronger than that between $|0\rangle$ and $|1\rangle$, the observed spectral splitting with increasing Raman beam intensity can be described as an Autler–Townes doublet [123]: two dressed states $|\alpha\rangle$ and $|\beta\rangle$ are formed with $|1\rangle$ and $|2\rangle$ under the strong coupling and their energy level splitting is probed via Raman transitions from the initial $|0\rangle$ state. In the rotating wave approximation, the energy levels of the two dressed states are given by $E_{\alpha,\beta} = \frac{1}{2}[E_1 + E_2 - 3\hbar\delta\omega \pm \sqrt{(E_1 - E_2 + \hbar\delta\omega)^2 + (\hbar\Omega_-)^2}]$, where $E_{1,2} = E(|1,2\rangle)$. The resonant wavenumbers $k_{\alpha,\beta}$ of the initial state $|0\rangle$ are determined from $E(|0\rangle) = E_{\alpha,\beta}$ and for $\delta\omega = 8E_R/\hbar$ and $B = 4B_R$, we obtain $k_{\alpha,\beta} = \pm\frac{k_R}{8\sqrt{2}}\frac{\hbar\Omega_-}{E_R}$. We find our measurement results on the double resonance at $B = 4B_R$ in good quantitative agreement with the estimation. The Ω_- was separately calibrated from the Rabi oscillation data of the $|0, -5/2\rangle \rightarrow |-2k_R, -3/2\rangle$ transition for $\delta\omega = -13.4E_R/\hbar$ at $B = 166$ G.

The Raman spectra in Fig. 3.4 reveal another double resonance at $B = \frac{4}{3}B_R \approx 24$ G, where the $(r, \Delta m_F) = (2,0)$ line crosses the $(r, \Delta m_F) = (1,3)$ line. Although the $(1,3)$ transition is a third-order Raman transition, its spectral strength is observed to be higher than that of the $(2,0)$ transition. In the intermediate region of $B \approx 35$ G, many Raman transitions are involved over the
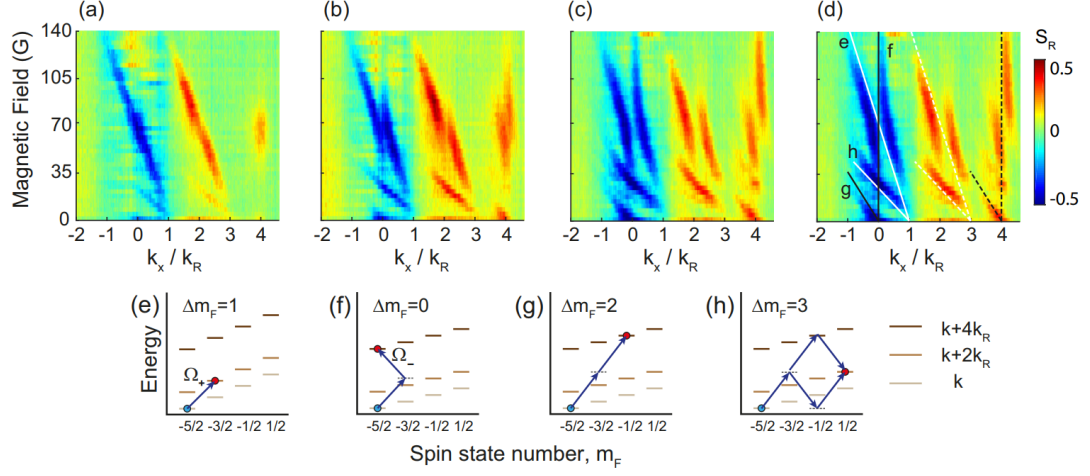
Figure 3.4: Double resonance of Raman transitions. (a–c) Raman spectra of a $m_F = -5/2$ spin-polarized sample as a function of the magnetic field B for $\delta\omega = 8E_\mathrm{R}/\hbar$ and various Raman beam powers (a) $P = 0.13$ mW, (b) 0.21 mW, and (c) 0.36 mW. As the Raman coupling strength increases with higher P, a spectral doublet splitting develops at $B = 4B_\mathrm{R} \approx 72$ G where the $(n, \Delta m_F) = (1, 1)$ and $(2, 0)$ transitions are doubly resonant. The spectrum in (d) is the same of (c) with the guide lines (solid) indicating the resonant momentum positions for various Raman transitions, which are calculated from Eq. 3.15 without including the AC Stark shift. The dashed lines are the corresponding final momentum positions. (e–h) Diagrams of the Raman transitions in the spin number and energy plane.

whole momentum space of the sample and the spectral structure for high Raman laser intensity shows interesting features which cannot be simply explained as crossing and avoided crossing of the spectral lines. It might be necessary to take into account the AC Stark shift effect and a further quantitative analysis of the Raman spectra will be discussed in future work.

Summary and outlook

In this section, the Raman spectra of a spin-polarized degenerate Fermi gas of ^{173}Yb atoms in the conventional SOC scheme and investigated the double
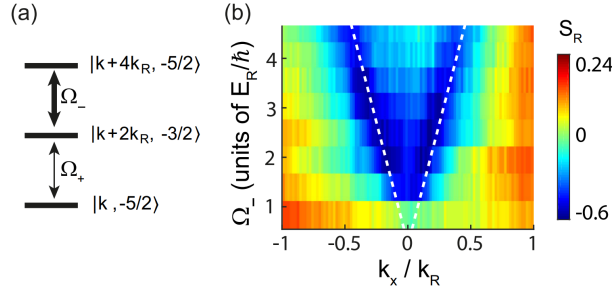
Figure 3.5: Spectral splitting at double resonance. (a) Three atomic states involved in the double resonance at $B = 4B_R$. For a ^{173}Yb atom in the $m_F = -5/2$ state, $\Omega_- = 5.3\ \Omega_+$ and the upper two states are more strongly coupled. (b) Raman spectrum for $\delta\omega = 8E_R/\hbar$ and $B = 4B_R$ as a function of the Raman coupling strength Ω_-. The dashed lines are the theoretical prediction of $k_{\alpha,\beta} = \pm\frac{k_R}{8\sqrt{2}}\frac{\hbar\Omega_-}{E_R}$, which is calculated in the limit of $\Omega_+/\Omega_- \to 0$ (see the text).

resonance of Raman transitions. We observed development of a spectral splitting at the double resonance of the $(r, \Delta m_F) = (1,1)$ and $(2,0)$ transitions and provided its quantiative explanation as the Autler–Townes doublet effect.

In general, when the system has multiple SOC paths in its spin-momentum space, a spinful energy band structure is formed, because of the periodicity imposed by them. In previous experiments [124, 126], the spinful band structures were designed and demonstrated by applying a RF field to the SO-coupled systems under the Raman laser dressing, where the role of the RF field was to open an additional coupling path between two different spin states. The results from this work highlight that the conventional Raman laser dressing scheme provides two ways of SOC and intrinsically produces a spinful band structure without any aid of an additional RF field. After publishing this work, two Raman pathway scheme (called "double–Λ" method) is realized to generate 2D SOC [130–132] in a periodic spinful band structure together with spatially rotating Raman effective field.

81

Chapter 4

Quantum Hall physics with ultracold atoms

Landau theory explains that a phase transition is characterized by the spontaneous symmetry breaking, which brings the system to exhibit a particular order. This phenomenological approach assumes analytic free energy of the system where the ground state changes. For example, ferromagnetic materials below the Curie temperature show magnetization, which implies that a certain spatial rotation symmetry is broken in the spin space. As a classical example, atoms in the liquid have a random distribution, thus having continuous translational symmetry, which is broken when the atoms become a crystal.

One exceptional case of this classification is a topological matter, where no long-range order parameter exists. Rather, the system is characterized by a topological order which displays nontrivial shape in the parameter space. In terms of the physical properties, a matter is topological in the sense that it is insensitive to smooth changes in parameters and microscopic details, unless

it undergoes a topological phase transition. Historically, the era of topological physics has been established since the experimental discovery of integer quantum Hall effect in 1980 by Klitzing [133]. The quantum Hall system depicts the electrons in two-dimensional system (2D electron gas; 2DEG) at low temperature subjected to the strong magnetic field perpendicular to the plane, showing the quantized Hall conductance. The link between this exact quantization and the topology (gauge invariance) had been subsequently found by Laughlin, who had explained the phenomena by his famous *gedanken* experiment of Thouless pump on the charge transport [134, 135].

This chapter describes basics of quantum Hall physics, including very recent researches in the field of quantum gases. To elaborate topological features such as topological invariants and edge currents, the theoretical description of the quantum Hall system in the absence of interaction are also discussed.

4.1 Overview of quantum Hall physics

The electrons traveling inside a periodic potential show discrete energy spectrum called Bloch bands. On the other hand, the electrons under the magnetic field exhibit highly degenerate states known as Landau levels. When both effects come into play, the system produces complex fractal energy spectrum called Hofstadter's butterfly [136]. In this section, the single-particle description on the quantum Hall system is revisited.

4.1.1 Motion under a magnetic field

The Hamiltonian for a charged particle with mass m and charge q under a static magnetic field $\mathbf{B}(\mathbf{r}) = \nabla \times \mathbf{A}(\mathbf{r})$ is (in cgs unit),

$$\hat{H} = \frac{1}{2m}\left(\mathbf{p} - \frac{q}{c}\mathbf{A}(\mathbf{r})\right)^2, \tag{4.1}$$

where $\mathbf{p}$ is the canonical momentum of the particle and $\mathbf{A}(\mathbf{r})$ is the gauge potential. Then, the kinetic velocity is not $\mathbf{p}/m$, but rather $\mathbf{v} = (\mathbf{p} - \frac{q}{c}\mathbf{A}(\mathbf{r}))/m$. Because the $\mathbf{A}(\mathbf{r})$ is the function of spatial location, $[p_i, A_j] = (\hbar/i)\partial A_j/\partial r_i$ and the above two velocities does not commute:

$$[v_i, v_j] = i\frac{q\hbar}{m^2 c}\epsilon_{ijk}B_k. \tag{4.2}$$

Here, ϵ_{ijk} is a Levi-Civita symbol. This leads to the equation of motion for the charged particle,

$$\begin{aligned}
\frac{d\mathbf{v}}{dt} &= \frac{q}{2mc}(\mathbf{v} \times \mathbf{B} - \mathbf{B} \times \mathbf{v}) \\
&= \frac{q}{mc}(\mathbf{v} \times \mathbf{B}) + i\frac{q\hbar}{2m^2 c}\nabla \times \mathbf{B},
\end{aligned} \tag{4.3}$$

where the second equation holds since $[B_j, v_k] = \frac{1}{m}[B_j, p_k] = \frac{i\hbar}{m}\frac{\partial B_j}{\partial r_k}$. In Eq. 4.3, the last term vanishes if magnetic field is uniform, $\nabla \times \mathbf{B}(\mathbf{r}) = 0$, which is identical to the classical equation of motion for the charged particle under the magnetic field (Lorentz force law $\mathbf{F} = q\mathbf{v} \times \mathbf{B}$). This can be understood by the commutation relation between two velocities (Eq. 4.2) become trivial as in the classical case.

Now, the Hamiltonian becomes quadratic function of velocity, $\hat{H} = \frac{1}{2}m|\mathbf{v}|^2$, which resembles the formula for a harmonic oscillator. Without loss of generality, we fix the magnetic field direction to $\hat{z}$, $\mathbf{B} = (0, 0, B)$ as a quantization axis. Then, the $v_z = p_z/m$ is now the constant of motion (symmetric along $\hat{z}$) and

84
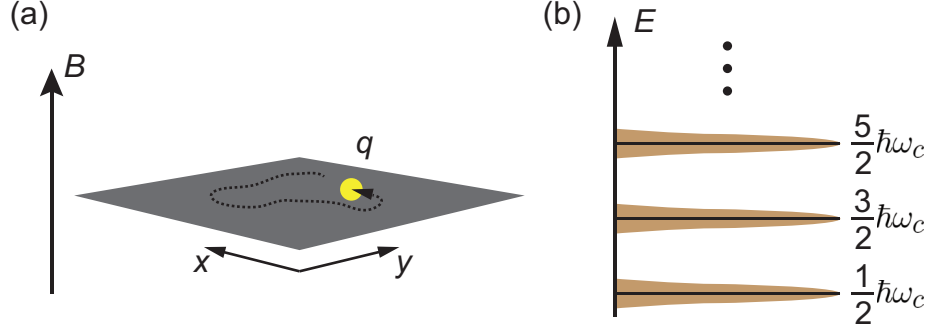
Figure 4.1: Schematic diagram for Landau levels. (a) A charged, quantum particle confined in 2D subjected to the strong magnetic field perpendicular to the plane of motion has a Hamiltonian similar to that of a harmonic oscillator, which yields ladder energy spectrum. These highly degenerate energy eigenstates are called Landau levels. Usually, the degeneracy is slightly broken (brown area) by the impurities.

the system becomes effectively 2D. For the uniform magnetic field, the velocity commutator becomes a c-number, which allows us to define the ladder operators as in the harmonic oscillators,

$$
\begin{aligned}
a &= \sqrt{\frac{m}{2\hbar\omega_c}}(v_x + iv_y) \\
a^\dagger &= \sqrt{\frac{m}{2\hbar\omega_c}}(v_x - iv_y),
\end{aligned}
\tag{4.4}
$$

where $\omega_c = eB/mc$ is the cyclotron frequency. Then the Hamiltonian can be rewritten by,

$$
\hat{H} = \hbar\omega_c\left(a^\dagger a + \frac{1}{2}\right),
\tag{4.5}
$$

and the energy spectrums appear as $E_n = \hbar\omega_c(n + 1/2)$ for $n = 0, 1, 2, \cdots$, which are highly degenerate. These are called *Landau levels*. The equations of motion are simplified to $\dot{v}_x = \omega_c v_y$ and $\dot{v}_y = -\omega_c v_x$, where the solutions are the clockwise circular motion with angular frequency ω_c, like a classical cyclotron:

$$
x(t) = x_0 - \frac{1}{\omega_c}v_y(t), \qquad y(t) = y_0 + \frac{1}{\omega_c}v_x(t).
\tag{4.6}
$$

85

Here, the "center of the cyclotron motion", (x_0, y_0), is a constant of motion, which commute with p_x, p_y, and hence with $a, a^\dagger$, and therefore the Hamiltonian. However, $[x_0, y_0] = -il_B^2$, where $l_B = \sqrt{\hbar/m\omega_c} = \sqrt{\hbar c/eB}$ is the characteristic magnetic length scale, implies that the only one of the coordinates can be diagonalized simultaneously with the energy eigenvalues. (This is equivalent to the Heisenberg's uncertainty principle–if one specifies x_0, uncertainty for y_0 grows.) The radius of the orbit is proportional to the Hamiltonian, as in the classical case,

$$\hat{R}^2 = [x(t) - x_0]^2 + [y(t) - y_0]^2 = \frac{2}{m\omega_c^2}\hat{H}, \tag{4.7}$$

which leads to $(R^2)_n = (2n + 1)l_B^2$.

As in the harmonic oscillator case, the Landau levels are highly degenerate. To specify these states, another quantum number should be given. It is straightforward to see that the angular momentum along $\hat{z}$, L_z, is a constant of motion, by choosing a symmetric Landau gauge, $\mathbf{A} = \frac{1}{2}(\mathbf{B} \times \mathbf{r})$. Despite our discussion does not take lattice potential into account, these degenerate states explain the fundamental reason for a quantized conductance in the integer quantum Hall effect, since the band structure in the deep bulk region can be regarded as Landau levels. When the chemical potential is placed between the energy gap, the system becomes the insulating state and shows plateau of Hall conductance; however, the system turns into the metallic phase if the chemical potential is in the degenerate states. Hence, the Hall conductance displays a step-like function as the external magnetic field increases, which arises due to the growing energy intervals of the Landau levels.

4.1.2 Motion in the square lattice under a magnetic field

Consider a situation where periodic square lattice potential is added. The Hamiltonian of a lattice system is well described by the Hubbard model based on the tight-binding approximation, as long as the system maintains the low temperature regime, where all particles occupy the lowest energy band. In a second-quantized form, the Hubbard Hamiltonian reads,

$$\hat{H} = -t \sum_{m,n} \left(\hat{c}_{m+1,n}^{\dagger} \hat{c}_{m,n} + \hat{c}_{m,n+1}^{\dagger} \hat{c}_{m,n} + \text{h.c.} \right), \tag{4.8}$$

where $\hat{c}_{m,n}^{\dagger}$ and $\hat{c}_{m,n}$ are the creation and annihilation operators for the site (m, n) respectively, and t is the tunneling matrix element between nearest neighboring sites. In presence of the external magnetic field $\mathbf{B} = \nabla \times \mathbf{A}$ (strictly speaking, the vector potential), the above Hamiltonian is modified according to the Peierls substitution,

$$\hat{H} = -t \sum_{m,n} \left(e^{i\phi_{m,n}^{x}} \hat{c}_{m+1,n}^{\dagger} \hat{c}_{m,n} + e^{i\phi_{m,n}^{y}} \hat{c}_{m,n+1}^{\dagger} \hat{c}_{m,n} + \text{h.c.} \right), \tag{4.9}$$

where $\phi_{m,n}^{j} = qA_{m,n}^{j}/\hbar$ denotes the phase accumulated during the hopping along $j = \hat{x}, \hat{y}$, respectively. The Peierls phase defines magnetic flux penetrating the unit plaquette of the square lattice by,

$$\alpha = \frac{\Phi_{m,n}}{2\pi} = \frac{1}{2\pi} \left(\phi_{m,n}^{x} + \phi_{m+1,n}^{y} - \phi_{m,n+1}^{x} - \phi_{m,n}^{y} \right). \tag{4.10}$$

This Peierls phase is equivalent to the Aharanov-Bohm (AB) phase acquired by a charged particle moving along the closed loop in a magnetic field,

$$\Phi_{\text{AB}} = \frac{q}{\hbar} \int_{\mathcal{C}} \mathbf{A} \cdot d\mathbf{r} = 2\pi \frac{\Phi_{\text{B}}}{\Phi_0}, \tag{4.11}$$

where Φ_{B} is the magnetic flux penetrating the area formed by the trajectory $\mathcal{C}$ and $\Phi_0 = h/q$ is the magnetic flux quantum.
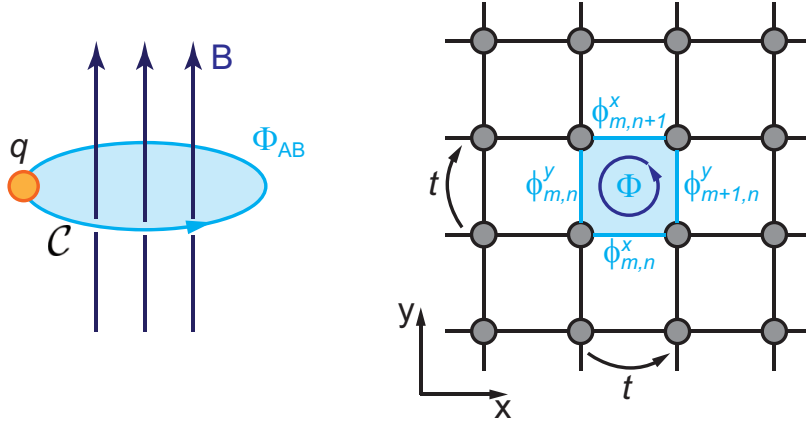
Figure 4.2: Equivalence of Aharonov-Bohm (AB) phase (left) with Peierls phase (right) in lattice systems.

Since the Hamiltonian breeds $U(1)$ gauge symmetry, a suitable gauge selection (nothing but a unitary transformation to different gauge) can simplifies the complex phases in the tunneling elements. For example, by choosing the Landau gauge $\mathbf{A} = (-yB, 0, 0)$, the tunnelings along $\hat{x}$ turns into complex while the tunnelings along $\hat{y}$ become real, and the Hamiltonian becomes [137],

$$\hat{H} = -t \sum_{m,n} \left(e^{-i\Phi_{m,n}n} \hat{c}^{\dagger}_{m+1,n} \hat{c}_{m,n} + \hat{c}^{\dagger}_{m,n+1} \hat{c}_{m,n} + \text{h.c.} \right), \qquad (4.12)$$

which is called famous Harper-Hofstadter (HH) Hamiltonian. (Original version is defined for homogeneous flux $\Phi_{m,n} = \Phi$.) It is no matter where the phase term is attached and the gauge invariance guarantees that choosing any gauge describes the same physical results as long as the transformation is correctly computed. Under the periodic boundary condition, the single-particle energy spectrum of this Hamiltonian shows a fractal structure known as Hofstadter's butterfly, which is a manifestation of two competing length scales (spatial and magnetic length unit) and is described in the section 4.2.

4.2 The Harper-Hofstadter model

A system with HH Hamiltonian can be diagonalized by looking at the symmetry of the Hamiltonian. In absence of the magnetic field, the discrete translational symmetry of the lattice system engenders the Bloch theorem, which implies the momentum space is also periodic in terms of Brillouin zone. When magnetic field is present, the system is no longer invariant under the shift of one lattice unit vector since the vector potential $\mathbf{A}$ is not. Therefore, the spatial lattice translation operators $\hat{T}_j^S$ do not commute with the HH Hamiltonian, $[\hat{T}_j^S, \hat{H}] \neq 0$. On the other hand, the least common multiple of the proper lattice translations in $\hat{x}$ and $\hat{y}$ forms a new unit supercell which represents the new symmetry of the HH Hamiltonian by protecting the invariance under magnetic translations. It is even more complicated when the magnetic flux piercing the lattice unit cell become some irrational number so that any multiples of the new supercell cannot constitute the whole system (integer multiples of 2π). This gives the fractal energy spectrum for incommensurate flux lattices.

To solve the Schrödinger equation for the Hamiltonian in Eq. 4.12, we define magnetic translational operators (MTOs),

$$
\begin{aligned}
\hat{T}_x^M &= \sum_{m,n} \hat{a}_{m+1,n}^\dagger \hat{a}_{m,n} e^{i(\phi_{m,n}^x + \Phi_{m,n} n)} \\
\hat{T}_y^M &= \sum_{m,n} \hat{a}_{m,n+1}^\dagger \hat{a}_{m,n} e^{i(\phi_{m,n}^y - \Phi_{m,n} m)},
\end{aligned}
\tag{4.13}
$$

which incubates the new symmetry of HH Hamiltonian by a commutation relation, $[\hat{T}_j^M, \hat{H}] = 0$ $(j = x, y)$. For homogeneous magnetic field $\Phi_{m,n} = \Phi$, it is satisfied that $e^{-i\Phi} \hat{T}_x^M \hat{T}_y^M = \hat{T}_y^M \hat{T}_x^M$. Consequently, the commutator $[\hat{T}_x^M, \hat{T}_y^M]$ vanishes only if Φ is an integer multiple of 2π. This is equivalent to choose a supercell on the lattice pierced by a magnetic flux equal to an integer multiple of

2π. In fact, the supercell can be chosen in the way that Φ is rational number of 2π by redefining new MTOs by multiples of the old ones. To be more specific, for $k \times l$ unit cell, the commutator becomes $e^{-i\Phi kl}\left(\hat{T}_x^M\right)^k\left(\hat{T}_y^M\right)^l = \left(\hat{T}_y^M\right)^l\left(\hat{T}_x^M\right)^k$. Therefore, one can choose the rational flux $\Phi/(2\pi) = p/q$ ($p,q \in \mathbb{Z}$ coprime integers) such that,

$$\Phi kl = 2\pi\frac{p}{q}kl = 2\pi\nu, \quad \nu \in \mathbb{Z}. \tag{4.14}$$

The smallest possible value making $\left[\left(\hat{T}_x^M\right)^k, \left(\hat{T}_y^M\right)^l\right] = 0$ is $kl = q$ and is called magnetic unit cell. The way of choosing magnetic unit cell may vary, since it is the matter of choosing "gauge" of the system.

In the Landau gauge, one can always construct MTOs with magnetic unit cells of dimension $1a \times qa$. Then, MTOs become mathematically equivalent to the usual discrete translational operators in lattice systems, where one along $\hat{x}$ corresponds to the shift by one lattice constant and the one along $\hat{y}$ corresponds to the translation by q lattice constants. Thus, the wavefunction satisfies the generalized Bloch theorem with the BZ in $\hat{y}$ folded by q times. The wavefunction can be derived by an ansatz,

$$\Psi_{m,n} = e^{ik_x ma}e^{ik_y na}\psi_n, \quad \psi_{n+q} = \psi_n \tag{4.15}$$

where $-\pi/a < k_x < \pi/a$ and $-\pi/(qa) < k_y < \pi/(qa)$. Plugging the ansatz into the Schrödinger equation leads to

$$E\psi_n = -t\left[2\cos\left(k_x a - \Phi n\right)\psi_n + e^{ik_y a}\psi_{n+1} + e^{-ik_y a}\psi_{n-1}\right]. \tag{4.16}$$

This is known as Harper equation which can be solved numerically. In presence of the rational flux $\Phi/(2\pi) = p/q$, the band splits into q subbands, which results in the famous self-similar fractal structure called Hofstadter's butterfly in the single-particle energy spectrum (Fig. 4.3).
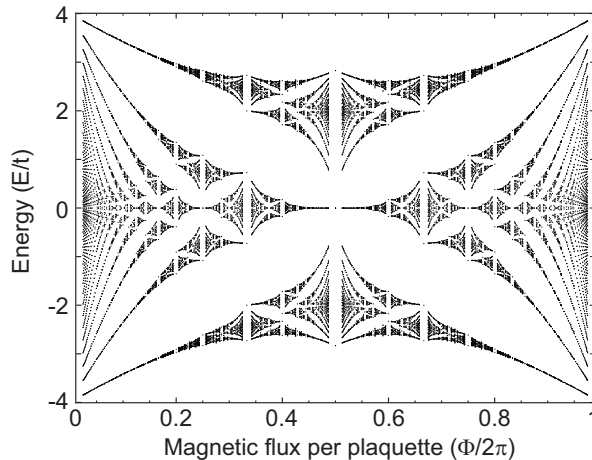
Figure 4.3: Hofstadter's butterfly in a square lattice with a periodic boundary condition. The energy spectrum shows a fractal structure depending on the magnetic flux exerted on the unit plaquette. Here, the spectrum is estimated up to $q = 40$.

Recently, the fractal energy spectrum is observed by implementing two graphene sheets slightly misaligned to produce Moiré superlattices [138]. In cold atom systems, the first realization of the HH Hamiltonian has been carried out by M. Aidelsburger and her colleagues [139]. The original idea is based on Ref. [64, 65]. In this scheme, the complex hopping between neighboring sites is achieved by magnetic field gradient which introduces an energy offset along one direction. The resonant hopping between the neighboring sites results in a chiral cyclotron orbits inside the two-dimensional lattices, which is a manifestation of the HH Hamiltonian.

4.3   Topology and Chern class

The connection between the quantum Hall system and the topology arises from the Berry phase associated with the Bloch wavefunctions $|\psi_n(\mathbf{k})\rangle$. When the

Bloch wavefunction travels around a closed loop inside the parameter space (here, $\mathbf{k}$-space; magnetic BZ), it acquires a Berry phase which is gauge-invariant. Mathematically, the Berry phase is a result of failure of parallel transport in the non-Euclidean parameter space, which is due to the intrinsic curvature of the space. After a parallel transport along a closed path, the vector acquires small angle pointing different direction from the original vector. In quantum mechanics (especially for the Bloch wavefunctions), this amount of angle for the state (ket) vector is measured by Berry phase, which can be calculated by,

$$\gamma_n = \oint_{\mathrm{mBZ}} d\mathbf{k} \; \mathcal{A}_n(\mathbf{k}), \tag{4.17}$$

where $\mathcal{A}_n(\mathbf{k}) = i\langle\psi_n(\mathbf{k})|\nabla_{\mathbf{k}}|\psi_n(\mathbf{k})\rangle$ is the Berry connection associated with the system. Obviously, the Berry connection is gauge dependent since its mathematical structure resembles that of a vector potential. Similarly, Berry curvature (flux) can be defined as

$$\begin{aligned}\mathcal{F}_n(\mathbf{k}) &= \nabla_{\mathbf{k}} \times \mathcal{A}_n(\mathbf{k}) \\ &= i\left(\langle\frac{\partial\psi_n(\mathbf{k})}{\partial k_x}|\frac{\partial\psi_n(\mathbf{k})}{\partial k_y}\rangle - \langle\frac{\partial\psi_n(\mathbf{k})}{\partial k_y}|\frac{\partial\psi_n(\mathbf{k})}{\partial k_x}\rangle\right),\end{aligned} \tag{4.18}$$

which again gives $\gamma_n = \int_{\mathrm{mBZ}} d\mathbf{S} \cdot \mathcal{F}_n(\mathbf{k})$ via Stokes' theorem. (For instance, the 1D version of the Berry phase in the crystalline solids are called Zak phase.) These geometric properties of given parameter space is closely related with the topological nature via Chern theorem, which is a generalization of Gauss-Bonnet theorem in Riemann geometry. In Gauss-Bonnet theorem, summation of the local curvatures generates a topological invariant, which counts the genus of the system. Likewise, the total integral of Berry curvature in the mBZ is known as the Chern number (it is just simply $\nu_n = \gamma_n/2\pi$) which characterizes the topological class of the n-th band. The Chern number should be an integer,
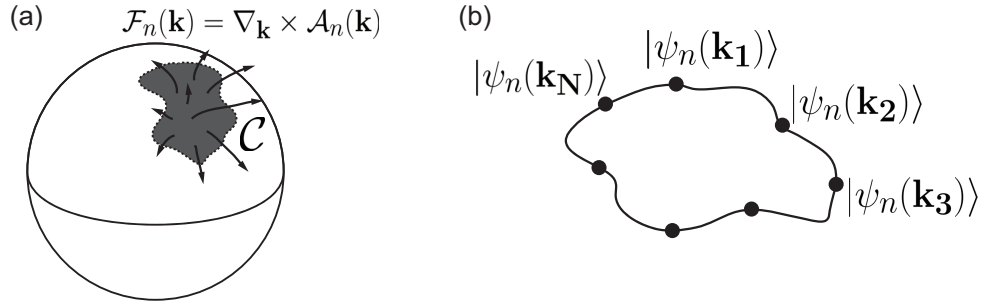
Figure 4.4: Schematic diagram for Berry phase and parallel transport of a vector (ket) state. (a) Berry phase (Chern number) is a measure of total amount of Berry flux penetrating the given surface of parameter space enclosed by a closed path $\mathcal{C}$. (b) After the parallel transport, the ket state acquires small holonomy angle corresponding to the Berry phase, depending on the (Berry) curvature of the parameter space.

since it is the phase mismatch between "two" areas encircled with a single closed loop. The closed loop can be regarded as the border of small area enclosed inside, but also as the boundary of the enclosing area outside the loop. The difference between the two integrals must be agreed up to an integer multiple of 2π, which gives the Chern number [135]. The analogy between Riemann geometry, electromagnetism, and Berry phase in quantum mechanics is summarized in Table 4.1.

The mathematical equivalence of Hall conductance and the curvature was first discovered by Thouless-Kohmoto-Nightingale-Nijs (TKNN) [140], who noticed that the topological properties of the bulk energy bands can be expressed in terms of quantized Hall conductance:

$$\sigma_H = \frac{e^2}{h} \sum_n \nu_n. \tag{4.19}$$

The Chern number is topological in the sense that it is invariant under adiabatic deformations in the parameter space. As a consequence, the Hall conductance is

Table 4.1: Mathematical analogy between Riemann (differential) geometry, electromagnetism, and quantum mechanics

Riemann geometry	Electromagnetism	Quantum Mechanics
Gaussian curvature	Magnetic field	Berry curvature
Levi-Civita connection	Vector potential	Berry connection
Holonomy angle	Aharanov-Bohm phase	Geometric (Berry) phase
Genus	Dirac monopole	Chern number

expected to show a plateau until the abrupt change of the system such as closing the band gaps (or equivalently, Fermi level crossing). This is the topological justification of the integer quantum Hall effect.

The above argument has been derived by assuming periodic boundary condition. In presence of the edges, the each energy gap possesses one edge state; If there are q energy bands, $q-1$ edge modes exist. The chiral edge modes become an evidence of topological state emergent in the HH Hamiltonian. The topological character of the bulk states emerges in the edge states. This is known as *bulk-edge correspondence*.

4.4   Synthetic dimension and chiral edge states

What is a *dimension*? Connectivity. Mathematically, the dimension is the number of coordinates required to specify a point in the space. For a lattice structure under such space is defined by the connectivity between these points, reflecting its dimensional character. For example, a system where the sites are connected by two other sites composes an 1D chain; if the sites are connected by four other sites in a cross-shape, the system composes a 2D square lattice. By extending this concept, any hyperdimensional structure can be also generated by elaborately connecting the sites [141], although our typical world is just 3D. On

the contrary, a structure with complicated connectivity can be regarded as a multi-dimensional lattice. In this part, cold atom systems offer a highly-tunable platform to realize these complicated synthetic lattice structure by connecting different lattice sites with arbitrary complexity.

Recent advances in cold atoms allow one to investigate HH Hamiltonian without use of 2D lattice systems [142]. Instead, any internal or external degrees of freedom of an atom serves as a synthetic dimension, which can be connected arbitrarily each other by photons or oscillating RF fields. In particular, a typical way to achieve synthetic lattice is to implement hyperfine spin states of a neutral atom as a synthetic dimensional sites, which is linked by two-photon Raman transitions. Depending on the phase imprinted on the atoms by Raman photons, the artificial vector potential can be generated in the synthetic lattice, since the tunneling amplitude along the synthetic lattice sites becomes complex as it contains the phase difference between the two photons. In light of this, the spinful atoms in the 1D lattice is equivalent to the spinless atoms in synthetic 2D lattice. The system composes one spatial lattice with "real (original)" and "real ($\in \mathbb{R}$)" tunneling amplitude, and another synthetic dimensional sites along spin direction with complex tunneling strength. In 2015, Florence and NIST group successfully observed chiral edge current in the open boundary Hall ribbon with three synthetic lattice sites [128, 143]. Despite the bulk region contains only the single line of lattice sites, *bulk-edge correspondence* well reflects the topological nature of the synthetic Hall system. In the next chapter, we will see how the dynamics and the topological property of a synthetic Hall system change when the boundary is modified.

Chapter 5

Synthetic Hall tube of Neutral Fermions

This chapter describes realization of a synthetic Hall tube with a periodic boundary condition along synthetic lattice sites. As one of the inter-leg coupling strength varies, a topologically nontrivial Hall tube undergoes a topological phase transition to a trivial open-boundary Hall strip. The result is published in the following paper.

- J. H. Han, J. H. Kang, and Y. Shin, *"Band Gap Closing in a Synthetic Hall Tube of Neutral Fermions,"* arXiv:1809.00444 [cond-mat.quant-gas] (2018).

5.1 Introduction

Over the past decade, a great effort has been devoted to design and to generate artificial gauge potentials for neutral atoms, providing an interesting opportu-

nity for exploring topologically nontrivial states of matter [22]. One of the major triumphs is the realization of the Harper-Hofstadter (HH) Hamiltonian, which is the essential model for quantum Hall physics, described in the chapter 4. The HH Hamiltonian has been demonstrated in two-dimensional (2D) optical lattice systems, using laser-assisted tunneling [21, 23, 139, 144]. In these systems, the lattice sites are distinguished in the energy-selective manner by applying linear potential gradients (for example, magnetic field gradients) and a Raman two-photon transition between the two sites establishes nontrivial site-dependent phase on the wavefunction of atoms. This straightforward method successfully observed chirality and topological (Chern) number [145–147], despite of complicated ingredients required.

On the other hand, another approach called "synthetic dimension frame" is adopted for simple experimental setup [141,142]. In this framework, the any internal or external degrees of freedom of atoms can be viewed as synthetic lattice sites orthogonal to the real lattice dimension. Recently, the ladder systems with the HH Hamiltonian, dubbed Hall ribbons, has been realized in the synthetic dimension framework. In this framework, the hopping along the virtual dimension is provided by Raman two-photon transitions between the states such as hyperfine spins [128, 143]. The framework is further extended with the other degrees of freedom of atoms such as clock states [148], momentum states [149–151], and lattice orbitals [152].

The key advantage of using synthetic lattice dimensions is versatile boundary manipulation. The edges along the synthetic dimension are sharply defined and individually detected with state-sensitive imaging, which allows experimental investigation of various phenomena such as chiral edge currents [128, 143], topological solitons at interfaces [149], and magnetic reflection [150, 151]. Fur-

thermore, nontrivial lattice geometries can be created in synthetic dimensions, which are hardly achievable with conventional optical lattices but may give rise to novel topological states [153,154]. A remarkable example is a ladder geometry with a periodic boundary condition (PBC), which can be realized by cyclically connecting the synthetic lattice sites. It is under a PBC that a Hall lattice system exhibits a *true* fractal structure of the single-particle energy spectrum, called Hofstadter's butterfly [136]. Additionally, Laughlin's pump, which is an ideal manifestation of quantized Hall conductivity and corresponding Chern number, has been proposed for a torus geometry [134, 155, 156]. Moreover, it is expected to observe emergent symmetry-protected topological states in the system under PBCs, which does not fit in either two-(2D) or one-dimensional (1D) theory [154].

In the following, the experimental realization of a synthetic Hall lattice system of a tube geometry with ultracold fermionic atoms is presented. In our scheme, the neutral fermions are confined in a one-dimensional (1D) optical lattice and three hyperfine spin states are employed as a synthetic dimension to form a three-leg tube structure. The cyclic links between the legs are created by spin-momentum couplings via two-photon Raman transitions between the spin states, and a uniform gauge flux $\phi = 2\pi/3$ per side plaquette is generated, thus realizing an HH Hamiltonian with a PBC [136]. Using quench dynamics, we investigate the band structure of the synthetic Hall tube system. When the system deforms from a symmetric tube to an open ladder as one of the inter-leg coupling strengths is decreased, we observe a critical point of band gap closing, which is consistent with a topological phase transition predicted for the Hall tube system. This work opens a new avenue for studies of topological phases with ultracold atoms in unconventional lattice geometries.

5.2 Periodic boundary condition

Sample preparation

Our experiment starts with preparing a degenerate Fermi gas of ^{173}Yb atoms in the $|F = 5/2, m_F = -5/2\rangle$ hyperfine spin state of the $^1S_0$ ground energy level [61]. The typical atom number is $N \approx 1.0 \times 10^4$ and the temperature is $T/T_F \approx 0.3$, where T_F is the Fermi temperature of the trapped sample. The fractional population of the residual atoms in the irrelevant spin states with $m_F \neq -5/2$ is less than 3%. The atoms are adiabatically loaded in a three-dimensional orthorhombic optical lattice potential generated by superposing three orthogonal standing waves with periodicity $d_{x,z} = \lambda_L/2$ and $d_y = \lambda_L/\sqrt{3}$, where $\lambda_L = 532$ nm is the laser wavelength. The lattice potential is exponentially ramped up in 70 ms to the target final lattice depths $(V_x, V_y, V_z) = (5, 20, 20)E_{L,\alpha}$, where $E_{L,\alpha} = h^2/(8md_\alpha^2)$ for $\alpha \in \{x, y, z\}$, h is the Planck constant, and m is the atomic mass. The adiabaticity of the lattice loading is confirmed by the fact that the sample temperature is not significantly altered even after reversing the loading sequence. The lattice depths V_α is calibrated by a modulation spectroscopy method [102]. During the lattice ramp-up, we reduce the dipole trap depth to counteract the increase in the overall trapping potential due to the optical lattice and apply an external magnetic field of 153 G along $\hat{z}$ to lift the spin degeneracy of the $^1S_0$ ground level, resulting in a Zeeman energy splitting of $h \times 31.6$ kHz between adjacent spin states. Then the atoms are held in the final lattice potential for another 20 ms to ensure equilibrium. Because dynamics along the y and z directions is frozen by large lattice depths, our lattice system is effectively 1D with the tunneling amplitude $t_x = 2\pi \times 264$ Hz. At this stage, the sample is in a metallic state with a char-

acteristic filling factor of $N \prod_\alpha \frac{d_\alpha}{\zeta_\alpha} \approx 0.75$, where $\zeta_\alpha = \sqrt{2\hbar t_\alpha/(m\omega_\alpha^2)}$, with the trapping frequencies of $(\omega_x, \omega_y, \omega_z) = 2\pi \times (58, 42, 132)$ Hz [6, 157].

Realization of synthetic Hall tube

The three lowest spin states of $^1\mathrm{S}_0$ state, which we denote $|1\rangle \equiv |m_F = -5/2\rangle$, $|2\rangle \equiv |m_F = -3/2\rangle$, and $|3\rangle \equiv |m_F = -1/2\rangle$, are employed for the three legs of the synthetic tube system. To generate inter-leg couplings, three linearly polarized Raman laser beams $R_{1,2,3}$ are irradiated on the sample [Fig. 5.1(a)], where the wave vectors of the laser beams are given by $\mathbf{k}_{r1} = k_\mathrm{R}(\cos\theta\hat{x} + \sin\theta\hat{y})$ and $\mathbf{k}_{r2} = \mathbf{k}_{r3} = k_\mathrm{R}\hat{x}$, respectively, and the polarization directions are horizontal for $R_{1,3}$ and vertical for R_2 to the xy plane. The laser frequencies of $R_{1,2,3}$ are set to $\omega_1 = \omega$, $\omega_2 = \omega + \delta\omega$, and $\omega_3 = \omega - 2\delta\omega$, respectively, where ω is the laser frequency blue-detuned by 1.97 GHz from the $|^1\mathrm{S}_0, F = 5/2\rangle \to |^3\mathrm{P}_1, F' = 7/2\rangle$ transition line. When $\delta\omega$ is tuned to half of the energy difference between $|1\rangle$ and $|3\rangle$, the three spin states $\{|1\rangle, |2\rangle, |3\rangle\}$ can be resonantly coupled to each other in a cyclic manner by two-photon Raman transitions, as described in Fig. 5.1(b). Thus, a three-leg synthetic tube is constructed with the fermions in the 1D optical lattice [Fig. 5.1(c)].

In the synthetic tube system, the Raman coupling between the spin states $|s\rangle$ and $|s'\rangle$ is described by inter-leg tunneling with complex amplitude $\Omega_{ss'}e^{i\phi j}$, where $\Omega_{ss'}$ is the Rabi frequency of the corresponding two-photon Raman transition and j is the site index for the real lattice. The spatial phase modulations of the tunneling amplitude originate from the momentum transfer $\hbar\Delta\mathbf{k}$ of the two-photon transition, yielding $\phi = (\Delta\mathbf{k} \cdot \hat{x})d_x$ [21]. In our experimental setup, $\Delta\mathbf{k} = \mathbf{k}_{r2,r3} - \mathbf{k}_{r1} = k_\mathrm{R}[(1 - \cos\theta)\hat{x} - \sin\theta\hat{y}]$ for all the cyclic inter-leg couplings and $\phi = 2\pi k_\mathrm{R}d_x(1 - \cos\theta)$ regardless of spin state. When a fermionic particle
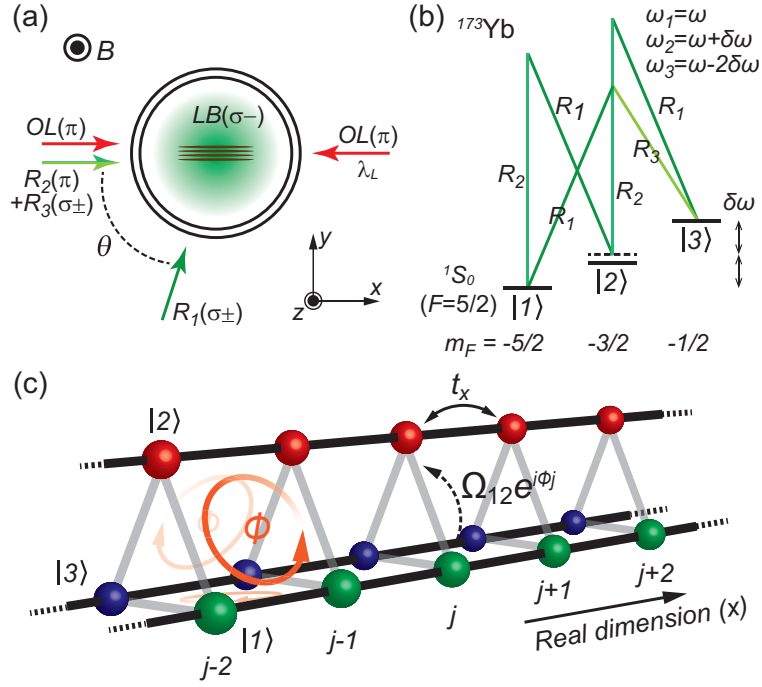
Figure 5.1: Realization of a synthetic three-leg Hall tube with neutral atoms. (a) Schematic of the experimental setup. Fermionic ^{173}Yb atoms are confined in an optical lattice and illuminated by three Raman laser beams $R_{1,2,3}$. A magnetic field B and an additional laser light (LB) are applied along $\hat{z}$ to control the energy levels of the spin states. (b) The three lowest spin states of ^{173}Yb are coupled to each other via two-photon Raman transitions by $R_{1,2,3}$. (c) Synthetic three-leg Hall tube with a uniform gauge flux ϕ on each side plaquette. The three legs are formed by the three spin states of the atoms in the 1D optical lattice (black lines) and the inter-leg tunneling with complex amplitude (gray lines) is provided by the cyclic Raman couplings between the spin states. The flux ϕ is controlled by θ. (see the text for details)
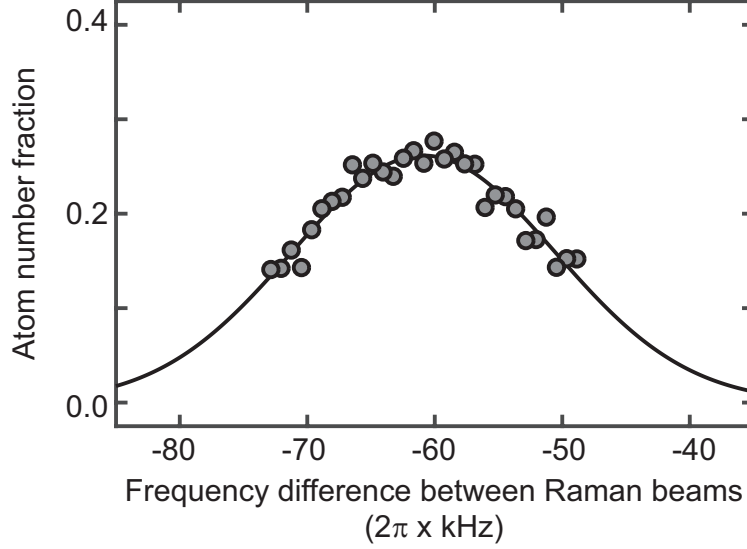
Figure 5.2: Raman spectrum of a spin-polarized sample in $|1\rangle \equiv |m_F = -5/2\rangle$. The outcoupled fraction of the atoms in $|3\rangle \equiv |m_F = -1/2\rangle$ is plotted as a function of the frequency difference of the Raman laser beams (with quadratic free-particle energy subtracted). The Raman beam pulse duration is $t_0 = 50~\mu$s. The solid line indicates a Gaussian curve fit to the data, which results in $2\delta\omega = 2\pi \times 60.8$ kHz.

travels around any side plaquette of the tube, it acquires a uniform net phase of ϕ, thus realizing the HH Hamiltonian in the tube geometry. In this work, the Raman beam angle is fixed to $\theta \approx 72.3°$ to have $\phi = 2\pi/3$, which satisfies the PBC for the synthetic dimension. Because the σ-σ transition ($\Delta m_F = 2$) for the $|1\rangle$-$|3\rangle$ coupling is relatively weak, the intensity ratio of $R_{1,2,3}$ is adjusted to create a symmetric coupling structure. We measure $\Omega_{12} = \Omega_{31} \approx 12.3t_x$. Here, Ω_{23}/Ω_{12} is fixed because the π-σ ($\Delta m_F = 1$) transitions for the $|1\rangle$–$|2\rangle$ and $|2\rangle$–$|3\rangle$ couplings are created by the same pair of Raman beams, and the ratio is nearly unity within 2%.

Note that a system under PBC is hard to be achieved using hyperfine

spins of alkali atoms, because the Raman two-photon σ-σ transition, changing the magnetic quanta by two, is nearly forbidden. Instead, nuclear spins of alkaline-earth-like atoms such as ytterbium (Yb) or strontium (Sr) carry proper σ-σ transition probability of order compared to those of π-σ transitions.

In realizing the three-leg Hall tube, careful control of the energy levels of the spin states is necessary to suppress the optical transitions to the other spin states, $|4\rangle \equiv |m_F = 1/2\rangle$ and $|5\rangle \equiv |m_F = 3/2\rangle$. The energy level ν_s of spin state $|s\rangle$ is determined by the sum of the magnetic Zeeman shift and the total AC Stark shift due to laser radiation. To generate sufficiently large differential AC Stark shifts, we illuminate the sample an additional laser light referred to as a Lift beam (LB) along $\hat{z}$ [158], which is σ^-–polarized and detuned by -70 MHz with respect to the $|^1\mathrm{S}_0, F = 5/2\rangle \rightarrow |^3\mathrm{P}_1, F' = 7/2\rangle$ transition line. The intensity of LB is about 8.5 mW/cm^2. The beam waists of the Lift and Raman beams are 150 μm, much larger than the *in situ* sample radius of 15 μm; thus, the confining effect due to the inhomogeneous intensity distributions of the laser beams is negligible. The lifetime of the atoms with the LB in the optical lattice is measured to be ≈ 250 ms, which is approximately four times shorter than that of the atoms without the LB. As the atoms are illuminated by the Raman laser beams, their lifetime is further reduced to ≈ 20 ms in the open three-leg ladder case and even down to ≈ 6 ms in the three-leg Hall tube case, which makes us impossible to load the atoms in the spinful ground band.

Under the final experimental condition, the energy level differences between the spin states are spectroscopically measured (see Fig. 5.2). The spin-polarized bulk sample is illuminated by a short Raman pulse with a pulse duration $t_0 = 50$ μs, which is resonant for a single leg among the three. Then the fractional population of the atoms transferred to the target spin state is

measured using an optical Stern-Gerlach spin separation method as a function of the frequency difference $\delta\omega_r$ of the two Raman laser beams associated with the transition. Here, the frequency of the other Raman laser beam which is not involved in the target transition is set to be far detuned to prevent Raman transitions to other spin states, while its AC Stark shift effect is maintained. Figure 5.2 shows a typical Raman spectrum for the $|1\rangle \to |3\rangle$ transition, where $|3\rangle \equiv |m_F = -1/2\rangle$. The center frequency $\delta\omega_{r,c}$ is determined by fitting a Gaussian function to the spectrum, and taking into account the kinetic energy contribution, the energy level difference $\nu_3 - \nu_1$ between the two spin states is obtained as $\nu_3 - \nu_1 = \delta\omega_{r,c} - \frac{\hbar}{2m}[2k_R \sin(\theta/2)]^2$. In determining the energy level ν_4 (ν_5) of the spin state $|4\rangle$ ($|5\rangle$), we use a spin-polarized atomic sample in $|3\rangle$. The final experimental condition yields $(\xi_1, \xi_2, \xi_3, \xi_4, \xi_5) \approx (0, -0.2, 0, -2, 1.7)\,\Omega_{12}$, where $\xi_s = (\nu_s - \nu_1) - (s-1)\delta\omega$ is the detuning of $|s\rangle$ from the energy staircase formed by two-photon Raman processes with a step unit of $\delta\omega$ and $\delta\omega = 2\pi \times 30.4$ kHz. The atom loss rate into $|4\rangle$ and $|5\rangle$ is measured to be $\approx 0.01\Omega_{12}$. In the following quench experiment of three-leg Hall tube, the fractional spin populations of $|4\rangle$ and $|5\rangle \equiv |m_F = 3/2\rangle$ are measured to be less than 13% and 7%, respectively, after 1 ms evolution.

Tight-binding model and Bloch Hamiltonian

In a rotating wave approximation, the tight-binding model Hamiltonian for our synthetic three-leg Hall tube system is given by

$$
\begin{aligned}
\hat{H}/\hbar = & \sum_j \sum_{s=1}^{3} \left(-t_x \hat{c}_{j+1,s}^\dagger \hat{c}_{j,s} + \text{h.c.} \right) \\
& + \sum_j \sum_{s=1}^{2} \left(\frac{\Omega_{s,(s+1)}}{2} e^{i\phi j} \hat{c}_{j,s+1}^\dagger \hat{c}_{j,s} + \text{h.c.} \right) \\
& + \sum_j \left(\frac{\Omega_{31}}{2} e^{i\phi j} \hat{c}_{j,1}^\dagger \hat{c}_{j,3} + \text{h.c.} \right) \\
& + \sum_j \sum_{s=1}^{3} \left(\xi_s + \epsilon_j/\hbar \right) \hat{c}_{j,s}^\dagger \hat{c}_{j,s} + \frac{U}{2\hbar} \sum_j \sum_{s \neq s'} \hat{n}_{j,s} \hat{n}_{j,s'},
\end{aligned}
\tag{5.1}
$$

where $\hat{c}_{j,s}$ ($\hat{c}_{j,s}^\dagger$) is the annihilation (creation) operator for a fermion in the Wannier state $|j,s\rangle$ localized at the real lattice site $j = 1, ..., L_x$ with spin $s = 1, 2, 3$. The first term represents tunneling in the real lattice; the second and third terms describe the inter-leg couplings generated by the Raman laser beams, where $\Omega_{ss'}$ is the Rabi frequency of the two-photon Raman transition between the spin states $|s\rangle$ and $|s'\rangle$ and the position-dependent complex phase factor $e^{i\phi j}$ results from the momentum imparted by the Raman transition; the fourth term is the on-site energy in the rotating frame, including the external trapping potential contribution, ϵ_j; and the last term is the on-site interaction energy with number operator $\hat{n}_{j,s} \equiv \hat{c}_{j,s}^\dagger \hat{c}_{j,s}$.

Under a unitary transformation $\hat{\mathcal{U}} \hat{c}_{j,s} \hat{\mathcal{U}}^\dagger = e^{i\phi(s-2)j} \hat{c}_{j,s}'$, the Hamiltonian is

recasted as

$$\hat{H}'/\hbar = \sum_j \sum_{s=1}^{3} \left(-t_x e^{-i\phi(s-2)} \hat{c}'^\dagger_{j+1,s} \hat{c}'_{j,s} + \text{h.c.} \right)$$
$$+ \sum_j \left(\frac{\Omega_{12}}{2} \hat{c}'^\dagger_{j,2} \hat{c}'_{j,1} + \frac{\Omega_{23}}{2} \hat{c}'^\dagger_{j,3} \hat{c}'_{j,2} + \text{h.c.} \right)$$
$$+ \sum_j \left(\frac{\Omega_{31}}{2} e^{i3\phi j} \hat{c}'^\dagger_{j,1} \hat{c}'_{j,3} + \text{h.c.} \right) \tag{5.2}$$
$$+ \sum_j \sum_{s=1}^{3} \xi_s \hat{c}'^\dagger_{j,s} \hat{c}'_{j,s},$$

where the external potential and interaction terms are neglected. When $\phi = 2\pi/3$, the complex phase factor $e^{i3\phi j}$ in the third term becomes unity and j-independent, and via a transformation $\hat{c}'_{q,s} = \frac{1}{\sqrt{L_x}} \sum_j e^{iqj} \hat{c}'_{j,s}$, $\hat{H}'$ can be represented in momentum space by the 3-by-3 Bloch Hamiltonian,

$$\hat{H}_q/\hbar =$$
$$\begin{pmatrix} -2t_x \cos(q - \phi) & \Omega_{12}/2 & \Omega_{31}/2 \\ \Omega_{12}/2 & \xi_2 - 2t_x \cos(q) & \Omega_{23}/2 \\ \Omega_{31}/2 & \Omega_{23}/2 & -2t_x \cos(q + \phi) \end{pmatrix}, \tag{5.3}$$

where q is the quasimomentum of the lattice tube system normalized by d_x^{-1} and $\xi_{1,3} = 0$ are employed. For a symmetric case with $\Omega_{12} = \Omega_{23} = \Omega_{31}$ and $\xi_2 = 0$, it is well known that the Hamiltonian $\hat{H}_q$ for $\phi = 2\pi/3$ embeds a topologically nontrivial state, which is protected by a generalized inversion symmetry [154, 159]. When Ω_{31} is modified for fixed $\Omega_{12} = \Omega_{23}$, the system undergoes topological phase transition to the trivial phase. In our experiment, the protecting symmetry is preserved with spatially uniform $\Omega_{ss'}$ and the topological state survives even $\xi_2 \neq 0$, featuring a nonzero Zak phase $Z = 1$ of its lowest band [160]. The $\hat{H}_q$ has broken time-reversal, particle-hole, and chiral symmetry, which corresponds to

the symmetry class A (unitary) of the Altland-Zirnbauer classification [161,162]. When the lowest band is completely filled, the system represents a topologically insulating state analogous to the integer quantum Hall state [163].

Quench dynamics of synthetic Hall tube

To demonstrate the effect of a gauge flux on plaquettes, the quench dynamics of the synthetic Hall system is investigated. In the quench experiment, the atoms are initially prepared in the leg $|1\rangle$, and then the inter-leg complex hoppings are suddenly allowed by turning on the Raman laser beams. After a variable hold time, the spin composition of the sample is measured by imaging with optical Stern-Gerlach spin separation [41], and separately, the lattice momentum distribution $n(k)$ of the sample is measured using a conventional adiabatic band-mapping technique [157]. Note that in the band-mapping process, the quasimomentum state with q is transformed into a superposition of free-space momentum states of the three spin states in the first Brillouin zone (BZ), where the momentum k_s of spin state $|s\rangle$ is related to q as $k_s d_x = [q + (s-2)\phi]$ modulo 2π and $-k_{\rm L} < k_s \leq k_{\rm L}$ with $k_{\rm L} = \pi/d_x$. The momentum distribution $n_s(k)$ of the atoms in $|s\rangle$ is also measured by spin-selective imaging [Fig. 5.3(b)] [61], for which short pulses of laser light resonant with the $|^1{\rm S}_0, F = 5/2\rangle \rightarrow |^3{\rm P}_1, F' = 7/2\rangle$ transition are applied within the initial 5 ms of the free expansion. The removal process causes inter-spin collisions, which results in atom position blurring in the absorption image [Fig. 5.3(a)].

The measurement results of the time evolution of the quenched synthetic Hall tube system are displayed in Figs. 5.3(c) and 5.3(d). At the early time $t < 100$ μs, when the atoms start transferring to the legs $|2\rangle$ and $|3\rangle$, the average lattice momentum of the sample, $\langle k \rangle = \int_{-k_{\rm L}}^{k_{\rm L}} kn(k)dk / \int_{-k_{\rm L}}^{k_{\rm L}} n(k)dk$,
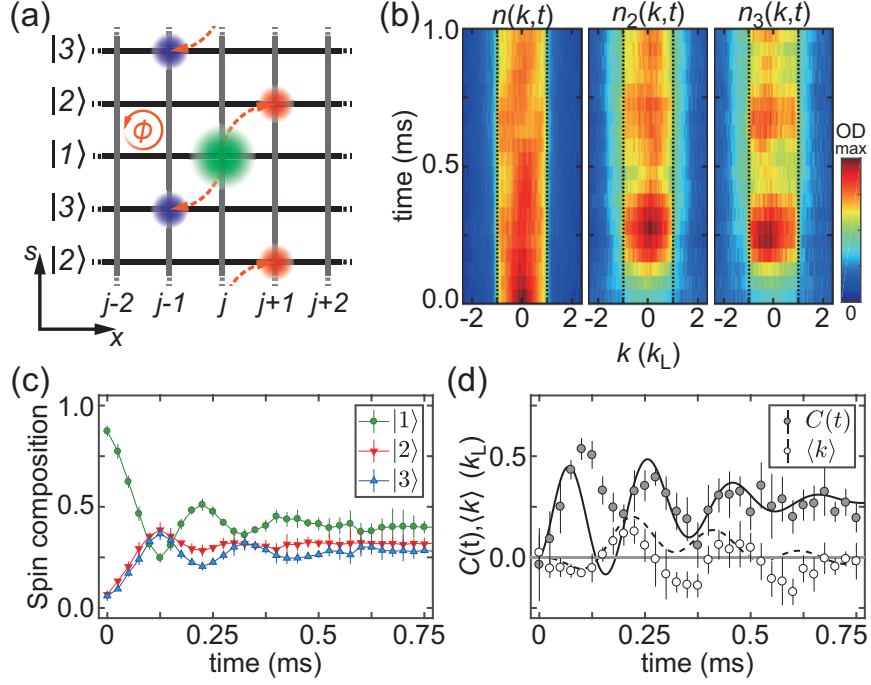
Figure 5.3: Quench dynamics of the three-leg Hall tube for $\phi = 2\pi/3$. (a) Illustration of the atomic motion in the Hall tube. Atoms are initially prepared in the spin-$|1\rangle$ leg and the inter-leg couplings are suddenly activated. (b) Time evolution of the lattice momentum distribution $n(k,t)$ of the sample, $n_2(k,t)$ of the atoms in $|2\rangle$, and $n_3(k,t)$ of the atoms in $|3\rangle$. Time evolution of (c) the fractional spin populations, (d) the average lattice momentum $\langle k \rangle$ of the sample, and the difference $\mathcal{C}(t) = \langle k_2 \rangle - \langle k_3 \rangle$ between the momenta of the two legs $|2\rangle$ and $|3\rangle$. Each data point comprises five measurements of the same experiment, and the error bar is their standard deviation. The solid and dashed lines in (d) show the numerical simulation results for $\mathcal{C}$ and $\langle k \rangle$, respectively.

shows no significant variations; however, the difference between the momenta of the atoms transferred into $|2\rangle$ and $|3\rangle$, $\mathcal{C}(t) = \langle k_2 \rangle - \langle k_3 \rangle$, where $\langle k_s \rangle = \int_{-k_\mathrm{L}}^{k_\mathrm{L}} k n_s(k) dk / \int_{-k_\mathrm{L}}^{k_\mathrm{L}} n_s(k) dk$, increases noticeably. This means that the atoms in the legs $|2\rangle$ and $|3\rangle$ move in positive and negative directions of the real lattice, respectively, which is understandable based on the classical motion of a charged particle moving in the tube in the presence of a magnetic field [Fig. 5.3(a)]. At later times, the spin composition and $\mathcal{C}(t)$ show damped oscillations, which are reasonably accounted for by a numerical simulation for $\hat{H}_q$ including phenomenological damping (refer to the following section). The asymmetry between $|2\rangle$ and $|3\rangle$ and the small oscillations of $\langle k \rangle$ result from nonzero ξ_2.

Numerical simulations

To understand quench dynamics, numerical simulations are performed by solving the Bloch equation,

$$i\hbar \frac{\partial}{\partial t} \begin{pmatrix} c_1(q,t) \\ c_2(q,t) \\ c_3(q,t) \end{pmatrix} = \hat{H}_q \begin{pmatrix} c_1(q,t) \\ c_2(q,t) \\ c_3(q,t) \end{pmatrix}. \qquad (5.4)$$

Here, the atomic density $n_s(k_s, t)$ for spin s and momentum k_s is calculated as $n_s(k_s) = |c_s(q)|^2$, where $k_s d_x = [q + (s-2)\phi]$ modulo 2π and $-k_\mathrm{L} < k_s \leq k_\mathrm{L}$ with $k_\mathrm{L} = \pi/d_x$. The initial conditions for c_s at $t = 0$ are set as $c_1(q,0) = \sqrt{n_1(k_1,0)}$ and $c_2(q,0) = c_3(q,0) = 0$, where $n_1(k_1,0)$ is obtained by averaging the experimentally measured lattice momentum distributions of the initial spin-polarized samples.

Figure 5.5 displays the numerical results of the quench dynamics for the various boundary conditions of the experiment. We observe that spin oscillations show damping in the three-leg Hall tube and three-leg open ladder cases

109
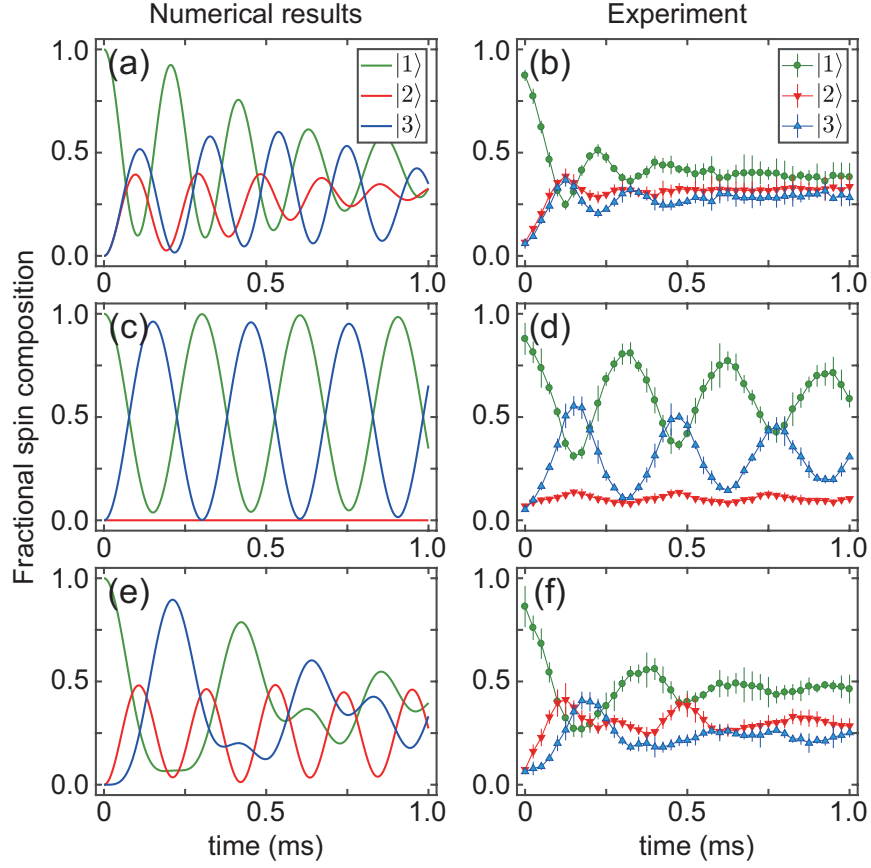
Figure 5.4: Calculated quench evolution of the fractional spin composition for various boundary conditions: (a) three-leg Hall tube, (c) open two-leg ladder, and (e) open three-leg ladder. (b, d, f) Corresponding experimental data shown in Fig. 5.3(c), Fig. 5.6(c) and 5.6(d), respectively.
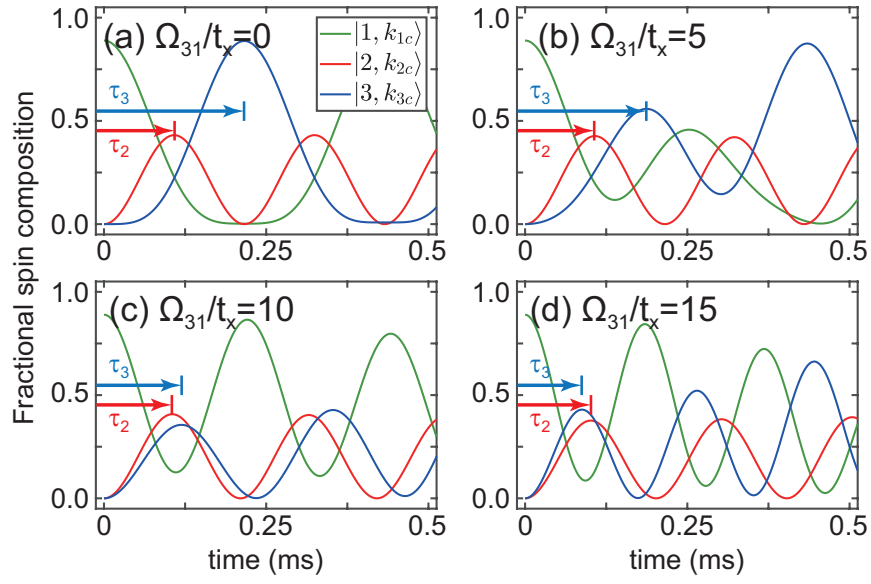
Figure 5.5: Calculated quench evolution of the fractional spin composition at $q_c = \pm\pi$ for various values of Ω_{31}/t_x in the synthetic three-leg Hall tube system. $t_x = 2\pi \times 264$ Hz and $\Omega_{12} = 12.3t_x$ as in the experiment present in Fig. 5.8. τ_s is the time when the fractional population in the spin s state reaches its first maximum.

[Figs. 5.4(a) and 5.4(e)], whereas those in the two-leg open ladder case are not damped [Fig. 5.4(c)]. Here, one of the effective damping originates from ξ_2 being nonzero, which is confirmed in the numerical simulations. In the experiment, we also observe that damping is enhanced in the synthetic Hall tube and open-three leg ladder cases. In the calculations of $\langle k \rangle (t)$ and $\mathcal{C}(t)$ for the three-leg cases in Figs. 5.3(d) and Fig. 5.6(f), we include the damping effect phenomenologically as

$$g_e(t) = \big(g(t) - \bar{g}\big)e^{-t/\tau_d} + \bar{g}, \tag{5.5}$$

where g is $\langle k \rangle$ or $\mathcal{C}$ directly obtained from the numerical simulation and $\bar{g}$ is the mean value determined from the experiment. We find that $\tau_d = 0.15$ ms for the synthetic three-leg Hall tube and $\tau_d = 0.3$ ms for the open three-leg ladder show reasonable agreement with the experimental data.

Figure 5.5 displays the numerical results of the quench dynamics at $q_c = \pm\pi$, i.e., $\{k_{1c}, k_{2c}, k_{3c}\} = \{1/3, \pm 1, -1/3\}k_{\mathrm{L}}$ for various values of Ω_{31}. The time scales of spin oscillations are characterized with τ_s at which spin population in $|s\rangle$ reaches its first maximum. At the critical point $\Omega_{31} = \Omega_-$ of the topological phase transition, $\tau_2 = \tau_3$ is observed, which is a consequence of the associated band gap closing.

5.3   Open boundary condition

The quench evolution of the Hall system is further examined for open ladder geometries [Figs. 5.6(a) and 5.6(b)]. The structure modification is achieved by deactivating two or one of the inter-leg links; by shifting ω_2 (ω_3) by $2\pi \times 400$ (-400) kHz, a two-(three-)leg ladder is formed, respectively. For large detuning, the associated inter-leg couplings are effectively turned off but the AC Stark

shifts due to the Raman beams are nearly unaffected [125, 126]. The time evolutions of the spin composition and the average momentum $\langle k \rangle$ are displayed in Figs. 5.6(c)–5.6(f). In contrast to the Hall tube case, $\langle k \rangle$ shows relatively large oscillations because the atoms are initially prepared at an edge of the ladder. Interestingly, $\langle k \rangle$ changes its sign during the oscillations, and the behavior is well captured by the numerical simulations [Fig. 5.6(e) and 5.6(f)]. In the open three-leg ladder case, we attribute the behavior mainly to the large gauge flux $\phi > \pi/2$ causing atoms to reflect at the BZ boundary. We note that the sign change of $\langle k \rangle$ was not observed in a previous experiment for a smaller gauge flux [128]. In Figs. 5.6(g) and 5.6(h), the semiclassical trajectories of the ladder systems are displayed in the plane of spin and real lattice positions. The open two-leg ladder case shows damped cyclotron motion truncated by the ladder edge, and the three-leg case exhibits bouncing motions due to the Bloch oscillations in the course of cyclotron motion. These observations corroborate the presence of a gauge flux on the side plaquettes of the synthetic tube.

5.4 Topological phase transition

Band gap closing and opening

In Fig. 5.8(a), the phase diagram of the Hall tube system for $\phi = 2\pi/3$ in the plane of Ω_{12} and Ω_{31} is illustrated. The topological phase with $Z = 1$ exists in a region of $\Omega_- < \Omega_{31} < \Omega_+$, where the boundaries are given by,

$$\Omega_\pm = \pm 3t_x - \xi_2 + \sqrt{(3t_x \mp \xi_2)^2 + \Omega_{12}^2}. \quad (\Omega_{12} = \Omega_{23} \text{ and } \xi_{1,3} = 0) \qquad (5.6)$$

Our current system with $\Omega_{31} = \Omega_{12} \approx 12.3t_x$ is located in the topological regime and its transition to a topologically trivial phase with $Z = 0$ can be driven by,

113
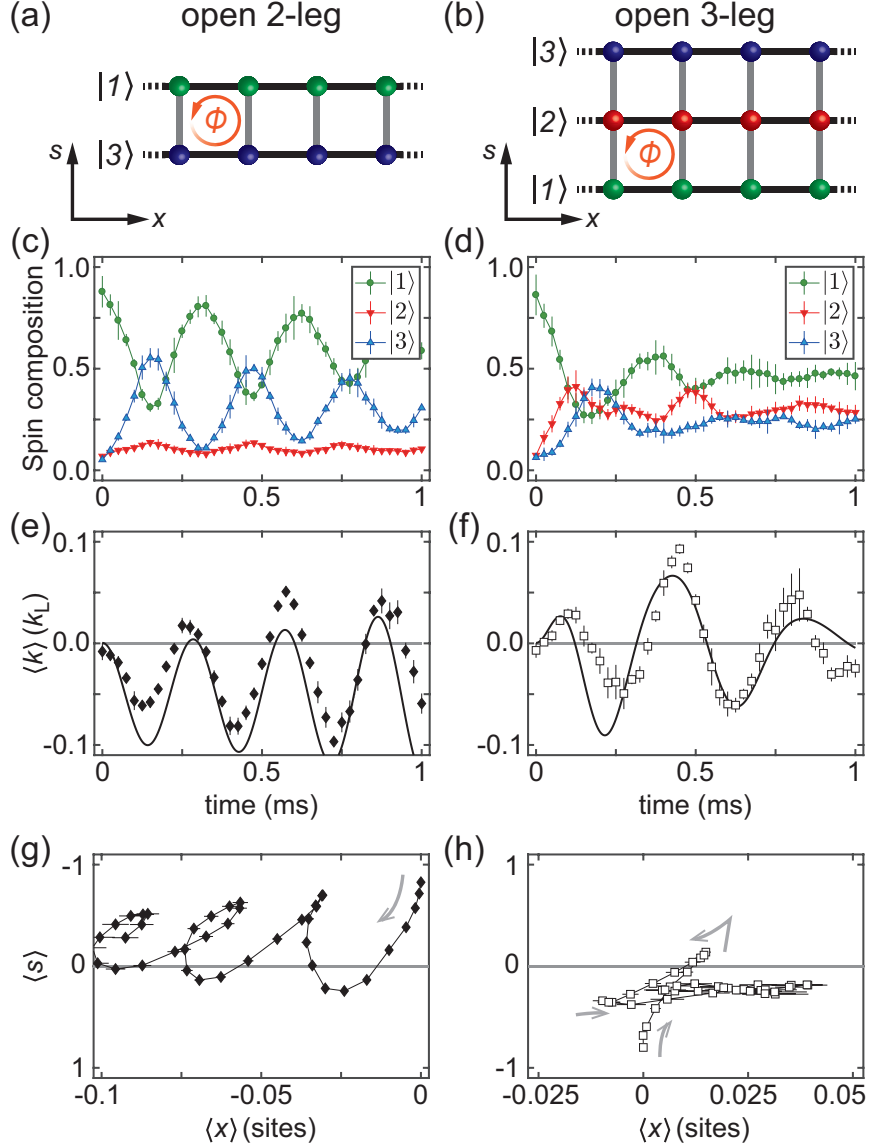
Figure 5.6: Quench dynamics of (a) two-leg and (b) three-leg ladders with open boundaries for $\phi = 2\pi/3$. Time evolution of (c,d) the fraction spin populations and (e,f) the average lattice momentum $\langle k \rangle$. The solid lines display the numerical simulation results for $\langle k \rangle$. Each data point comprises five measurements of the same experiment. (g,h) Trajectories of the ladder systems in the plane of the spin and real lattice positions $\langle s \rangle$ and $\langle x \rangle$. $\langle s \rangle = \tilde{n}_3 - \tilde{n}_1$, where $\tilde{n}_s$ is the fractional population of spin component $|s\rangle$ and $\langle x \rangle$ is calculated from $\langle k \rangle$ using the knowledge of band dispersion [128].

114
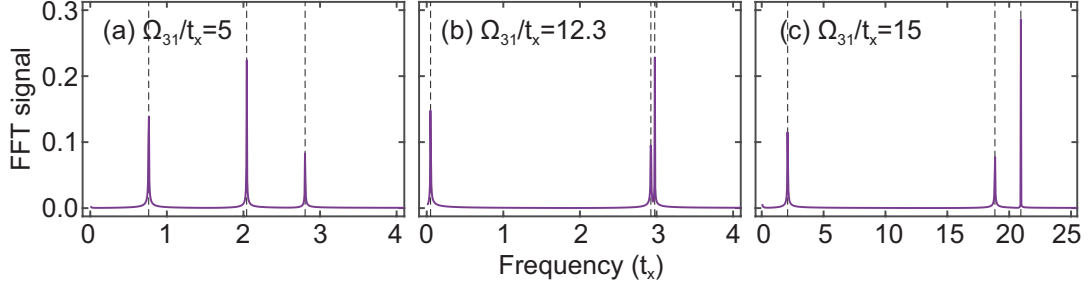
Figure 5.7: Expected Fourier spectrum of the quench dynamics at specific quasi-momentum $q_c = \pm\pi$ for (a) $\Omega_{31} = 5t_x$, (b) $\Omega_{31} = 12.3t_x$, and (c) $\Omega_{31} = 15t_x$. The quench data from numerical simulation for 10 ms (sampling rate of 5 μm) is transformed to show three bands. As the system changes its topology from trivial to nontrivial, the two rightmost peaks should merge and then seperate, which indicates the band gap closing. Conversely, the Fourier spectrum can be implemented to reconstruct the band structure of the system [164].

for example, decreasing Ω_{31} below the critical value of $\Omega_- = 11.6t_x$ [154]. In Fig. 5.8(b), the band dispersions of the Hall tube system are displayed for various Ω_{31}, showing that the topological phase transition at $\Omega_{31} = \Omega_-$ occurs with closing the energy gap between the first and second bands at quasimomentum $q_c = \pm\pi$. On the other hand, the topological transition at $\Omega_{31} = \Omega_+$ shows the gap closing at $q = 0$ [154]. This is because the $\hat{H}_q$ is mirror symmetric along the spin dimension with respect to $|2\rangle$ for $\Omega_{12} = \Omega_{23}$; the quasimomentum for gap closing should be $q = 0$ or $\pm\pi$. According to the bulk-edge correspondence, band gap closing is a generic and necessary feature of the topological phase transition of a symmetry-preserving system [165].

The critical point of band gap closing is probed via momentum-resolving analysis of the quench dynamics. It is possible to reconstruct the band structure using the quench dynamics [164], by measuring all the Fourier component
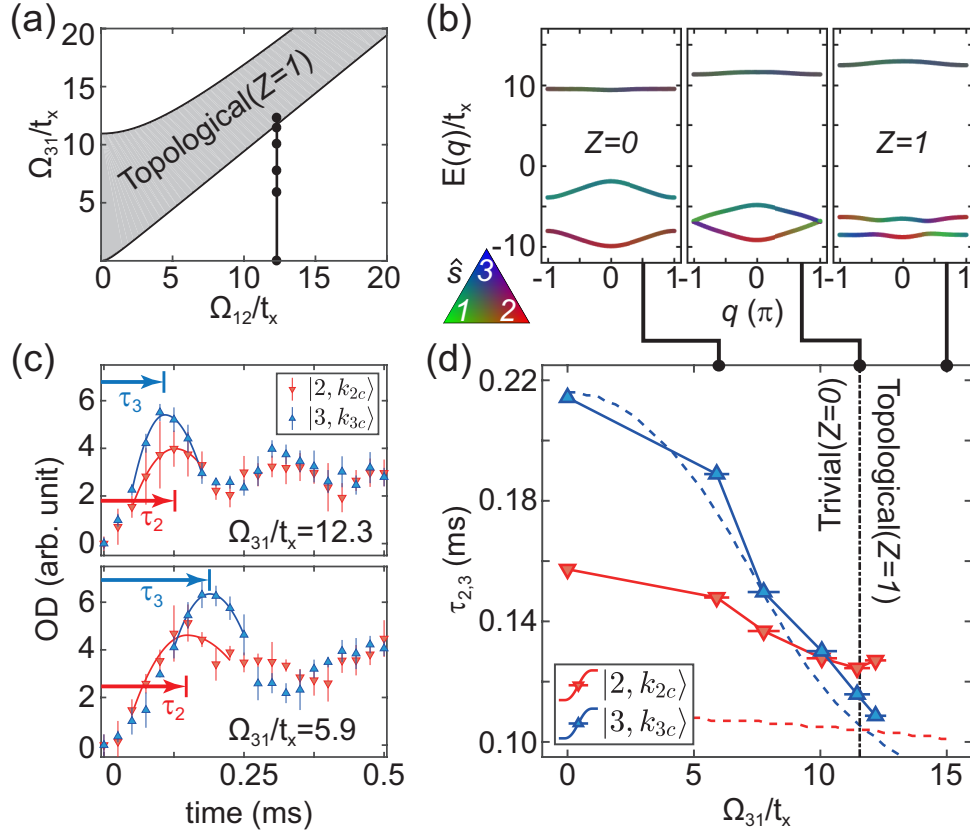
Figure 5.8: Observation of band gap closing in the three-leg Hall tube. (a) Phase diagram of the system. The shaded area indicates a topologically nontrivial phase with a nonzero Zak phase $Z = 1$ of the lowest band. The solid dots indicate the parameter positions explored in the experiment. (b) Band structures calculated for various Ω_{31} with $\Omega_{12} = \Omega_{23} \approx 12.3 t_x$. A topological phase transition occurs together with band gap closing at $q_c = \pm\pi$. (c) Quench evolution of $n_2(k_{2c})$ and $n_3(k_{3c})$, where k_{2c} and k_{3c} are the lattice momenta of $|2\rangle$ and $|3\rangle$, respectively, corresponding to q_c. Each data point is obtained by averaging five measurements and the error bar is their standard deviation. The time τ_2 (τ_3) for the first maximum of $n_2(k_{2c})$ ($n_3(k_{3c})$) is determined by fitting the experimental data to an asymmetric parabola function (solid line). (d) τ_2 and τ_3 as functions of Ω_{31}. The red and blue dashed lines show the numerical results for τ_2 and τ_3, respectively. The crossing of τ_2 and τ_3 reveals the critical point of band gap closing.

116

of each band quasimomentum, which is equivalent to the band energy $E(q)$. Especially, when the band gap closes, the dynamic evolution at critical quasi-momentum $q = q_c$ is governed by a single energy scale that is determined by the energy gap [Fig. 5.7]. Therefore, the gap closing would be characteristically reflected in the quench evolution of the spin composition at q_c. Unfortunately, our quench dynamics show short coherence time (few hundreds of μs) which cannot perform direct Fourier transform. Instead, to obtain largest energy scale (band gap) present in the system, we measure the shortest time scale of the quench dynamics. The momenta of the spin states $|2\rangle$ and $|3\rangle$ corresponding to $q_c = \pm\pi$ are $k_{2c} = -k_\mathrm{L}$ and $k_{3c} = -k_\mathrm{L}/3$, respectively, and we measure the quench evolution of $n_2(k_{2c})$ and $n_3(k_{3c})$ for various $\Omega_{31} \leq \Omega_{12}$ [Fig. 5.8(c)]. When Ω_{31} is decreased by decreasing the intensity of R_3, the resulting reduction of the AC Stark shift is compensated for by applying another off-resonant laser light with the same polarization as R_3. To obtain the characteristic time scales of the spin composition oscillations, we determine the times τ_2 and τ_3 at which $n_2(k_{2c})$ and $n_3(k_{3c})$ reach their first maxima, respectively, by fitting the experimental data to an asymmetric parabolic function,

$$f(t) = \begin{cases} \alpha_1(t - \tau_s)^2 + \beta & \text{for} \ \ t \leq t_s \\ \alpha_2(t - \tau_s)^2 + \beta & \text{for} \ \ t > t_s \end{cases}, \tag{5.7}$$

with four fitting parameters, $\alpha_{1,2}$, β, and τ_s.

Figure 5.8(d) shows the measurement results of the time scales as functions of Ω_{31}. At $\Omega_{31} = \Omega_{12}$, τ_3 is smaller than τ_2 and increases faster than τ_2 as Ω_{31} decreases. The crossing of τ_2 and τ_3 occurs at $\Omega_{31} \approx 10.4 t_x$ in the vicinity of the expected critical point Ω_-. The numerical simulation reproduces the observed crossing behavior of the two time scales and yields $\tau_2 = \tau_3$ at $\Omega_{31} = \Omega_-$, which validates our experimental approach using the time scales of quench dy-

namics to probe band gap closing. The deviation of the measured critical value from the predicted Ω_- is not clearly understood. This might be due to imperfection in the spin-selective imaging, the damping, or the interaction effects in the quench dynamics, which are neglected in our numerical simulations. For our experimental parameters, the on-site interaction energy is estimated to be $U/\hbar \approx 1.7 t_x$.

5.5 Detuned systems

Thus far, synthetic Hall tube system has been studied for assuming all the Raman photons are on resonance. When the three Raman pairs are slightly detuned by δ_i $(i = 1, 2, 3)$, the dynamics slows down significantly. This can be understood by the concept of generalized Rabi frequency for the two-level systems, as $\tilde{\Omega}_i = \sqrt{\Omega_i^2 + \delta_i^2}$. In general, the Hamiltonian can be written as,

$$
\hat{H}_q/\hbar =
$$

$$
\begin{pmatrix}
\xi_1 - 2t_x \cos(q - \phi) & \Omega_{12} e^{-i\delta_1 t}/2 & \Omega_{31} e^{-i\delta_2 t}/2 \\
\Omega_{12} e^{i\delta_1 t}/2 & \xi_2 - 2t_x \cos(q) & \Omega_{23} e^{-i\delta_3 t}/2 \\
\Omega_{31} e^{i\delta_2 t}/2 & \Omega_{23} e^{i\delta_3 t}/2 & \xi_3 - 2t_x \cos(q + \phi)
\end{pmatrix}, \quad (5.8)
$$

where the detunings are present in the off-diagonal terms. Note that the above Hamiltonian has no eigenstate–it is perturbed endlessly by the phase modulation due to the Raman beams. In synthetic dimension description, the Hamiltonian depicts the phase modulated cyclic chain, where the phase is accumulated by $\sum_i \delta_i$ after an atom hops around the single spin loop. It is interesting to study when $\sum_i \delta_i \neq 2\pi n$, which is similar to the Hofstadter's butterfly with incommensurate flux. Further investigation is required to find the physics inside this process.
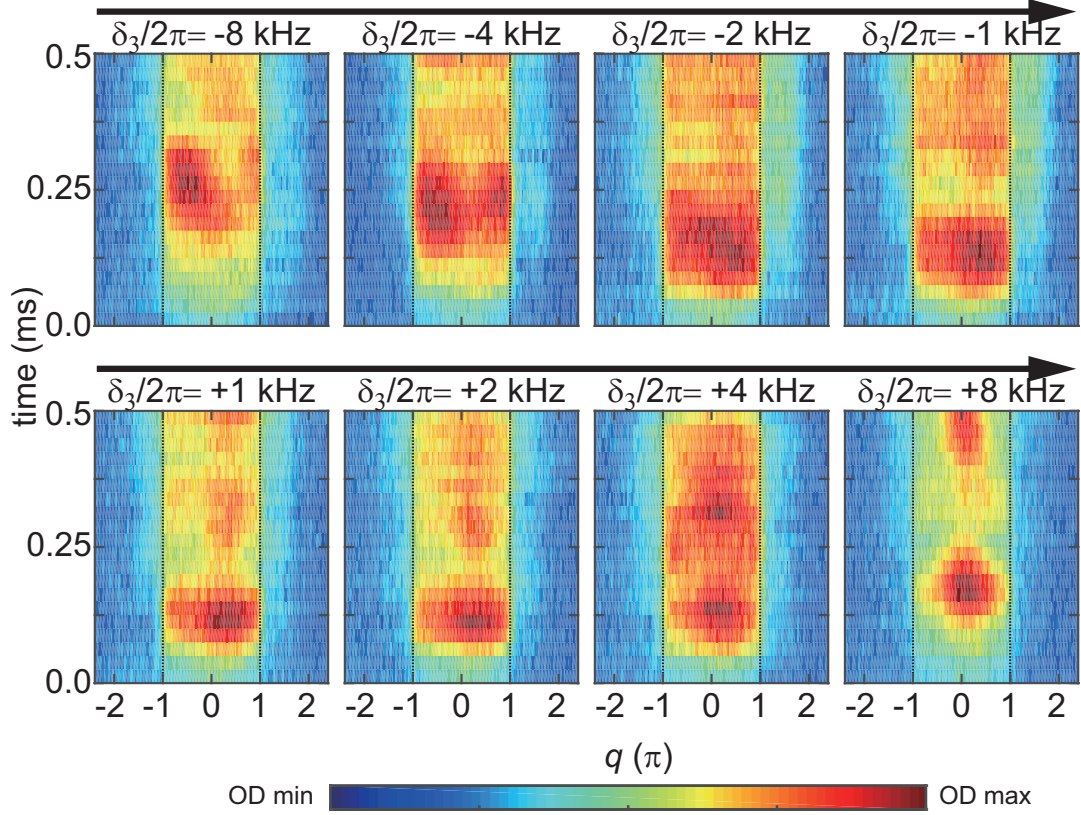
Figure 5.9: Quench dynamics of $|m_F = -1/2\rangle$ for various R_3 detunings at equal Rabi frequencies. The sample is initially prepared in $|m_F = -5/2\rangle$ and the inter-leg couplings are suddenly activated. The momentum space of $|m_F = -1/2\rangle$ is obtained by state-selective imaging. The Raman beams $R_{1,2}$ are on resonance and δ_3 is scanned from $2\pi \times -8$ kHz (top left) to $2\pi \times +8$ kHz (bottom right). As detuning grows, the dynamics gets dragged.

5.6 Zero-momentum Raman spectroscopy

The RF transition is almost impossible in alkaline-earth-like atoms due to the lack of ground state magnetic moment. Instead, when the momentum transfer between the two Raman photons are zero (that is, the angle between the Raman beams is $\theta = 0$), the transition between different spin states become also possible independent of momentum of the original cloud. This can be implemented to realize the "zero-momentum" Raman spectroscopy for alkaline-earth-like atoms as the RF spectroscopy does for the alkali atoms.

The scheme can be easily implemented by using one AOM with two RF sources. we have tested two AOMs in typically used our lab, whether they accept multiple frequencies at the same time. Some AOMs (Intraaction, ATM-801A1) accepted multiple RF frequencies, while the others (AA optics, MT80-B30A1,5-VIS) did not. Moreover, the frequency difference between the two RF sources should be the half of the target frequency. For example, if one plugs 80 MHz and 80.03MHz, the strongest frequency component in the beating signal is 60 kHz, not 30 kHz. It is also worth to mention that higher-order harmonic frequency components were also appeared though they were insufficient in magnitude (below -30 dB) to provoke corresponding transitions. This results from the different characteristic bandwidth of the modulator attached at the device.

Next, the two Raman beams are coupled to the single fiber and share the same beam path. We observed inter-spin Rabi oscillation by suddenly irradiating zero-momentum Raman beams on the spin-polarized sample of $|m_F = -5/2\rangle$ and then measure the spin composition of the cloud using optical Stern-Gerlach method. By setting the frequency difference between the two RF sources be the half of the energy difference between the states $|m_F = -5/2\rangle$ and $|m_F = -1/2\rangle$,

120
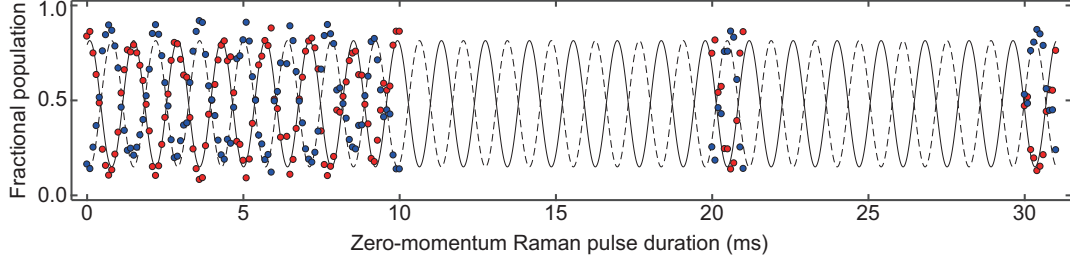
Figure 5.10: Zero-momentum tranfer Raman Rabi oscillations. The fractional population is measured by optical Stern-Gerlach experiment. The initial population at $|m_F = -5/2\rangle$ (red) oscillates back and forth to the state $|m_F = -1/2\rangle$ (blue). In this experiment, both Raman beams are horizontally polarized perpendicular to the magnetic field (≈ 153 G) to induce σ^+-σ^- transition. The bold and dashed lines are experimental fit which results the Rabi frequency of $\Omega_R \approx 2\pi \times 1.4$ kHz.

several cycles of Rabi periods are measured. Surprisngly, the oscillation does not lose its coherence even upto several hundreds of ms [Fig. 5.10], which is enormously large compared to the case of nonzero-momentum Raman transition with independent fiber using ≈ 2 ms [see Fig. 3.3]. We guess that the phase noise between different fibers are the cause. Therefore, the system can be improved by implementing active phase-locked-loop (PLL) for the longer coherence.

In synthetic dimension frame, the zero-momentum Raman transitions can be viewed as trivial hopping along the synthetic dimension. One direct extension to this technique is to realize boundaries with magnetic defects in the synthetic lattices [150]. It is also interesting to investigate various quantum transport properties using the synthetic dimension frame [151, 166–168].

5.7 Conclusions and outlooks

In this chapter, we reviewed the realization of a synthetic three-leg Hall tube with $\phi = 2\pi/3$ and the band gap closing at a critical point of the topological phase transition was demonstrated. In our experimental setup, the gauge flux ϕ can be controlled by θ, and we expect an immediate expansion of this work to study fractal band structures with varying magnetic fluxes from commensurate to incommensurate values. In such commensurate flux $\phi = \pi/3$, for instance, the Bloch Hamiltonian is now 6-by-6 and the three energy bands splits into the six bands. In case of incommensurate flux, the band picture is not applicable and the Hamiltonian can be only described in a sequential form, which is known as famous Harper equation studied in chapter 4. When sufficient coherence time is secured to resolve small energy scales appearing in the band splitting, observing Hofstadter's butterfly is no more a dream. This can be done by stabilizing the Raman beam phase noise due to the fiber.

It is also promising to realize synthetic lattices of unconventional lattice geometries with nontrival boundary conditions. For instance, when every $\Delta m_F = 1, 2$ transitions are coupled, the six spins of ^{173}Yb constitutes a short zig-zag lattice with four unit cells. In fact, a proposal to create a chain of zig-zag lattices using only two spin states and spin-dependent lattices is suggested [169]. A crucial limitation of using hyperfine spins as synthetic dimension is lack of freedom in creating various connections between the legs. Since the only way to disconnect unwanted inter-leg links is the energy mismatch, the system requires an additional gadget (such as LB in our scheme) to achieve proper energy shifts. Placing a gadget is cumbersome, and systematic noise or heating on the atomic sample should be ensued. One solution is to implement other synthetic degrees

such as free momentum states [149–151] and lattice orbitals [152]. In the former case, much more degree of freedom in connectivity is provided at the expense of lattice length. Despite finite size of the lattice (typically 20 sites), many exotic transport behavior has been investigated using the momentum states; however, this scheme cannot be employed to the fermionic systems due to large momentum spread. In the lattice orbitals, three-leg cross-linked Cruetz model has been demonstrated. In Ref. [153], lattice systems with Möbius strip and twisted torus are proposed to observe exotic topological phasese immersed in the geometry. These can be realized by directly implementing both lattices with synthetic dimensions (synthetic+synthetic lattices).

Future directions may include interatomic interactions [170], which are expected to show fractional charge behavior [155], using the recently implemented orbital Feschbach resonance [71, 72].
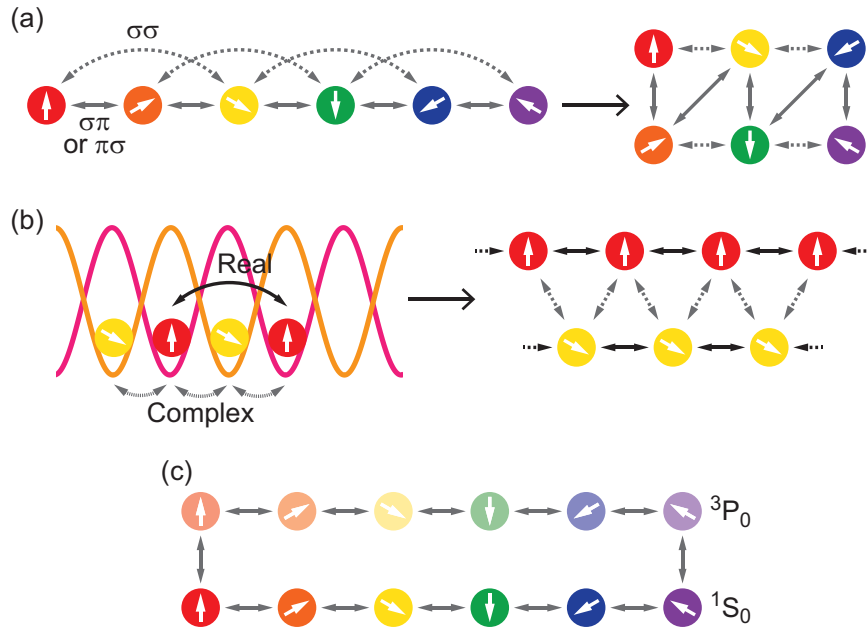
Figure 5.11: Various possible lattice strategies in synthetic dimension framework. (a) Four-unit zig-zag lattices. (b) Semi-synthetic zig-zag lattice proposed in Ref. [169]. (c) Cyclic coupling with 12 synthetic sites using the clock states of ^{173}Yb.

Chapter 6

Photoassociation Spectroscopy of 173 Ytterbium Fermi gas

This chapter describes our measurement on photoassociation spectrum of 173 ytterbium atoms. The experimental and theoretical results are published in the following paper.

- J. H. Han, J. H. Kang, M. Lee, and Y. Shin, *"Photoassociation spectroscopy of ultracold ^{173}Yb atoms near the intercombination line,"* Phys. Rev. A **97**, 013401 (2018).

6.1 Introduction

Photoassociation (PA) is a process in which two colliding atoms form an excited molecule by absorbing a photon. PA spectroscopy provides a versatile tool for probing the physics of rovibrational molecular states [171] and precisely determining the collisional properties of atoms, such as scattering length

and interatomic potential coefficients [87]. Furthermore, the PA process can be actively used to control the strength of atomic interaction via coupling to an excited molecular state, a phenomenon called optical Feshbach resonance (OFR) [92–97], and to measure pair correlations in strongly correlated atomic gas systems [54, 172].

Recently, there has been broad interest in studies on the PA physics of two-valence-electron atoms such as Yb [83, 87, 95, 95, 173–177], Sr [97, 178–183], and Ca [184, 185]. These atoms have narrow ^1S–^3P intercombination transition, which is beneficial for the precise determination of PA resonances and enables the implementation of OFR without significant atom loss [94–97]. In particular, Yb atoms have rich, stable isotopes, including five spinless bosons (^{168}Yb, ^{170}Yb, ^{172}Yb, ^{174}Yb, and ^{176}Yb) and two fermions (^{171}Yb, with a nuclear spin of $i = 1/2$ and ^{173}Yb, with $i = 5/2$), providing an interesting opportunity to study the mass scaling of PA physics [87, 175]. To date, many PA spectra of Yb atoms have been reported for bosonic isotopes [87, 173–175], fermionic ^{171}Yb [95], and isotopic mixtures [176, 177]. However, the complete PA spectrum of fermionic ^{173}Yb, with its high nuclear spin, is still unknown, although a couple of PA resonances have been reported [54, 87, 186]. In addition, the ^{173}Yb Fermi gas system has been discussed as a candidate platform for studies of exotic SU($\mathcal{N} >$ 2) quantum magnetism [30]. Information on the PA spectrum of ^{173}Yb near the intercombination line is highly desirable for such a quantum simulation application [187].

In this experiment, we report the PA spectrum of a degenerate Fermi gas of ^{173}Yb atoms near the dissociation limit of the $|^1S_0, f = 5/2\rangle \rightarrow |^3P_1, f' = 7/2\rangle$ intercombination transition. We measured an atom-loss spectrum as a function of the frequency of the PA light and we observed eighty PA resonances in the

spectrum on the red-detuned side of the atomic resonance down to -1 GHz. The high density of the spectral lines can be attributed to the high nuclear spin number of ^{173}Yb, which we confirmed by performing a multi-channel calculation of the molecular energy levels based on known spectroscopic results. To collect further spectroscopic information on the excited molecular states, we investigated the Zeeman effect in the spectrum near the frequency detuning of -0.8 GHz. By employing various two-component spin mixture samples, we determined the quantum numbers of the Zeeman sublevels and estimated the g factor of the molecular state corresponding to the PA line at -796 MHz detuning. Finally, we measured the two-body loss rates under PA light for several pronounced PA resonances. Our measurement results provide a starting point for studies of the PA physics of fermionic ^{173}Yb atoms, although further theoretical efforts will be required to interpret the measured spectra.

6.2 Experiment

Sample preparation

The atomic sample was evaporatively cooled by lowering the trap depth, and after cooling, it was held for an additional 0.3 s to ensure equilibrium. The final sample was an equal mixture of all six spin components of the $^1S_0$ ground state, containing approximately 3.1×10^5 atoms. The sample temperature was measured to be $T \approx 130$ nK. The *in situ* density distribution of the trapped sample was found to be well fit by a Gaussian profile with a $1/e^2$ radius of $\{\sigma_x, \sigma_y, \sigma_z\} \approx \{12.0, 7.5, 3.8\}$ μm, and the central density was estimated to be $n_0 \approx 1.6 \times 10^{14}$ cm^{-3}, corresponding to a Fermi energy of $E_F = \hbar^2 (\pi^2 n_0)^{2/3}/(2m) \approx$

$k_B \times 190$ nK, where $\hbar$ is the Planck constant h divided by 2π, m is the atomic mass, and k_B is the Boltzmann constant. To measure the sample condition, we take absorption image using the $^1S_0$–$^1P_1$ transition.

Photoassociation spectroscopy

PA resonances were detected via atom loss by illuminating the trapped sample with a pulsed PA laser beam. The linewidth of our PA laser was < 70 kHz, which is sufficiently narrow to probe excited molecular states with a natural linewidth of $\Gamma_{\text{nat}}/2\pi \approx (2\Gamma_{\text{a}})/2\pi = 364$ kHz, where Γ_a is the atomic linewidth of the $^1S_0$–$^3P_1$ transition [94]. The PA laser beam was σ^-–polarized and focused onto the sample with a Gaussian beam waist of ≈ 114 μm, which was large to uniformly irradiate the entire sample. We obtained a PA spectrum by measuring the remaining atom number fraction η_a as a function of the frequency ν of the PA laser beam. For each ν, we determined η_a by measuring the numbers of atoms with and without application of the PA laser beam, respectively.

6.3   Photoassociation spectrum

Figure 6.1 shows the PA spectrum measured for $\delta\nu = \nu - \nu_0 = -1 \sim 0$ GHz, where $\nu_0 = 539\,384\,174(10)$ MHz is the resonance frequency for the $|^1S_0, f = 5/2\rangle \rightarrow |^3P_1, f' = 7/2\rangle$ atomic transition [74]. In the measurement, we reduced the PA beam intensity I_{PA} and the pulse duration τ in a piecewise manner as we approach the atomic resonance to avoid power broadening and photon scattering loss effects, where $I_{\text{PA}} = 0.037 - 0.74$ W/cm^2 and $\tau = 30 - 100$ ms. The saturation intensity for the atomic transition is $I_{\text{sat}} = 0.14$ mW/cm^2. The spectrum shows a high density of spectral lines, and we identified eighty PA resonances in
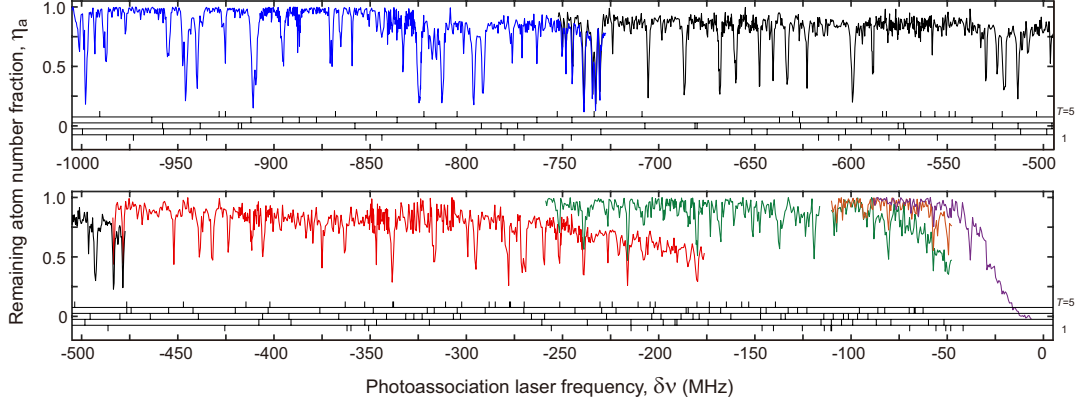
Figure 6.1: Photoassociation (PA) spectrum of unpolarized ^{173}Yb atoms at ultralow temperature. The various colored lines represent different PA laser beam conditions with intentisy I_{PA} and pulse duration τ: blue (-1000 to -727 MHz, I_{PA} =0.74 W/cm^2, τ = 100 ms), black (-752 to -477 MHz, 0.37 W/cm^2, 100 ms), red (-484 to -176 MHz, 74 mW/cm^2, 100 ms), green (-259 to -48 MHz, 74 mW/cm^2, 50 ms), orange (-110 to -48 MHz, 74 mW/cm^2, 30 ms), and purple (-88 to 0 MHz, 37 mW/cm^2, 30 ms). The barcode lines at the bottom of the plot show the numerical calculation results obtained for the adiabatic molecular potentials with $T = 1$(bottom) to 5(top) (Fig. 2).

the range of -1 GHz $< \delta\nu < -38$ MHz. For $\delta\nu > -38$ MHz, it was difficult to unambiguously identify PA resonances because of high photon scattering loss near the atomic resonance. The positions ν_b and linewidths Γ_b of the spectral lines were determined from Lorentzian line fits to the measured data and are listed in Table 6.1. In our experiment, the ac Stark shift due to the dipole trapping beams was < 100 kHz and insignificant, and the thermal broadening was negligible for $k_B T/h \approx 4$ kHz.

To understand the observed high density of the spectral lines, we calculate the bound state energy levels for two ^{173}Yb atoms in the $^3P_1 + ^1S_0$ channel, following the methods presented in Refs. [179, 187]. The Hamiltonian for the

two atoms is

$$\hat{H} = \frac{p_r^2}{2\mu} + \frac{\hbar^2}{2\mu r^2}R(R+1) + V_{\mathrm{BO}}(r) + \hat{H}_{\mathrm{hf}}, \tag{6.1}$$

where the first and second terms represent the radial and angular kinetic energies, respectively of the nuclei of the two atoms, $V_{\mathrm{BO}}(r)$ is the electronic Born-Oppenheimer (BO) potential, and $\hat{H}_{\mathrm{hf}}$ is the hyperfine interaction term. Here, μ and r denote the reduced mass and radial separation of the two nuclei, respectively, and R is the quantum number for the overall rotation of the atom dimer. The BO potential is given by

$$V_{\mathrm{BO}}(r) = -\frac{C_6}{r^6}\left(1 - \frac{\sigma^6}{r^6}\right) - s\frac{C_3^\Omega}{r^3}. \tag{6.2}$$

The first term is the Lennard-Jones potential and the second term represents the dipole-dipole interaction, where $s = +1(-1)$ for the *gerade* (*ungerade*) potential and Ω is the projection of the angular momentum $\boldsymbol{J} = \boldsymbol{j}_1 + \boldsymbol{j}_2$ on the internuclear axis. Here, $\boldsymbol{j}_{k=1,2}$ is the total electronic angular momentum of atom k. From Ref. [175], we have $C_6 = 2.41(0.22) \times 10^3 E_h a_0^6$, $\sigma = 8.5(1.0)a_0$, and $C_3^0 = -2C_3^1 = -0.1949(11) \times E_h a_0^3$, where E_h is the Hartree energy and a_0 is the Bohr radius. The hyperfine interaction is described by [187],

$$\hat{H}_{\mathrm{hf}} = A(\boldsymbol{i}_1 \cdot \boldsymbol{j}_1) + B\frac{3(\boldsymbol{i}_1 \cdot \boldsymbol{j}_1)^2 + \frac{3}{2}(\boldsymbol{i}_1 \cdot \boldsymbol{j}_1) - i_1(i_1 + 1)j_1(j_1 + 1)}{2i_1 j_1(2i_1 - 1)(2j_1 - 1)}, \tag{6.3}$$

where we assume that the $k = 2$ atom belongs to the $^1S_0$ state, i.e., $\boldsymbol{i}_2 \cdot \boldsymbol{j}_2 = 0$. We adopt the values of $A/h = -1094.328$ MHz and $B/h = -826.635$ MHz from Ref. [74].

At the low temperature of our experiment, we expect only s-wave ($R = 0$) collisions for two fermionic ^{173}Yb atoms in the $^1S_0$ ground state, and the initial $^1S_0 + ^1S_0$ dimer state should have total angular momentum of $T = F = I = 0, 2,$ or 4 and even spatial parity ($p = 1$). Here, $\boldsymbol{F} = \boldsymbol{f}_1 + \boldsymbol{f}_2$ and $\boldsymbol{I} = \boldsymbol{i}_1 + \boldsymbol{i}_2$. According

to the selection rules for optical excitation, excited molecular states should have $T = 1, 2, 3, 4$, or 5 and odd parity ($p = -1$). In the modified Hund's case (e) that is relevant to our condition, with large spin-orbit coupling and hyperfine interaction, we count 205 different configurations of (T, F, R) for the final states of the PA transition. Note that the transition from the initial $^1\Sigma_g$ molecular state to a *gerade*-symmetry state is possible because the *u-g* symmetry is broken in Hund's case (e) [188].

The adiabatic potentials for molecular states can be obtained by diagonalizing the Hamiltonian in Eq. 6.1 via basis transformation between different Hund's cases [187, 189]. For a short distance r, the BO potential, which is diagonal under Hund's case (c), is dominant. In this case, the basis set is given by $|\gamma\rangle = |J, \Omega, I, \iota, \Phi, (T, M_T, p)\rangle$, where ι and Φ are the projections of $\boldsymbol{I}$ and $\boldsymbol{F}$ onto the internuclear axis, respectively, and M_T is the projection of the total angular momentum onto a space-fixed quantization axis. At large r, i.e., when the two atoms are far apart, Hund's case (d) becomes relevant and results in the product basis of internal atomic states and nuclear rotations, $|\pi\rangle = |f_1, m_1, f_2, m_2, R, (T, M_T, p)\rangle$. In the intermediate range of r, we consider Hund's case (e), in which rotational and hyperfine interactions are diagonal and use a basis of $|\epsilon\rangle = |f_1, f_2, F, R, (T, M_T, p)\rangle$.

The calculated adiabatic potentials for the 205 channels for excited molecular states are displayed in Fig. 6.2. At small r, the potentials are grouped into four branches, representing the four different dipole-dipole interaction configurations, and at large r, they converge to three asymptotes near the dissociation limit, which correspond to $f'_1 = 3/2, 5/2$, and 7/2, respectively. We note that some of the potentials related to the $f'_1 = 5/2$ asymptote have local minima near ~ 70 a_0 (Fig. 2 inset), predicting purely-long-range molecular states. This

is due to the large hyperfine structure of heavy Yb atoms, and purely-long-range states have been observed with ^{171}Yb [95].

From the calculated molecular potentials, we compute the bound state energy levels using a multi-channel discrete variable representation (DVR) method [187, 189, 190]. This calculation predicts more than 200 bound states in the range of -1 GHz $< \delta\nu < -38$ MHz, whose positions are indicated in Fig. 6.1 alongside the measured PA spectrum. We checked the validity of our DVR method with LeRoy-Bernstein formula. The lowest potentials of 0_u branch with $T = 1, 2$ can be approximated to from of r^{-n}, which follows vibrational progression. (See also Ref. [191]) Considering the limited experimental sensitivity, the observed high density of the spectral lines is reasonably explained by the calculated results. With regard to the resonance positions, a better comparison might be enabled by using an iterative fitting method to tune the potential coefficients values [175], but because of the heavy calculation load involved, we will leave such an effort as a topic for future studies.

6.3.1 Zeeman effect

Information on the excited molecular states can be further obtained by investigating the Zeeman effect on the spectrum by applying an external magnetic field B [193]. In the presence of B, the total angular momentum T and its projection M_T onto the field direction are still good quantum numbers of the system and for low B the Zeeman shift is described as $\Delta E_Z = \mu_B g B M_T$, where μ_B is the Bohr magneton and g is the Lande g-factor of the molecular state. Thus, the quantum number T and the g-factor value of the molecular state can be directly revealed by the number of Zeeman sublevels and the magnitude of their spec-
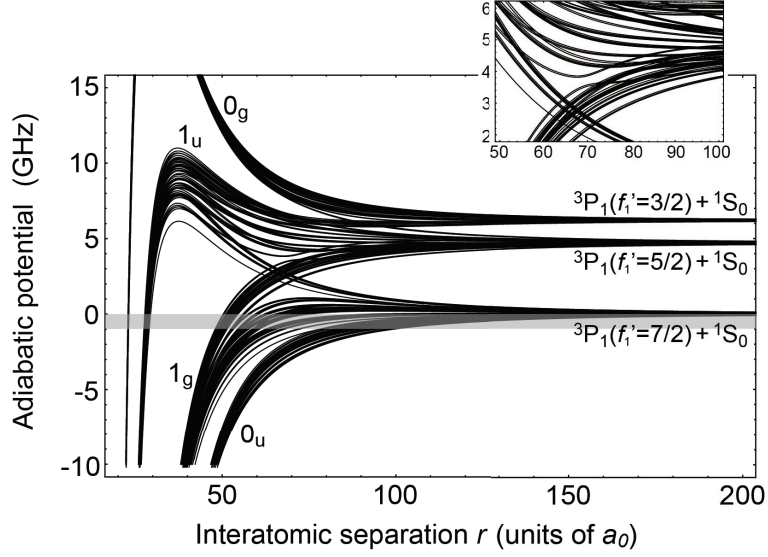
Figure 6.2: Adiabatic molecular potentials for a $^{173}\text{Yb}_2$ dimer in the $^1S_0+^3P_1$ channel as functions of the interatomic separation r. The molecular potentials for 205 different (T, F, R) configurations are displayed, which are accessible via PA from the initial s-wave colliding atoms in the $^1S_0+^1S_0$ channel. At large r, the potentials converge to three asymptotic branches, which correspond to excited atomic states with hyperfine numbers of $f_1' = 3/2, 5/2$, and $7/2$. Some of the potentials have a local minimum (inset), possibly hosting purely-long-range bound states [95]. The energy offset is adjusted to the $f_1' = 7/2$ asymptote. The shaded region indicates the spectral range of our measurements.

tral splitting for B, respectively. The value of g is sensitively determined by the interatomic potential [184, 185].

In this section, we describe an experimental investigation of the Zeeman splitting of a few PA lines. In the situation where a large number of PA lines from many molecular potentials are observed in a complicated pattern with high spectral density, identifying the T numbers for some PA lines would be very beneficial for future theoretical efforts to make a full account of the observed

PA spectrum.

We applied the magnetic field along the axis of the PA laser beam and measured the PA spectra for various B (Fig. 6.3). The scan range of $\delta\nu$ was chosen to be from -820 MHz to -780 MHz, where for $B = 0$ G, three pronounced PA lines are located at $\delta\nu = -812.5$ MHz, -796.2 MHz, and -791.3 MHz, with relatively large linewidths of > 1 MHz. The latter two PA lines have been reported in previous experiments [54, 87, 186]. With increasing B, each spectral peak broadens and splits into multiple weak peaks. The Zeeman splitting response appears relatively rapidly for the line at -791.3 MHz and slowly for the line at -812.5 MHz, reflecting the different magnitudes of gT for these PA lines. Asymmetric shifting toward negative detuning is observed, which we attribute mainly to the σ^- polarization of the PA light, which allows only $\Delta M_T = -1$ transitions.

For $B > 30$ G, the spectrum shows a group of fully resolved Zeeman peaks with linewidths of ~ 1 MHz. To determine the M_T numbers of the Zeeman peaks, we measured the PA spectra of two-component spin mixture samples. When such a sample is prepared with two spin components with magnetic Zeeman numbers of m_{f_1} and m_{f_2}, the initial dimer state for s-wave collision in ${}^1S_0 + {}^1S_0$ has a specific quantum number of $M_T = m_{f_1} + m_{f_2}$, and with a σ^-–polarized PA laser beam, this state can be coupled only to excited molecular states with $M_T = m_{f_1} + m_{f_2} - 1$. Thus, the corresponding M_T number can be assigned to Zeeman peaks that appear in the PA spectrum of such a two-component sample. In our experiment, we employed five binary spin mixtures of $m_{f_1} = -5/2$ and $m_{f_2} = \{-3/2, -1/2, 1/2, 3/2, 5/2\}$ [61] and the PA spectra of the samples were measured at $B = 33.2$ G [Fig. 6.4(b)]. As expected, each spectrum shows a subset of the Zeeman peaks observed in the PA spectrum of a

fully balanced spin mixture [Fig. 6.4(a)]. To suppress unwanted optical pumping by the PA light into different spin states, we set $I_{PA} = 0.16$ W/cm^2 and $\tau = 100$ ms to obtain $\Gamma_{sc}\tau \approx 0.8$, where Γ_{sc} is the Rayleigh scattering rate of the PA light at $\delta\nu = -800$ MHz.

The main finding from the M_T analysis is that the three Zeeman peaks that are almost equally spaced in the detuning range of -805 MHz $< \delta\nu <$ -798 MHz have $M_T = -3, -2$, and -1, respectively. We find that Zeeman peaks are also located at the positions linearly extrapolated for $M_T = 0, 1, 2$, and 3 from these three Zeeman peaks and, in particular, that the peak position corresponding to $M_T = 0$ coincides with the zero-field PA line at -796.2 MHz. From these observations and the fact that there is no $M_T = -4$ Zeeman peak at the corresponding expected spacing from the $M_T = -3$ peak, we infer that the total angular momentum number of the PA line at $\delta\nu = -796.2$ MHz is $T = 3$. From a linear fit to the seven Zeeman peak positions, a g-factor of $g = 0.056(3)$ can be determined, which is approximately ten times smaller than the atomic value of $g_F = 0.426$ for the $^3P_1$ state. In Fig. 6.4(d), we display the PA resonance positions measured from the data in Fig. 6.3 as a function of B, and the Zeeman splitting lines predicted from the measured g-factor are found to reasonably fit the experimental data. For a high B of approximately ≈ 50 G, the PA resonance positions slightly deviate from the predictions toward a negative detuning except for $M_T = 0$, indicating higher-order Zeeman effects.

Although the M_T information is helpful for deciphering the linear Zeeman splitting of the PA line at -796.2 MHz, an analysis of the Zeeman effects of the other two PA lines is not straightforward. First, we observe no $M_T = -1$ Zeeman peaks for these two PA lines, although such peaks should exist because $T \geq 1$. Second, each PA spectrum for $M_T = -3$ and -4 shows four resonances

[Fig. 4(b)], which means that our PA spectrum for a high B of > 30 G must involve Zeeman contributions from other PA lines outside the measurement range. Theoretical support will be critical for a complete understanding of the observed Zeeman effects.

6.3.2 Two-body loss rate

Finally, we characterized some of the pronounced PA resonances by measuring the two-body loss rate K_2 under PA light. K_2 contains important information such as the Franck-Condon factor for the optical transition [171, 194] and the so-called optical length l_{opt} that describes the magnitude of the change of the scattering length due to the OFR [94, 175, 183].

In the presence of PA light, the atom density n evolves as,

$$\dot{n}(t) = -2K_2 n^2 - \gamma n, \tag{6.4}$$

where the first term represents the two-body PA process and the second term accounts for one-body decay processes such as Rayleigh photon scattering loss and background trap loss. For a case of a trapped sample, considering its inhomogeneous density distribution, the rate equation for the total number of atoms N is given by $\dot{N}(t) = -2K_2 \frac{N^2}{V_e} - \gamma N$, where $V_e = (2\pi)^{3/2} \sigma_x \sigma_y \sigma_z$ is the effective volume of the sample for a Gaussian density distribution. To avoid nonlinear effects caused by sample heating on K_2 and V_e, we measured the decay rate γ' of N from an exponential fit to the initial 10 ms of $N(t)$ data and calculated K_2 as $K_2 = \frac{V_e}{2\bar{N}}(\gamma' - \gamma)$. Here $\bar{N}$ denotes the average number of atoms over the initial 10 ms and γ was independently measured at off-resonance detuning which is more than $4\Gamma_b$ away from the PA resonance (Fig. 6.5).

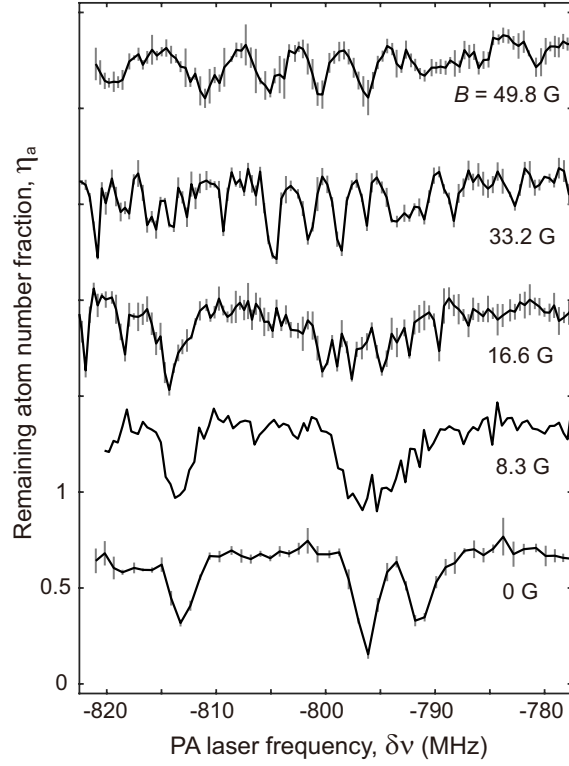Figure 6.3: PA spectra near $\delta\nu = -800$ MHz for various magnetic fields of $B = 0$ G, 8.3 G, 16.6 G, 33.2 G, and 49.8 G. The PA laser beam was σ^--polarized and the magnetic field was applied along the beam axis. All data points except those at $B = 8.3$ G were obtained by averaging five independent measurements and the error bars denote their standard deviations. The data are offset for clarity.
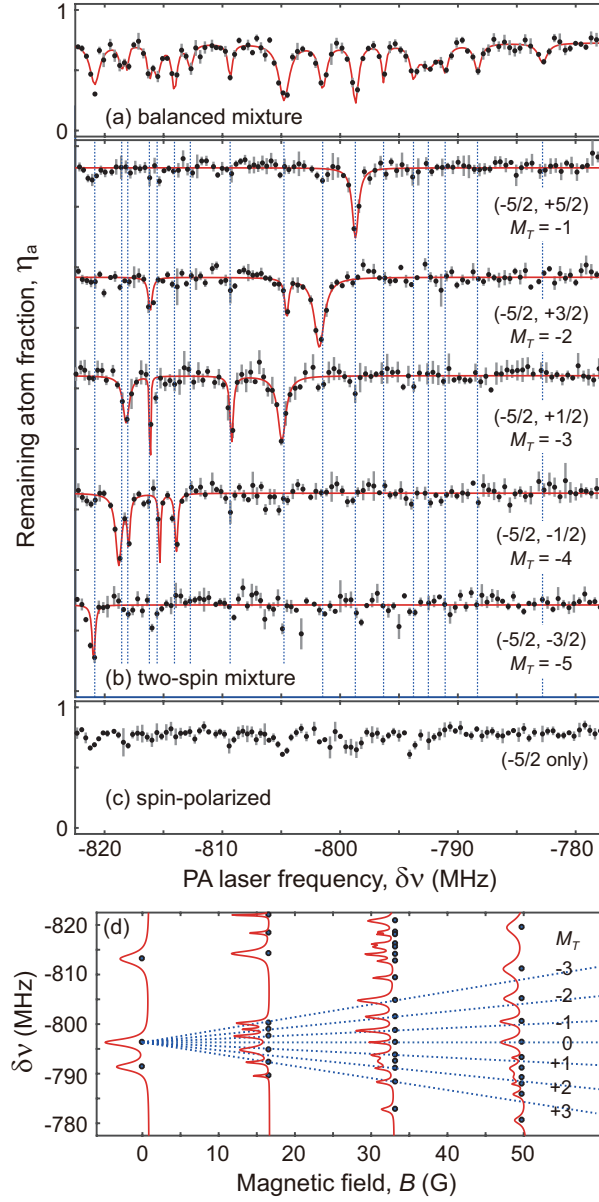
Figure 6.4: PA spectra of various spin mixtures for $B = 33.2$ G: (a) an unpolarized spin mixture, as shown in Fig. 6.3; (b) two-component spin mixtures; and (c) a spin-polarized Fermi gas. The red lines show the sums of the Lorentzian fit curves to guide the eye, and the dotted vertical lines indicate the resonance positions as fitted from the spectrum of the balanced mixture. (d) Zeeman splitting of the -796.2 MHz resonance (dotted lines), with markers representing the measured PA resonance positions.

Figure 6.5: Atom loss curves as functions of the pulse duration τ of the PA light for $\delta\nu = -791.3$ MHz (on resonance, solid green circles) and $\delta\nu = -784$ MHz (off resonance, open blue circles) with $I_{PA} = 0.74$ W/cm^2. The solid lines are exponential fits to the initial 10 ms of decay data. All data points were obtained by averaging the results of five independent runs of the same experiment.

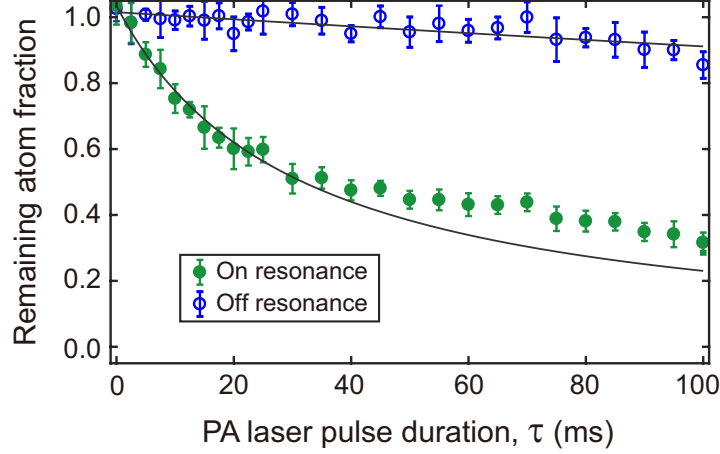The K_2 is measured for the three PA resonances at $\delta\nu = -38.1$ MHz, -791.3 MHz, and -796.2 MHz, and obtained $K_2 = 1.0(3) \times 10^{-12}$ cm^3/s with $I_{PA} = 74$ mW/cm^2, $K_2 = 0.5(1) \times 10^{-12}$ cm^3/s with $I_{PA} = 0.74$ W/cm^2, and $K_2 = 0.8(5) \times 10^{-12}$ cm^3/s with $I_{PA} = 0.74$ W/cm^2, respectively. In the cold collision limit, the optical length is given as $l_{opt} = \eta\mu K_2/(8\pi\hbar)$ [94, 97], where η is the enhancement factor of the molecular linewidth with respect to the natural linewidth. Assuming that η is order of unity, our measurement results suggest that $l_{opt} \sim 10a_0$ at $I_{PA} = 1$ W/cm^2. It is surprising that the estimated value of l_{opt} is more than two orders of magnitude smaller than the values reported for other Yb isotopes [175, 187, 195]. It would be worthwhile to investigate the tempearture and $\delta\nu$ dependence of K_2 in a further systematic manner [175].

6.4   Conclusions and outlooks

In this chapter, the measurement of PA spectrum of a degenerate Fermi gas of ^{173}Yb atoms near the dissociation limit of the $^1S_0$–$^3P_1$ intercombination transition is reported. Some of the prominent PA lines are studied by investigating their Zeeman splitting and measuring their two-body loss rates under PA light. The high density of the spectral lines was accounted for by the calculation of the molecular energy levels based on an extended version of Hund's case (e), but further theoretical investigation will be necessary for spectral identification of the observed molecular states. This will improve our understanding of the collisional properties of Yb atoms in $^1S+^3P$, which are important for many applications using Yb atoms, such as optical clocks [80, 196] and the simulation of novel quantum magnetism [30, 54].

Finally, we note that when the Zeeman splitting of a PA line is fully understood in terms of its molecular quantum number, the spin-dependent PA transitions may find immediate use in probing interspin correlations, particularly, in optical lattice experiments [54, 197]. For example, the correlations between the $m_f = m$ and $-m$ spin states may be distinctively detected by using the PA resonance at -798.4 MHz for $B = 33.2$ G. Thus, it might be worthwhile to search for an isolated $T = 5$ PA line whose Zeeman lines are spectroscopically well resolved and have reasonable transition strengths for a moderate magnetic field.

Table 6.1: Measured PA resonances ν_b and the corresponding linewidths Γ_b from Lorentzian fits to the individual resonances depicted in Fig. 6.1 [192]. The errors represent the 95% confidence intervals from the fits. For some resonances, no linewidth is given due to insufficient data points. Note that the PA laser beam intensity varies over the frequency detuning (see the caption of Fig. 1).

ν_b (MHz)	$\Gamma_b/2\pi$ (MHz)	ν_b (MHz)	$\Gamma_b/2\pi$ (MHz)	ν_b (MHz)	$\Gamma_b/2\pi$ (MHz)
-997.8 ± 0.1	1.3 ± 0.2	-724.1 ± 0.7	$-$	-338.5 ± 0.2	1.3 ± 0.5
-993.1 ± 0.3	0.6 ± 0.4	-724.1 ± 0.7	$-$	-316.6 ± 0.4	1.1 ± 0.3
-987.4 ± 0.2	1.6 ± 0.6	-705.4 ± 0.1	0.8 ± 0.2	-299.4 ± 0.2	$-$
-955.0 ± 0.2	1.5 ± 0.5	-686.5 ± 0.1	1.0 ± 0.3	-295.1 ± 0.1	1.3 ± 0.4
-945.9 ± 0.1	2.1 ± 0.4	-668.1 ± 0.1	1.0 ± 0.2	-278.2 ± 0.2	$-$
-940.0 ± 0.1	1.2 ± 0.3	-659.9 ± 0.1	1.1 ± 0.3	-270.2 ± 0.4	2.3 ± 1.3
-925.4 ± 0.1	0.5 ± 0.4	-647.6 ± 0.1	0.5 ± 0.3	-259.5 ± 0.5	$-$
-910.4 ± 0.2	2.8 ± 0.5	-640.5 ± 0.1	0.5 ± 0.3	-251.7 ± 0.5	$-$
-895.3 ± 0.1	1.3 ± 0.3	-633.1 ± 0.1	1.0 ± 0.3	-238.9 ± 0.1	0.9 ± 0.7
-887.6 ± 0.1	0.5 ± 0.2	-622.9 ± 0.1	0.6 ± 0.2	-226.4 ± 0.5	$-$
-870.2 ± 0.2	1.6 ± 0.5	-599.1 ± 0.1	1.4 ± 0.3	-220.6 ± 0.2	$-$
-865.3 ± 0.2	0.9 ± 0.4	-588.5 ± 0.1	0.7 ± 0.3	-216.1 ± 0.1	0.7 ± 0.3
-859.3 ± 0.2	0.4 ± 0.3	-557.7 ± 0.3	$-$	-207.8 ± 0.3	1.9 ± 0.9
-832.9 ± 0.1	0.8 ± 0.3	-529.8 ± 0.1	0.6 ± 0.5	-197.4 ± 0.7	2.6 ± 2.2
-824.5 ± 0.1	2.1 ± 0.3	-523.9 ± 0.1	$-$	-193.7 ± 1.1	$-$
-812.5 ± 0.1	1.5 ± 0.4	-520.3 ± 0.1	1.5 ± 0.4	-190.2 ± 0.3	1.1 ± 0.9
-796.2 ± 0.1	1.4 ± 0.2	-513.3 ± 0.1	1.1 ± 0.3	-184.5 ± 0.3	1.9 ± 0.9
-791.3 ± 0.1	1.3 ± 0.2	-496.3 ± 0.2	$-$	-180.0 ± 0.1	1.5 ± 0.4
-776.1 ± 0.3	0.6 ± 0.4	-492.8 ± 0.1	1.3 ± 0.4	-168.0 ± 0.2	1.4 ± 0.9
-771.0 ± 1.2	$-$	-483.3 ± 0.1	1.1 ± 0.3	-137.3 ± 0.2	1.5 ± 0.8
-763.3 ± 0.2	0.6 ± 0.3	-478.5 ± 0.1	0.9 ± 0.3	-119.1 ± 0.5	$-$
-750.1 ± 0.1	$-$	-452.0 ± 0.2	0.6 ± 0.3	-80.7 ± 0.2	1.0 ± 0.7
-748.3 ± 0.1	$-$	-438.6 ± 0.1	1.2 ± 0.5	-57.1 ± 0.5	$-$
-744.9 ± 0.1	0.5 ± 0.3	-432.1 ± 0.1	0.8 ± 0.5	-49.5 ± 0.2	1.2 ± 0.9
-738.9 ± 0.1	1.1 ± 0.2	-423.6 ± 0.1	$-$	-38.1 ± 0.2	0.9 ± 0.7
-734.4 ± 0.1	0.7 ± 0.3	-405.7 ± 0.1	1.1 ± 0.6	$-$	$-$
-732.8 ± 0.1	0.9 ± 0.2	-374.9 ± 0.4	$-$	$-$	$-$
-730.7 ± 0.1	0.5 ± 0.2	-363.1 ± 0.1	$-$	$-$	$-$

Chapter 7

Conclusions and Outlooks

In this dissertation, I explained the our apparatus for generating ultracold ytterbium quantum gases and described how to reach quantum degeneracy. In this apparatus, a Bose-Einstein condensate of ^{174}Yb and a degenerate Fermi gas of ^{173}Yb were repeatedly generated. Using typical Raman two-photon scheme, properly designed laser fields induced artificial gauge potentials for the neutral fermions, which realized equal Rashba-Dresselhaus (1D) spin-orbit coupling. For ^{173}Yb, the multi-order Raman process and the double resonance phenomena were observed due to high spin nature of the system and the Raman spectra for various magnetic fields were investigated.

Moreover, the basic concepts of quantum Hall physics and the its connection to the topological world were examined, where Berry phase of the lattice band protects the topological phase. As a simplest example, Harper-Hofstadter (HH) Hamiltonian, which describes the movement of a charged particle under the square lattice and the perpendicular magnetic field, was introduced. To realize HH Hamiltonian, topological band engineering using ^{173}Yb in optical lattices was discussed under synthetic dimensional framework. Taking the advantage of

^{173}Yb, synthetic Hall tube, which is a Hall ladder with periodic boundary condition, was realized. In this experiment, the band gap closing due to the topological phase transition was revealed by comparing two different timescales of quench dynamics, where each of them represents the band energy.

The topological matters are expected to show exotic physical properties which is robust against the continuous change of parameters. For instance, the topological matters may demonstrate chiral or step-like conductance, or even magnetoelectric effect. To my knowledge, the most common feature of a typical topological matter (not all, but especially for an insulator) is the presence of edge current, which is a hallmark of the topological nature of the system. Inside the vacuum, the topological invariant is zero, while in the bulk is not. This is why the study of interface in topological materials, where two different topologies get faced, is important. The synthetic Hall tube experiment provides first experimental investigation on the crossover between the two distinct boundary conditions. Along with the various symmetries inherent in the system, these topological properties may become reinforced.

Finally, photoassociation spectrum of ^{173}Yb was measured to obtain basic information on the interaction effects in these atomic systems. Despite complicated adiabatic potential structure, the quantum number of some of the pronounced resonances were discovered. In the future experiment, control of interaction strength in ^{173}Yb quantum gas is necessary, which enriches the study of topological physics using the cold atoms in optical lattices and can be realized by orbital Feshbach resonances with the clock states.

Bibliography

[1] M. H. Anderson, J. R. Ensher, M. R. Matthews, C. E. Wieman, and E. A. Cornell, "Observation of Bose-Einstein Condensation in a Dilute Atomic Vapor," *Science*, vol. 269, no. 5221, pp. 198–201, 1995.

[2] K. B. Davis, M. O. Mewes, M. R. Andrews, N. J. Van Druten, D. S. Durfee, D. M. Kurn, and W. Ketterle, "Bose-Einstein condensation in a gas of sodium atoms," *Physical Review Letters*, vol. 75, no. 22, pp. 3969–3973, 1995.

[3] B. DeMarco and D. S. Jin, "Onset of fermi degeneracy in a trapped atomic gas," *Science*, vol. 285, no. 5434, pp. 1703–1706, 1999.

[4] F. Schreck, L. Khaykovich, K. L. Corwin, G. Ferrari, T. Bourdel, J. Cubizolles, and C. Salomon, "Quasipure bose-einstein condensate immersed in a fermi sea," *Phys. Rev. Lett.*, vol. 87, p. 080403, Aug 2001.

[5] A. G. Truscott, K. E. Strecker, W. I. McAlexander, G. B. Partridge, and R. G. Hulet, "Observation of fermi pressure in a gas of trapped atoms," *Science*, vol. 291, no. 5513, pp. 2570–2572, 2001.

[6] I. Bloch, J. Dalibard, and W. Zwerger, "Many-body physics with ultracold gases," *Rev. Mod. Phys.*, vol. 80, pp. 885–964, Jul 2008.

[7] M. R. Andrews, M.-O. Mewes, N. J. van Druten, D. S. Durfee, D. M. Kurn, and W. Ketterle, "Direct, Nondestructive Observation of a Bose Condensate," *Science*, vol. 273, no. 5271, pp. 84–87, 1996.

[8] M. R. Andrews, "Observation of Interference Between Two Bose Condensates," *Science*, vol. 275, no. 5300, pp. 637–641, 1997.

[9] I. Bloch, J. Dalibard, and S. Nascimbène, "Quantum simulations with ultracold quantum gases," *Nature Physics*, vol. 8, no. 4, pp. 267–276, 2012.

[10] M. Greiner, O. Mandel, T. Esslinger, T. W. Hänsch, and I. Bloch, "Quantum phase transition from a superfluid to a mott insulator in a gas of ultracold atoms," *Nature*, vol. 415, p. 39, Jan 2002.

[11] A. L. Gaunt, T. F. Schmidutz, I. Gotlibovych, R. P. Smith, and Z. Hadzibabic, "Bose-einstein condensation of atoms in a uniform potential," *Phys. Rev. Lett.*, vol. 110, p. 200406, May 2013.

[12] J. Billy, V. Josse, Z. Zuo, A. Bernard, B. Hambrecht, P. Lugan, D. Clément, L. Sanchez-Palencia, P. Bouyer, and A. Aspect, "Direct observation of anderson localization of matter waves in a controlled disorder," *Nature*, vol. 453, p. 891, Jun 2008.

[13] V. L. Berezinskii, "Destruction of long-range order in one-dimensional and two-dimensional systems having a continuous symmetry group I. classical systems," *Sov. Phys. JETP*, vol. 32, no. 3, p. 493, 1971.

[14] J. M. Kosterlitz and D. J. Thouless, "Ordering, metastability and phase transitions in two-dimensional systems," *Journal of Physics C: Solid State Physics*, vol. 6, no. 7, p. 1181, 1973.

[15] M. C. Revelle, J. A. Fry, B. A. Olsen, and R. G. Hulet, "1d to 3d crossover of a spin-imbalanced fermi gas," *Phys. Rev. Lett.*, vol. 117, p. 235301, Nov 2016.

[16] P. Courteille, R. S. Freeland, D. J. Heinzen, F. A. van Abeelen, and B. J. Verhaar, "Observation of a feshbach resonance in cold atom scattering," *Phys. Rev. Lett.*, vol. 81, pp. 69–72, Jul 1998.

[17] S. Inouye, M. R. Andrews, J. Stenger, H.-J. Miesner, D. M. Stamper-Kurn, and W. Ketterle, "Observation of feshbach resonances in a bose-einstein condensate," *Nature*, vol. 392, p. 151, Mar 1998.

[18] T. Loftus, C. A. Regal, C. Ticknor, J. L. Bohn, and D. S. Jin, "Resonant control of elastic collisions in an optically trapped fermi gas of atoms," *Phys. Rev. Lett.*, vol. 88, p. 173201, Apr 2002.

[19] K. M. O'Hara, S. L. Hemmer, M. E. Gehm, S. R. Granade, and J. E. Thomas, "Observation of a strongly interacting degenerate fermi gas of atoms," *Science*, vol. 298, no. 5601, pp. 2179–2182, 2002.

[20] M. Greiner, C. A. Regal, and D. S. Jin, "Emergence of a molecular bose-einstein condensate from a fermi gas," *Nature*, vol. 426, p. 537, Nov 2003.

[21] N. Goldman, G. Juzeliūnas, P. Öhberg, and I. B. Spielman, "Light-induced gauge fields for ultracold atoms," *Rep. Prog. in Phys.*, vol. 77, no. 12, p. 126401, 2014.

[22] J. Dalibard, F. Gerbier, G. Juzeliūnas, and P. Öhberg, "Colloquium: Artificial gauge potentials for neutral atoms," *Rev. Mod. Phys.*, vol. 83, pp. 1523–1543, Nov 2011.

[23] Y.-J. Lin, K. Jiménez-García, and I. B. Spielman, "Spin-orbit-coupled bose-einstein condensates," *Nature*, vol. 471, p. 83, Mar 2011.

[24] D. Jaksch and P. Zoller, "The cold atom hubbard toolbox," *Ann. Phys. (Amsterdam)*, vol. 315, no. 1, pp. 52 – 79, 2005.

[25] W. S. Bakr, J. I. Gillen, A. Peng, S. Fölling, and M. Greiner, "A quantum gas microscope for detecting single atoms in a hubbard-regime optical lattice," *Nature*, vol. 462, p. 74, Nov 2009.

[26] M. F. Parsons, F. Huber, A. Mazurenko, C. S. Chiu, W. Setiawan, K. Wooley-Brown, S. Blatt, and M. Greiner, "Site-resolved imaging of fermionic ^{6}Li in an optical lattice," *Phys. Rev. Lett.*, vol. 114, p. 213002, May 2015.

[27] M. Boll, T. A. Hilker, G. Salomon, A. Omran, J. Nespolo, L. Pollet, I. Bloch, and C. Gross, "Spin- and density-resolved microscopy of antiferromagnetic correlations in fermi-hubbard chains," *Science*, vol. 353, no. 6305, pp. 1257–1260, 2016.

[28] L. W. Cheuk, M. A. Nichols, K. R. Lawrence, M. Okan, H. Zhang, and M. W. Zwierlein, "Observation of 2d fermionic mott insulators of ^{40}K with single-site resolution," *Phys. Rev. Lett.*, vol. 116, p. 235301, Jun 2016.

[29] C. Weitenberg, M. Endres, J. F. Sherson, M. Cheneau, P. Schauß, T. Fukuhara, I. Bloch, and S. Kuhr, "Single-spin addressing in an atomic mott insulator," *Nature*, vol. 471, p. 319, Mar 2011.

[30] A. V. Gorshkov, M. Hermele, V. Gurarie, C. Xu, P. S. Julienne, J. Ye, P. Zoller, E. Demler, M. D. Lukin, and A. M. Rey, "Two-orbital su(n)

magnetism with ultracold alkaline-earth atoms," *Nature Physics*, vol. 6, p. 289, Feb 2010.

[31] J. W. Park, S. A. Will, and M. W. Zwierlein, "Ultracold dipolar gas of fermionic ^{23}Na^{40}K molecules in their absolute ground state," *Phys. Rev. Lett.*, vol. 114, p. 205302, May 2015.

[32] M. Guo, B. Zhu, B. Lu, X. Ye, F. Wang, R. Vexiau, N. Bouloufa-Maafa, G. Quéméner, O. Dulieu, and D. Wang, "Creation of an ultracold gas of ground-state dipolar ^{23}Na^{87}Rb molecules," *Phys. Rev. Lett.*, vol. 116, p. 205303, May 2016.

[33] P. K. Molony, P. D. Gregory, Z. Ji, B. Lu, M. P. Köppinger, C. R. Le Sueur, C. L. Blackley, J. M. Hutson, and S. L. Cornish, "Creation of ultracold ^{87}Rb^{133}Cs molecules in the rovibrational ground state," *Phys. Rev. Lett.*, vol. 113, p. 255301, Dec 2014.

[34] T. Takekoshi, L. Reichsöllner, A. Schindewolf, J. M. Hutson, C. R. Le Sueur, O. Dulieu, F. Ferlaino, R. Grimm, and H.-C. Nägerl, "Ultracold dense samples of dipolar rbcs molecules in the rovibrational and hyperfine ground state," *Phys. Rev. Lett.*, vol. 113, p. 205301, Nov 2014.

[35] K.-K. Ni, S. Ospelkaus, M. H. G. de Miranda, A. Pe'er, B. Neyenhuis, J. J. Zirbel, S. Kotochigova, P. S. Julienne, D. S. Jin, and J. Ye, "A high phase-space-density gas of polar molecules," *Science*, vol. 322, no. 5899, pp. 231–235, 2008.

[36] L. R. Liu, J. D. Hood, Y. Yu, J. T. Zhang, N. R. Hutzler, T. Rosenband,

and K.-K. Ni, "Building one molecule from a reservoir of two atoms," *Science*, vol. 360, no. 6391, pp. 900–903, 2018.

[37] K. Gottfried and T.-M. Yan, "Quantum mechanics: Fundamentals 2nd ed.," *Springer, ISBN 0-387-22823-2*, 2004.

[38] D. A. Steck, "Quantum and atom optics," *available online at https://steck.us/teaching (revision 0.12.2, 11 April 2018)*, 2018.

[39] R. Grimm, M. Weidemüller, and Y. B. Ovchinnikov, "Optical dipole traps for neutral atoms," vol. 42 of *Advances In Atomic, Molecular, and Optical Physics*, pp. 95 – 170, Academic Press, 2000.

[40] O. Mandel, M. Greiner, A. Widera, T. Rom, T. W. Hänsch, and I. Bloch, "Coherent transport of neutral atoms in spin-dependent optical lattice potentials," *Phys. Rev. Lett.*, vol. 91, p. 010407, Jul 2003.

[41] S. Taie, Y. Takasu, S. Sugawa, R. Yamazaki, T. Tsujimoto, R. Murakami, and Y. Takahashi, "Realization of a $SU(2) \times SU(6)$ system of fermions in a cold atomic gas," *Phys. Rev. Lett.*, vol. 105, p. 190401, Nov 2010.

[42] T. Esslinger, "Fermi-hubbard physics with atoms in an optical lattice," *Annual Review of Condensed Matter Physics*, vol. 1, no. 1, pp. 129–152, 2010.

[43] A. Bansil, H. Lin, and T. Das, "Colloquium: Topological band theory," *Rev. Mod. Phys.*, vol. 88, p. 021004, Jun 2016.

[44] S. E. Dörscher, "Quantum simulation with ytterbium atoms in synthetic dimensions," *Ph.D. Thesis, Universität Hamburg*, 2013.

[45] F. Scazza, "Quantum simulation with ytterbium atoms in synthetic dimensions," *Ph.D. Thesis, Ludwig-Maximilians-Universität München*, Jan 2013.

[46] Y. Takasu, K. Maki, K. Komori, T. Takano, K. Honda, M. Kumakura, T. Yabuzaki, and Y. Takahashi, "Spin-singlet bose-einstein condensation of two-electron atoms," *Phys. Rev. Lett.*, vol. 91, p. 040404, Jul 2003.

[47] T. Fukuhara, Y. Takasu, M. Kumakura, and Y. Takahashi, "Degenerate fermi gases of ytterbium," *Phys. Rev. Lett.*, vol. 98, p. 030401, Jan 2007.

[48] T. Fukuhara, S. Sugawa, and Y. Takahashi, "Bose-einstein condensation of an ytterbium isotope," *Phys. Rev. A*, vol. 76, p. 051604, Nov 2007.

[49] S. Sugawa, R. Yamazaki, S. Taie, and Y. Takahashi, "Bose-einstein condensate in gases of rare atomic species," *Phys. Rev. A*, vol. 84, p. 011610, Jul 2011.

[50] T. Fukuhara, S. Sugawa, Y. Takasu, and Y. Takahashi, "All-optical formation of quantum degenerate mixtures," *Phys. Rev. A*, vol. 79, p. 021601, Feb 2009.

[51] A. H. Hansen, A. Khramov, W. H. Dowd, A. O. Jamison, V. V. Ivanov, and S. Gupta, "Quantum degenerate mixture of ytterbium and lithium atoms," *Phys. Rev. A*, vol. 84, p. 011606, Jul 2011.

[52] A. O. Jamison, J. N. Kutz, and S. Gupta, "Atomic interactions in precision interferometry using bose-einstein condensates," *Phys. Rev. A*, vol. 84, p. 043643, Oct 2011.

[53] V. V. Ivanov, A. Khramov, A. H. Hansen, W. H. Dowd, F. Münchow, A. O. Jamison, and S. Gupta, "Sympathetic cooling in an optically trapped mixture of alkali and spin-singlet atoms," *Phys. Rev. Lett.*, vol. 106, p. 153201, Apr 2011.

[54] S. Sugawa, K. Inaba, S. Taie, R. Yamazaki, M. Yamashita, and Y. Takahashi, "Interaction and filling-induced quantum phases of dual mott insulators of bosons and fermions," *Nature Physics*, vol. 7, p. 642, Jun 2011.

[55] H. Hara, Y. Takasu, Y. Yamaoka, J. M. Doyle, and Y. Takahashi, "Quantum degenerate mixtures of alkali and alkaline-earth-like atoms," *Phys. Rev. Lett.*, vol. 106, p. 205304, May 2011.

[56] S. Dörscher, A. Thobe, B. Hundt, A. Kochanke, R. Le Targat, P. Windpassinger, C. Becker, and K. Sengstock, "Creation of quantum-degenerate gases of ytterbium in a compact 2d-/3d-magneto-optical trap setup," *Review of Scientific Instruments*, vol. 84, no. 4, p. 043109, 2013.

[57] F. Scazza, C. Hofrichter, M. Höfer, P. C. De Groot, I. Bloch, and S. Fölling, "Observation of two-orbital spin-exchange interactions with ultracold su(n)-symmetric fermions," *Nature Physics*, vol. 10, p. 779, Aug 2014.

[58] G. Pagano, M. Mancini, G. Cappellini, P. Lombardi, F. Schäfer, H. Hu, X.-J. Liu, J. Catani, C. Sias, M. Inguscio, and L. Fallani, "A one-dimensional liquid of fermions with tunable spin," *Nature Physics*, vol. 10, p. 198, Feb 2014.

[59] V. D. Vaidya, J. Tiamsuphat, S. L. Rolston, and J. V. Porto, "Degenerate

bose-fermi mixtures of rubidium and ytterbium," *Phys. Rev. A*, vol. 92, p. 043604, Oct 2015.

[60] M.-S. Kim, M. Lee, J. H. Han, and Y.-i. Shin, "Experimental apparatus for generating quantum degenerate gases of ytterbium atoms," *Journal of the Korean Physical Society*, vol. 67, pp. 1719–1725, Nov 2015.

[61] M. Lee, J. H. Han, J. H. Kang, M.-S. Kim, and Y. Shin, "Double resonance of raman transitions in a degenerate fermi gas," *Phys. Rev. A*, vol. 95, p. 043627, Apr 2017.

[62] J. Lee, J. H. Lee, J. Noh, and J. Mun, "Core-shell magneto-optical trap for alkaline-earth-metal-like atoms," *Phys. Rev. A*, vol. 91, p. 053405, May 2015.

[63] B. Song, C. He, S. Zhang, E. Hajiyev, W. Huang, X.-J. Liu, and G.-B. Jo, "Spin-orbit-coupled two-electron fermi gases of ytterbium atoms," *Phys. Rev. A*, vol. 94, p. 061604, Dec 2016.

[64] D. Jaksch and P. Zoller, "Creation of effective magnetic fields in optical lattices: the hofstadter butterfly for cold neutral atoms," *New Journal of Physics*, vol. 5, no. 1, p. 56, 2003.

[65] F. Gerbier and J. Dalibard, "Gauge fields for ultracold atoms in optical superlattices," *New Journal of Physics*, vol. 12, no. 3, p. 033007, 2010.

[66] F. Gerbier, N. Goldman, M. Lewenstein, and K. Sengstock, "Non-abelian gauge fields," *Journal of Physics B: Atomic, Molecular and Optical Physics*, vol. 46, no. 13, p. 130201, 2013.

[67] N. Goldman, F. Gerbier, and M. Lewenstein, "Realizing non-abelian gauge potentials in optical square lattices: an application to atomic chern insulators," *Journal of Physics B: Atomic, Molecular and Optical Physics*, vol. 46, no. 13, p. 134010, 2013.

[68] L. Riegger, N. Darkwah Oppong, M. Höfer, D. R. Fernandes, I. Bloch, and S. Fölling, "Localized magnetic moments with tunable spin exchange in a gas of ultracold fermions," *Phys. Rev. Lett.*, vol. 120, p. 143601, Apr 2018.

[69] M. Foss-Feig, M. Hermele, and A. M. Rey, "Probing the kondo lattice model with alkaline-earth-metal atoms," *Phys. Rev. A*, vol. 81, p. 051603, May 2010.

[70] R. Zhang, Y. Cheng, H. Zhai, and P. Zhang, "Orbital feshbach resonance in alkali-earth atoms," *Phys. Rev. Lett.*, vol. 115, p. 135301, Sep 2015.

[71] G. Pagano, M. Mancini, G. Cappellini, L. Livi, C. Sias, J. Catani, M. Inguscio, and L. Fallani, "Strongly interacting gas of two-electron fermions at an orbital feshbach resonance," *Phys. Rev. Lett.*, vol. 115, p. 265301, Dec 2015.

[72] M. Höfer, L. Riegger, F. Scazza, C. Hofrichter, D. R. Fernandes, M. M. Parish, J. Levinsen, I. Bloch, and S. Fölling, "Observation of an orbital interaction-induced feshbach resonance in ^{173}Yb," *Phys. Rev. Lett.*, vol. 115, p. 265302, Dec 2015.

[73] D. Das, S. Barthwal, A. Banerjee, and V. Natarajan, "Absolute frequency measurements in yb with 0.08 ppb uncertainty: Isotope shifts and hyper-

fine structure in the $399-$nm $^1 s_0 \to^1 p_1$ line," *Phys. Rev. A*, vol. 72, p. 032506, Sep 2005.

[74] K. Pandey, A. K. Singh, P. V. K. Kumar, M. V. Suryanarayana, and V. Natarajan, "Isotope shifts and hyperfine structure in the 555.8-nm $^1 S_0 \to {}^3 P_1$ line of yb," *Phys. Rev. A*, vol. 80, p. 022518, Aug 2009.

[75] N. D. Lemke, A. D. Ludlow, Z. W. Barber, T. M. Fortier, S. A. Diddams, Y. Jiang, S. R. Jefferts, T. P. Heavner, T. E. Parker, and C. W. Oates, "Spin-1/2 optical lattice clock," *Phys. Rev. Lett.*, vol. 103, p. 063001, Aug 2009.

[76] N. Poli, Z. W. Barber, N. D. Lemke, C. W. Oates, L. S. Ma, J. E. Stalnaker, T. M. Fortier, S. A. Diddams, L. Hollberg, J. C. Bergquist, A. Brusch, S. Jefferts, T. Heavner, and T. Parker, "Frequency evaluation of the doubly forbidden $^1 S_0 \to^3 P_0$ transition in bosonic ^{174}Yb," *Phys. Rev. A*, vol. 77, p. 050501, May 2008.

[77] C. W. Hoyt, Z. W. Barber, C. W. Oates, T. M. Fortier, S. A. Diddams, and L. Hollberg, "Observation and absolute frequency measurements of the $^1 s_0 -^3 p_0$ optical clock transition in neutral ytterbium," *Phys. Rev. Lett.*, vol. 95, p. 083003, Aug 2005.

[78] C. J. Foot, "Atomic physics," *Oxford university press, ISBN 978-0-19-850696-6*, 2005.

[79] S. L. Campbell, R. B. Hutson, G. E. Marti, A. Goban, N. Darkwah Oppong, R. L. McNally, L. Sonderhouse, J. M. Robinson, W. Zhang, B. J.

Bloom, and J. Ye, "A fermi-degenerate three-dimensional optical lattice clock," *Science*, vol. 358, no. 6359, pp. 90–94, 2017.

[80] B. J. Bloom, T. L. Nicholson, J. R. Williams, S. L. Campbell, M. Bishof, X. Zhang, W. Zhang, S. L. Bromley, and J. Ye, "An optical lattice clock with accuracy and stability at the 10-18 level," *Nature*, vol. 506, p. 71, Jan 2014.

[81] K. Beloy, N. Hinkley, N. B. Phillips, J. A. Sherman, M. Schioppo, J. Lehman, A. Feldman, L. M. Hanssen, C. W. Oates, and A. D. Ludlow, "Atomic clock with 1×10^{-18} room-temperature blackbody stark uncertainty," *Phys. Rev. Lett.*, vol. 113, p. 260801, Dec 2014.

[82] N. Hinkley, J. A. Sherman, N. B. Phillips, M. Schioppo, N. D. Lemke, K. Beloy, M. Pizzocaro, C. W. Oates, and A. D. Ludlow, "An atomic clock with 10–18 instability," *Science*, vol. 341, no. 6151, pp. 1215–1218, 2013.

[83] Y. Takasu, K. Komori, K. Honda, M. Kumakura, T. Yabuzaki, and Y. Takahashi, "Photoassociation spectroscopy of laser-cooled ytterbium atoms," *Phys. Rev. Lett.*, vol. 93, p. 123202, Sep 2004.

[84] S. G. Porsev and A. Derevianko, "Hyperfine quenching of the metastable $^3p_{0,2}$ states in divalent atoms," *Phys. Rev. A*, vol. 69, p. 042506, Apr 2004.

[85] S.-K. Yip and T.-L. Ho, "Zero sound modes of dilute fermi gases with arbitrary spin," *Phys. Rev. A*, vol. 59, pp. 4653–4656, Jun 1999.

[86] M. A. Cazalilla and A. M. Rey, "Ultracold fermi gases with emergent su(n)

symmetry," *Reports on Progress in Physics*, vol. 77, no. 12, p. 124401, 2014.

[87] M. Kitagawa, K. Enomoto, K. Kasa, Y. Takahashi, R. Ciuryło, P. Naidon, and P. S. Julienne, "Two-color photoassociation spectroscopy of ytterbium atoms and the precise determinations of *s*-wave scattering lengths," *Phys. Rev. A*, vol. 77, p. 012719, Jan 2008.

[88] M. A. Cazalilla, A. F. Ho, and M. Ueda, "Ultracold gases of ytterbium: ferromagnetism and mott states in an su(6) fermi system," *New Journal of Physics*, vol. 11, no. 10, p. 103033, 2009.

[89] L. He, M. Jin, and P. Zhuang, "Superfluidity in a three-flavor fermi gas with SU(3) symmetry," *Phys. Rev. A*, vol. 74, p. 033604, Sep 2006.

[90] A. Rapp, G. Zaránd, C. Honerkamp, and W. Hofstetter, "Color superfluidity and "baryon" formation in ultracold fermions," *Phys. Rev. Lett.*, vol. 98, p. 160405, Apr 2007.

[91] T. Ozawa and G. Baym, "Population imbalance and pairing in the bcs-bec crossover of three-component ultracold fermions," *Phys. Rev. A*, vol. 82, p. 063615, Dec 2010.

[92] F. K. Fatemi, K. M. Jones, and P. D. Lett, "Observation of optically induced feshbach resonances in collisions of cold atoms," *Phys. Rev. Lett.*, vol. 85, pp. 4462–4465, Nov 2000.

[93] M. Theis, G. Thalhammer, K. Winkler, M. Hellwig, G. Ruff, R. Grimm, and J. H. Denschlag, "Tuning the scattering length with an optically induced feshbach resonance," *Phys. Rev. Lett.*, vol. 93, p. 123001, Sep 2004.

[94] R. Ciuryło, E. Tiesinga, and P. S. Julienne, "Optical tuning of the scattering length of cold alkaline-earth-metal atoms," *Phys. Rev. A*, vol. 71, p. 030701, Mar 2005.

[95] K. Enomoto, K. Kasa, M. Kitagawa, and Y. Takahashi, "Optical feshbach resonance using the intercombination transition," *Phys. Rev. Lett.*, vol. 101, p. 203201, Nov 2008.

[96] R. Yamazaki, S. Taie, S. Sugawa, and Y. Takahashi, "Submicron spatial modulation of an interatomic interaction in a bose-einstein condensate," *Phys. Rev. Lett.*, vol. 105, p. 050405, Jul 2010.

[97] M. Yan, B. J. DeSalvo, B. Ramachandhran, H. Pu, and T. C. Killian, "Controlling condensate collapse and expansion with an optical feshbach resonance," *Phys. Rev. Lett.*, vol. 110, p. 123201, Mar 2013.

[98] C. J. Hawthorn, K. P. Weber, and R. E. Scholten, "Littrow configuration tunable external cavity diode laser with fixed direction output beam," *Review of Scientific Instruments*, vol. 72, no. 12, pp. 4477–4479, 2001.

[99] M. Lee, "Double resonance of raman transitions in a two-electron degenerate fermi gas of ytterbium atoms," *Ph.D. Thesis, Seoul National University*, Aug 2017.

[100] M. Ł ącki, M. A. Baranov, H. Pichler, and P. Zoller, "Nanoscale "dark state" optical potentials for cold atoms," *Phys. Rev. Lett.*, vol. 117, p. 233001, Nov 2016.

[101] Y. Wang, S. Subhankar, P. Bienias, M. Łącki, T.-C. Tsui, M. A. Baranov, A. V. Gorshkov, P. Zoller, J. V. Porto, and S. L. Rolston, "Dark state

optical lattice with a subwavelength spatial structure," *Phys. Rev. Lett.*, vol. 120, p. 083601, Feb 2018.

[102] J. Heinze, S. Götze, J. S. Krauser, B. Hundt, N. Fläschner, D.-S. Lühmann, C. Becker, and K. Sengstock, "Multiband spectroscopy of ultracold fermions: Observation of reduced tunneling in attractive bose-fermi mixtures," *Phys. Rev. Lett.*, vol. 107, p. 135303, Sep 2011.

[103] R. Wei and E. J. Mueller, "Magnetic-field dependence of raman coupling in alkali-metal atoms," *Phys. Rev. A*, vol. 87, p. 042514, Apr 2013.

[104] A. Aspect, E. Arimondo, R. Kaiser, N. Vansteenkiste, and C. Cohen-Tannoudji, "Laser cooling below the one-photon recoil energy by velocity-selective coherent population trapping," *Phys. Rev. Lett.*, vol. 61, pp. 826–829, Aug 1988.

[105] D. Boiron, C. Triché, D. R. Meacher, P. Verkerk, and G. Grynberg, "Three-dimensional cooling of cesium atoms in four-beam gray optical molasses," *Phys. Rev. A*, vol. 52, pp. R3425–R3428, Nov 1995.

[106] D. Nath, R. K. Easwaran, G. Rajalakshmi, and C. S. Unnikrishnan, "Quantum-interference-enhanced deep sub-doppler cooling of ^{39}k atoms in gray molasses," *Phys. Rev. A*, vol. 88, p. 053407, Nov 2013.

[107] F. Sievers, N. Kretzschmar, D. R. Fernandes, D. Suchet, M. Rabinovic, S. Wu, C. V. Parker, L. Khaykovich, C. Salomon, and F. Chevy, "Simultaneous sub-doppler laser cooling of fermionic ^{6}Li and ^{40}K on the D_1 line: Theory and experiment," *Phys. Rev. A*, vol. 91, p. 023426, Feb 2015.

[108] S. P. Tewari and G. S. Agarwal, "Control of phase matching and nonlinear generation in dense media by resonant fields," *Phys. Rev. Lett.*, vol. 56, pp. 1811–1814, Apr 1986.

[109] S. E. Harris, J. E. Field, and A. Imamoğlu, "Nonlinear optical processes using electromagnetically induced transparency," *Phys. Rev. Lett.*, vol. 64, pp. 1107–1110, Mar 1990.

[110] G. Morigi, J. Eschner, and C. H. Keitel, "Ground state laser cooling using electromagnetically induced transparency," *Phys. Rev. Lett.*, vol. 85, pp. 4458–4461, Nov 2000.

[111] E. Haller, J. Hudson, A. Kelly, D. A. Cotta, B. Peaudecerf, G. D. Bruce, and S. Kuhr, "Single-atom imaging of fermions in a quantum-gas microscope," *Nature Physics*, vol. 11, p. 738, Jul 2015.

[112] D. Budker, D. F. Kimball, S. M. Rochester, and V. V. Yashchuk, "Nonlinear magneto-optics and reduced group velocity of light in atomic vapor with slow ground state relaxation," *Phys. Rev. Lett.*, vol. 83, pp. 1767–1770, Aug 1999.

[113] M. Bajcsy, A. S. Zibrov, and M. D. Lukin, "Stationary pulses of light in an atomic medium," *Nature*, vol. 426, p. 638, Dec 2003.

[114] L. V. Hau, S. E. Harris, Z. Dutton, and C. H. Behroozi, "Light speed reduction to 17 metres per second in an ultracold atomic gas," *Nature*, vol. 397, p. 594, Feb 1999.

[115] K. Bergmann, N. V. Vitanov, and B. W. Shore, "Perspective: Stimulated

raman adiabatic passage: The status after 25 years," *The Journal of Chemical Physics*, vol. 142, no. 17, p. 170901, 2015.

[116] N. V. Vitanov, A. A. Rangelov, B. W. Shore, and K. Bergmann, "Stimulated raman adiabatic passage in physics, chemistry, and beyond," *Rev. Mod. Phys.*, vol. 89, p. 015006, Mar 2017.

[117] A. V. Gorshkov, L. Jiang, M. Greiner, P. Zoller, and M. D. Lukin, "Coherent quantum optical control with subwavelength resolution," *Phys. Rev. Lett.*, vol. 100, p. 093005, Mar 2008.

[118] Y.-J. Lin, R. L. Compton, A. R. Perry, W. D. Phillips, J. V. Porto, and I. B. Spielman, "Bose-einstein condensate in a uniform light-induced vector potential," *Phys. Rev. Lett.*, vol. 102, p. 130401, Mar 2009.

[119] Y.-J. Lin, R. L. Compton, K. Jiménez-García, W. D. Phillips, J. V. Porto, and I. B. Spielman, "A synthetic electric force acting on neutral atoms," *Nature Physics*, vol. 7, p. 531, Mar 2011.

[120] Y.-J. Lin, R. L. Compton, K. Jiménez-García, J. V. Porto, and I. B. Spielman, "Synthetic magnetic fields for ultracold neutral atoms," *Nature*, vol. 462, p. 628, Dec 2009.

[121] V. Galitski and I. B. Spielman, "Spin-orbit coupling in quantum gases," *Nature*, vol. 494, p. 49, Feb 2013.

[122] M. Mancini, "Quantum simulation with ytterbium atoms in synthetic dimensions," *Ph.D. Thesis, University of Firenze*, Aug 2016.

[123] S. H. Autler and C. H. Townes, "Stark effect in rapidly varying fields," *Phys. Rev.*, vol. 100, pp. 703–722, Oct 1955.

[124] K. Jiménez-García, L. J. LeBlanc, R. A. Williams, M. C. Beeler, A. R. Perry, and I. B. Spielman, "Peierls substitution in an engineered lattice potential," *Phys. Rev. Lett.*, vol. 108, p. 225303, May 2012.

[125] P. Wang, Z.-Q. Yu, Z. Fu, J. Miao, L. Huang, S. Chai, H. Zhai, and J. Zhang, "Spin-orbit coupled degenerate fermi gases," *Phys. Rev. Lett.*, vol. 109, p. 095301, Aug 2012.

[126] L. W. Cheuk, A. T. Sommer, Z. Hadzibabic, T. Yefsah, W. S. Bakr, and M. W. Zwierlein, "Spin-injection spectroscopy of a spin-orbit coupled fermi gas," *Phys. Rev. Lett.*, vol. 109, p. 095302, Aug 2012.

[127] N. Q. Burdick, Y. Tang, and B. L. Lev, "Long-lived spin-orbit-coupled degenerate dipolar fermi gas," *Phys. Rev. X*, vol. 6, p. 031022, Aug 2016.

[128] M. Mancini, G. Pagano, G. Cappellini, L. Livi, M. Rider, J. Catani, C. Sias, P. Zoller, M. Inguscio, M. Dalmonte, and L. Fallani, "Observation of chiral edge states with neutral fermions in synthetic hall ribbons," *Science*, vol. 349, no. 6255, pp. 1510–1513, 2015.

[129] G. Veeravalli, E. Kuhnle, P. Dyke, and C. J. Vale, "Bragg spectroscopy of a strongly interacting fermi gas," *Phys. Rev. Lett.*, vol. 101, p. 250403, Dec 2008.

[130] B.-Z. Wang, Y.-H. Lu, W. Sun, S. Chen, Y. Deng, and X.-J. Liu, "Dirac-, rashba-, and weyl-type spin-orbit couplings: Toward experimental realization in ultracold atoms," *Phys. Rev. A*, vol. 97, p. 011605, Jan 2018.

[131] Z. Wu, L. Zhang, W. Sun, X.-T. Xu, B.-Z. Wang, S.-C. Ji, Y. Deng, S. Chen, X.-J. Liu, and J.-W. Pan, "Realization of two-dimensional spin-

orbit coupling for bose-einstein condensates," *Science*, vol. 354, no. 6308, pp. 83–88, 2016.

[132] W. Sun, B.-Z. Wang, X.-T. Xu, C.-R. Yi, L. Zhang, Z. Wu, Y. Deng, X.-J. Liu, S. Chen, and J.-W. Pan, "Highly controllable and robust 2d spin-orbit coupling for quantum gases," *Phys. Rev. Lett.*, vol. 121, p. 150401, Oct 2018.

[133] K. v. Klitzing, G. Dorda, and M. Pepper, "New method for high-accuracy determination of the fine-structure constant based on quantized hall resistance," *Phys. Rev. Lett.*, vol. 45, pp. 494–497, Aug 1980.

[134] R. B. Laughlin, "Quantized hall conductivity in two dimensions," *Phys. Rev. B*, vol. 23, pp. 5632–5633, May 1981.

[135] J. Avron, "A topological look at the quantum hall effect," *Physics Today*, vol. 56, p. 38, Aug 2003.

[136] D. R. Hofstadter, "Energy levels and wave functions of bloch electrons in rational and irrational magnetic fields," *Phys. Rev. B*, vol. 14, pp. 2239–2249, Sep 1976.

[137] M. Aidelsburger, "Artificial gauge fields with ultracold atoms in optical lattices," *Springer, ISBN 978-3-319-25829-4*, 2016.

[138] C. R. Dean, L. Wang, P. Maher, C. Forsythe, F. Ghahari, Y. Gao, J. Katoch, M. Ishigami, P. Moon, M. Koshino, T. Taniguchi, K. Watanabe, K. L. Shepard, J. Hone, and P. Kim, "Hofstadter's butterfly and the fractal quantum hall effect in moiré superlattices," *Nature*, vol. 497, p. 598, May 2013.

162

[139] M. Aidelsburger, M. Atala, M. Lohse, J. T. Barreiro, B. Paredes, and I. Bloch, "Realization of the hofstadter hamiltonian with ultracold atoms in optical lattices," *Phys. Rev. Lett.*, vol. 111, p. 185301, Oct 2013.

[140] D. J. Thouless, M. Kohmoto, M. P. Nightingale, and M. den Nijs, "Quantized hall conductance in a two-dimensional periodic potential," *Phys. Rev. Lett.*, vol. 49, pp. 405–408, Aug 1982.

[141] O. Boada, A. Celi, J. I. Latorre, and M. Lewenstein, "Quantum simulation of an extra dimension," *Phys. Rev. Lett.*, vol. 108, p. 133001, Mar 2012.

[142] A. Celi, P. Massignan, J. Ruseckas, N. Goldman, I. B. Spielman, G. Juzeliūnas, and M. Lewenstein, "Synthetic gauge fields in synthetic dimensions," *Phys. Rev. Lett.*, vol. 112, p. 043001, Jan 2014.

[143] B. K. Stuhl, H.-I. Lu, L. M. Aycock, D. Genkina, and I. B. Spielman, "Visualizing edge states with an atomic bose gas in the quantum hall regime," *Science*, vol. 349, no. 6255, pp. 1514–1518, 2015.

[144] H. Miyake, G. A. Siviloglou, C. J. Kennedy, W. C. Burton, and W. Ketterle, "Realizing the harper hamiltonian with laser-assisted tunneling in optical lattices," *Phys. Rev. Lett.*, vol. 111, p. 185302, Oct 2013.

[145] M. Aidelsburger, M. Atala, S. Nascimbène, S. Trotzky, Y.-A. Chen, and I. Bloch, "Experimental realization of strong effective magnetic fields in an optical lattice," *Phys. Rev. Lett.*, vol. 107, p. 255301, Dec 2011.

[146] M. Atala, M. Aidelsburger, M. Lohse, J. T. Barreiro, B. Paredes, and I. Bloch, "Observation of chiral currents with ultracold atoms in bosonic ladders," *Nature Physics*, vol. 10, p. 588, Jul 2014.

[147] M. Aidelsburger, M. Lohse, C. Schweizer, M. Atala, J. . T. Barreiro, S. Nascimbène, N. . R. Cooper, I. Bloch, and N. Goldman, "Measuring the chern number of hofstadter bands with ultracold bosonic atoms," *Nature Physics*, vol. 11, p. 162, Dec 2014.

[148] L. F. Livi, G. Cappellini, M. Diem, L. Franchi, C. Clivati, M. Frittelli, F. Levi, D. Calonico, J. Catani, M. Inguscio, and L. Fallani, "Synthetic dimensions and spin-orbit coupling with an optical clock transition," *Phys. Rev. Lett.*, vol. 117, p. 220401, Nov 2016.

[149] E. J. Meier, F. A. An, and B. Gadway, "Observation of the topological soliton state in the su-schrieffer-heeger model," *Nat. Commun.*, vol. 7, p. 13986, Dec 2016.

[150] F. A. An, E. J. Meier, and B. Gadway, "Direct observation of chiral currents and magnetic reflection in atomic flux lattices," *Sci. Adv.*, vol. 3, no. 4, p. e1602685, 2017.

[151] F. A. An, E. J. Meier, and B. Gadway, "Diffusive and arrested transport of atoms under tailored disorder," *Nat. Commun.*, vol. 8, no. 1, p. 325, 2017.

[152] J. H. Kang, J. H. Han, and Y. Shin, "Realization of a cross-linked chiral ladder with neutral fermions in a 1d optical lattice by orbital-momentum coupling," *Phys. Rev. Lett.*, vol. 121, p. 150403, Oct 2018.

[153] O. Boada, A. Celi, J. Rodríguez-Laguna, J. I. Latorre, and M. Lewenstein, "Quantum simulation of non-trivial topology," *New J. Phys.*, vol. 17, no. 4, p. 045007, 2015.

[154] S. Barbarino, M. Dalmonte, R. Fazio, and G. E. Santoro, "Topological phases in frustrated synthetic ladders with an odd number of legs," *Phys. Rev. A*, vol. 97, p. 013634, Jan 2018.

[155] T.-S. Zeng, C. Wang, and H. Zhai, "Charge pumping of interacting fermion atoms in the synthetic dimension," *Phys. Rev. Lett.*, vol. 115, p. 095302, Aug 2015.

[156] L. Taddia, E. Cornfeld, D. Rossini, L. Mazza, E. Sela, and R. Fazio, "Topological fractional pumping with alkaline-earth-like atoms in synthetic lattices," *Phys. Rev. Lett.*, vol. 118, p. 230402, Jun 2017.

[157] M. Köhl, H. Moritz, T. Stöferle, K. Günter, and T. Esslinger, "Fermionic atoms in a three dimensional optical lattice: Observing fermi surfaces, dynamics, and interactions," *Phys. Rev. Lett.*, vol. 94, p. 080403, Mar 2005.

[158] B. Song, L. Zhang, C. He, T. F. J. Poon, E. Hajiyev, S. Zhang, X.-J. Liu, and G.-B. Jo, "Observation of symmetry-protected topological band with ultracold fermions," *Sci. Adv.*, vol. 4, no. 2, p. eaao4748, 2018.

[159] H. L. Nourse, I. P. McCulloch, C. Janani, and B. J. Powell, "Haldane insulator protected by reflection symmetry in the doped hubbard model on the three-legged ladder," *Phys. Rev. B*, vol. 94, p. 214418, Dec 2016.

[160] J. Zak, "Berry's phase for energy bands in solids," *Phys. Rev. Lett.*, vol. 62, pp. 2747–2750, Jun 1989.

[161] A. Altland and M. R. Zirnbauer, "Nonstandard symmetry classes in meso-

scopic normal-superconducting hybrid structures," *Phys. Rev. B*, vol. 55, pp. 1142–1161, Jan 1997.

[162] C.-K. Chiu, J. C. Y. Teo, A. P. Schnyder, and S. Ryu, "Classification of topological quantum matter with symmetries," *Rev. Mod. Phys.*, vol. 88, p. 035005, Aug 2016.

[163] A. P. Schnyder, S. Ryu, A. Furusaki, and A. W. W. Ludwig, "Classification of topological insulators and superconductors in three spatial dimensions," *Phys. Rev. B*, vol. 78, p. 195125, Nov 2008.

[164] A. Valdés-Curiel, D. Trypogeorgos, E. E. Marshall, and I. B. Spielman, "Fourier transform spectroscopy of a spin–orbit coupled bose gas," *New Journal of Physics*, vol. 19, no. 3, p. 033025, 2017.

[165] M. Ezawa, Y. Tanaka, and N. Nagaosa, "Topological phase transition without gap closing," *Sci. Rep.*, vol. 3, p. 2790, Sep 2013.

[166] E. J. Meier, F. A. An, A. Dauphin, M. Maffei, P. Massignan, T. L. Hughes, and B. Gadway, "Observation of the topological anderson insulator in disordered atomic wires," *Science*, 2018.

[167] F. A. An, E. J. Meier, and B. Gadway, "Engineering a flux-dependent mobility edge in disordered zigzag chains," *Phys. Rev. X*, vol. 8, p. 031045, Aug 2018.

[168] F. A. An, E. J. Meier, J. Ang'ong'a, and B. Gadway, "Correlated dynamics in a synthetic lattice of momentum states," *Phys. Rev. Lett.*, vol. 120, p. 040407, Jan 2018.

[169] E. Anisimovas, M. Račiūnas, C. Sträter, A. Eckardt, I. B. Spielman, and G. Juzeliūnas, "Semisynthetic zigzag optical lattice for ultracold bosons," *Phys. Rev. A*, vol. 94, p. 063632, Dec 2016.

[170] S. Barbarino, L. Taddia, D. Rossini, L. Mazza, and R. Fazio, "Magnetic crystals and helical liquids in alkaline-earth fermionic gases," *Nat. Commun.*, vol. 6, p. 8134, Sep 2015.

[171] K. M. Jones, E. Tiesinga, P. D. Lett, and P. S. Julienne, "Ultracold photoassociation spectroscopy: Long-range molecules and atomic scattering," *Rev. Mod. Phys.*, vol. 78, pp. 483–535, May 2006.

[172] G. B. Partridge, K. E. Strecker, R. I. Kamar, M. W. Jack, and R. G. Hulet, "Molecular probe of pairing in the bec-bcs crossover," *Phys. Rev. Lett.*, vol. 95, p. 020404, Jul 2005.

[173] S. Tojo, M. Kitagawa, K. Enomoto, Y. Kato, Y. Takasu, M. Kumakura, and Y. Takahashi, "High-resolution photoassociation spectroscopy of ultracold ytterbium atoms by using the intercombination transition," *Phys. Rev. Lett.*, vol. 96, p. 153201, Apr 2006.

[174] K. Enomoto, M. Kitagawa, K. Kasa, S. Tojo, and Y. Takahashi, "Determination of the s-wave scattering length and the C_6 van der waals coefficient of ^{174}Yb via photoassociation spectroscopy," *Phys. Rev. Lett.*, vol. 98, p. 203201, May 2007.

[175] M. Borkowski, R. Ciuryło, P. S. Julienne, S. Tojo, K. Enomoto, and Y. Takahashi, "Line shapes of optical feshbach resonances near the in-

tercombination transition of bosonic ytterbium," *Phys. Rev. A*, vol. 80, p. 012715, Jul 2009.

[176] M. Borkowski, R. Ciuryło, P. S. Julienne, R. Yamazaki, H. Hara, K. Enomoto, S. Taie, S. Sugawa, Y. Takasu, and Y. Takahashi, "Photoassociative production of ultracold heteronuclear ytterbium molecules," *Phys. Rev. A*, vol. 84, p. 030702, Sep 2011.

[177] R. Roy, R. Shrestha, A. Green, S. Gupta, M. Li, S. Kotochigova, A. Petrov, and C. H. Yuen, "Photoassociative production of ultracold heteronuclear ybli* molecules," *Phys. Rev. A*, vol. 94, p. 033413, Sep 2016.

[178] S. B. Nagel, P. G. Mickelson, A. D. Saenz, Y. N. Martinez, Y. C. Chen, T. C. Killian, P. Pellegrini, and R. Côté, "Photoassociative spectroscopy at long range in ultracold strontium," *Phys. Rev. Lett.*, vol. 94, p. 083004, Mar 2005.

[179] T. Zelevinsky, M. M. Boyd, A. D. Ludlow, T. Ido, J. Ye, R. Ciuryło, P. Naidon, and P. S. Julienne, "Narrow line photoassociation in an optical lattice," *Phys. Rev. Lett.*, vol. 96, p. 203201, May 2006.

[180] M. Borkowski, P. Morzyński, R. Ciuryło, P. S. Julienne, M. Yan, B. J. DeSalvo, and T. C. Killian, "Mass scaling and nonadiabatic effects in photoassociation spectroscopy of ultracold strontium atoms," *Phys. Rev. A*, vol. 90, p. 032713, Sep 2014.

[181] S. Stellmer, B. Pasquiou, R. Grimm, and F. Schreck, "Creation of ultracold sr_2 molecules in the electronic ground state," *Phys. Rev. Lett.*, vol. 109, p. 115302, Sep 2012.

[182] G. Reinaudi, C. B. Osborn, M. McDonald, S. Kotochigova, and T. Zelevinsky, "Optical production of stable ultracold $^{88}Sr_2$ molecules," *Phys. Rev. Lett.*, vol. 109, p. 115303, Sep 2012.

[183] T. L. Nicholson, S. Blatt, B. J. Bloom, J. R. Williams, J. W. Thomsen, J. Ye, and P. S. Julienne, "Optical feshbach resonances: Field-dressed theory and comparison with experiments," *Phys. Rev. A*, vol. 92, p. 022709, Aug 2015.

[184] M. Kahmann, E. Tiemann, O. Appel, U. Sterr, and F. Riehle, "Photoassociation spectroscopy of ^{40}Ca measured with kilohertz accuracy near the $^3P_1 + {}^1S_0$ asymptote and its zeeman effect," *Phys. Rev. A*, vol. 89, p. 023413, Feb 2014.

[185] E. Tiemann, M. Kahmann, E. Pachomow, F. Riehle, and U. Sterr, "Nonlinear zeeman effect in photoassociation spectra of ^{40}Ca near the $^3p_1 + {}^1s_0$ asymptote," *Phys. Rev. A*, vol. 92, p. 023419, Aug 2015.

[186] S. Taie, R. Yamazaki, S. Sugawa, and Y. Takahashi, "An su(6) mott insulator of an atomic fermi gas realized by large-spin pomeranchuk cooling," *Nature Physics*, vol. 8, p. 825, Sep 2012.

[187] I. Reichenbach, P. S. Julienne, and I. H. Deutsch, "Controlling nuclear spin exchange via optical feshbach resonances in ^{171}Yb," *Phys. Rev. A*, vol. 80, p. 020701, Aug 2009.

[188] J. P. Pique, F. Hartmann, R. Bacis, S. Churassy, and J. B. Koffend, "Hyperfine-induced ungerade-gerade symmetry breaking in a homonuclear

diatomic molecule near a dissociation limit: $^{127}I_2$ at the $^2p_{\frac{3}{2}} -^2 p_{\frac{1}{2}}$ limit," *Phys. Rev. Lett.*, vol. 52, pp. 267–270, Jan 1984.

[189] E. Tiesinga, K. M. Jones, P. D. Lett, U. Volz, C. J. Williams, and P. S. Julienne, "Measurement and modeling of hyperfine- and rotation-induced state mixing in large weakly bound sodium dimers," *Phys. Rev. A*, vol. 71, p. 052703, May 2005.

[190] E. Tiesinga, C. J. Williams, and P. S. Julienne, "Photoassociative spectroscopy of highly excited vibrational levels of alkali-metal dimers: Greenfunction approach for eigenvalue solvers," *Phys. Rev. A*, vol. 57, pp. 4257–4267, Jun 1998.

[191] R. J. LeRoy and R. B. Bernstein, "Dissociation energy and long-range potential of diatomic molecules from vibrational spacings of higher levels," *J. Chem. Phys.*, vol. 52, no. 8, pp. 3869–3879, 1970.

[192] R. Ciuryło, E. Tiesinga, S. Kotochigova, and P. S. Julienne, "Photoassociation spectroscopy of cold alkaline-earth-metal atoms near the intercombination line," *Phys. Rev. A*, vol. 70, p. 062710, Dec 2004.

[193] C. D. Hamley, E. M. Bookjans, G. Behin-Aein, P. Ahmadi, and M. S. Chapman, "Photoassociation spectroscopy of a spin-1 bose-einstein condensate," *Phys. Rev. A*, vol. 79, p. 023401, Feb 2009.

[194] J. L. Bohn and P. S. Julienne, "Semianalytic theory of laser-assisted resonant cold collisions," *Phys. Rev. A*, vol. 60, pp. 414–425, Jul 1999.

[195] M.-S. Kim, J. Lee, J. H. Lee, Y. Shin, and J. Mun, "Measurements of opti-

cal feshbach resonances of ^{174}Yb atoms," *Phys. Rev. A*, vol. 94, p. 042703, Oct 2016.

[196] N. Nemitz, T. Ohkubo, M. Takamoto, I. Ushijima, M. Das, N. Ohmae, and H. Katori, "Frequency ratio of yb and sr clocks with 5×10^{-17} uncertainty at 150 seconds averaging time," *Nature Photonics*, vol. 10, p. 258, Feb 2016.

[197] C. Hofrichter, L. Riegger, F. Scazza, M. Höfer, D. R. Fernandes, I. Bloch, and S. Fölling, "Direct probing of the mott crossover in the SU(n) fermi-hubbard model," *Phys. Rev. X*, vol. 6, p. 021030, Jun 2016.

[198] M.-s. Kim, "Generation of degenerate quantum gases of ytterbium atoms," *Ph.D. Thesis, Seoul National University*, Aug 2016.

Appendix A

Clebsch-Gordan coefficients of ^{173}Yb nuclear spins

This Appendix shows the calculated amplitude of normalized Clebsch-Gordan coefficients (line strengths) $|C_{F',m_F}(\epsilon)|^2\alpha_{JJ'}$ of ^{173}Yb nuclear spins.
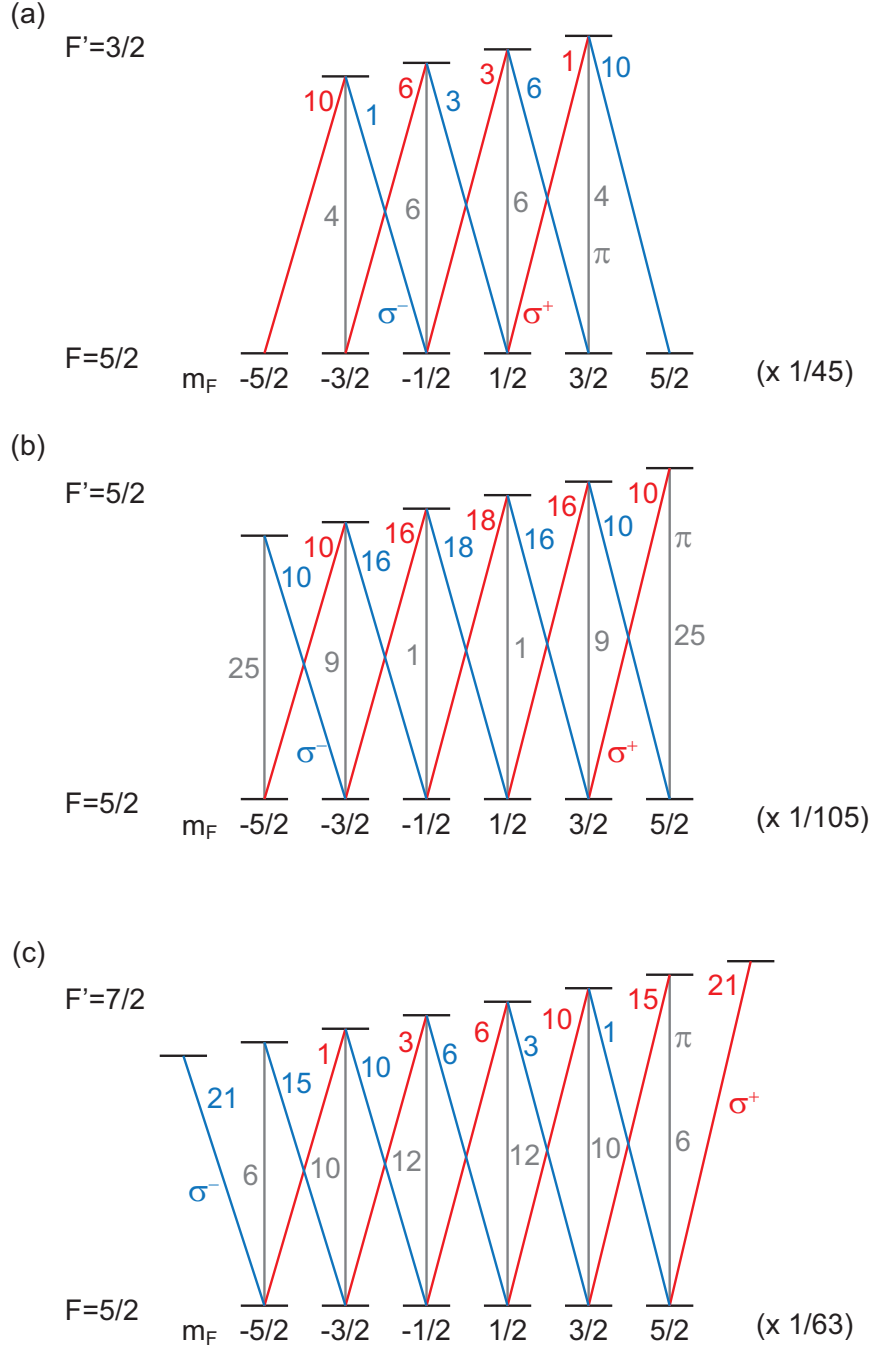
Figure A.1: Line strengths $|C_{F',m_F}(\epsilon)|^2\alpha_{JJ'}$ of ytterbium fermions between different hyperfine spin states for $^1S_0 \to {}^1P_1$ and $^1S_0 \to {}^3P_1$ transitions.

Appendix B

Electronic Circuits

This Appendix contains information of basic electronic circuits frequently used in ultracold atom experiments.
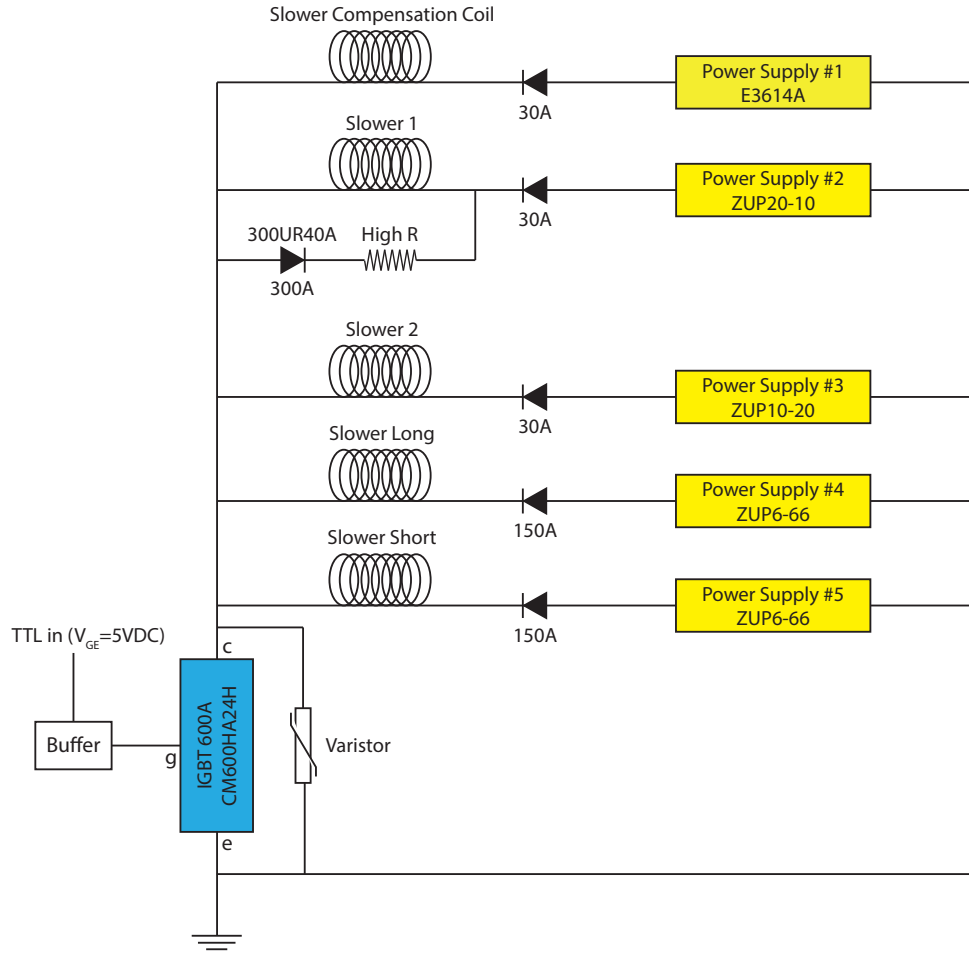
Figure B.1: Schematic diagram for an IGBT coil switching system. A varistor and a high-power resistor absorb eddy currents ringing after the abrupt switching off ($\ll 100~\mu s$) the magnetic field. The IGBT systems for the MOT coils and science chamber coils are similarly constructed.
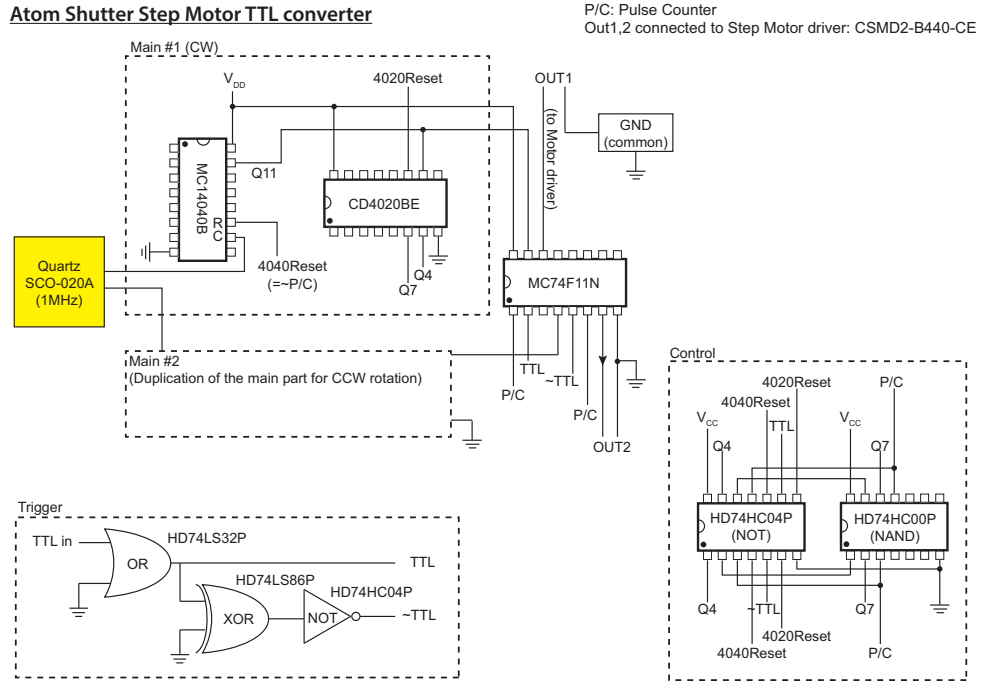
Figure B.2: Schematic diagram for a pulse generator operating an atom shutter. The pulse generator is based on the typical counter circuit of flip-flops. When the trigger pulse (TTL) rises, the circuit emits a set of pulses driving the atom shutter clockwise direction. The circuit also discharges another set of pulses driving the atom shutter counter-clockwise manner if the TTL signal drops to zero. Since the atom shutter rotates by $1.8°$ per a pulse, one requires at least 50 pulses to rotate the atom shutter by $90°$.
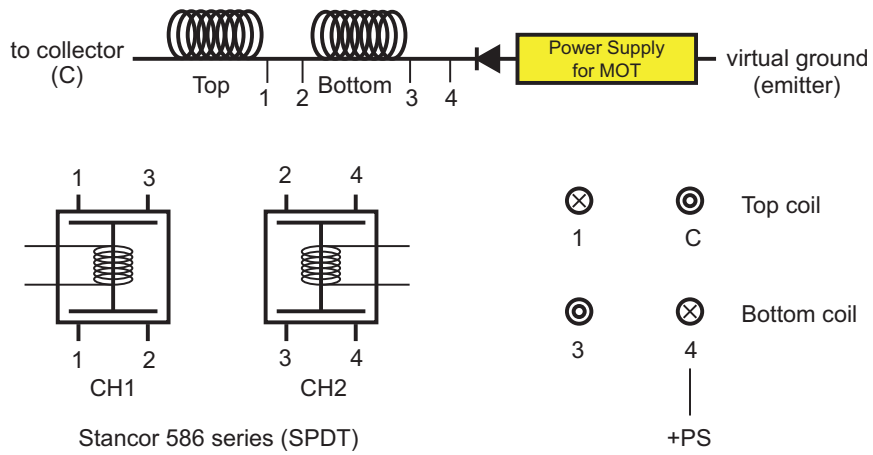
Figure B.3: Schematic diagram for a relay system which swaps MOT coil from anti-Helmholtz to Helmholtz configuration. The system is made of mechanical relays, switching the coil configuration within ≈ 200 ms.

Appendix C

How to align a SHG cavity

This Appendix explains how to align a bow-tie type cavity for the second harmonic generation. The basic idea is to find an alignment which makes best conversion efficiency performance, and then finish the cavity unit by small tweaks. The tips and procedures for aligning the cavity are given below:

1) Find an optimal set of lens pair which creates sufficient beam parameters (especially the beam waist, ω_0) at the position of the crystal, as designed. For blue cavity, $\omega_0 \approx 35.2\ \mu m$ and for green cavity, $\omega_0 \approx 25.9\ \mu m$ are adopted. The folding angle of the cavity is chosen to $8°$. Our optimal parameters are calculated using SNLO program and are summarized in the thesis of M.-S. Kim [198].

2) Place the M_1, M_2, M_3 and the crystal (of course, temperature stabilized) at the designed location. It is useful if one glue the blueprint of the cavity system on the breadboard. Check whether all laser beams are reflected at the center of the mirrors. Place the piezoelectric transducer (PZT) voltage in the middle of the dynamic control range.
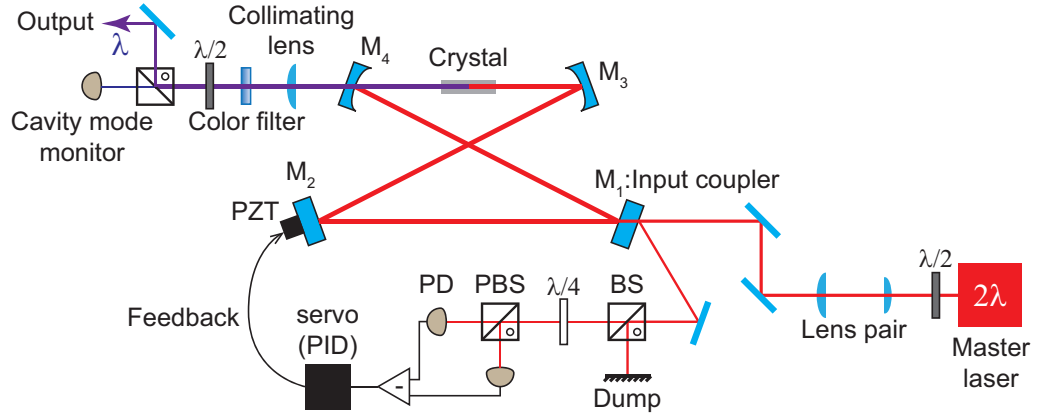
Figure C.1: Schematic drawing of cavity system (second harmonic generator unit) and Hänsch-Couillaud method to lock the cavity length.

3) Empirically find the position of the crystal which gives the best single-path conversion efficiency. Do not get confused with the power incident from the master laser. Placing a color filter or a dichroic mirror is helpful to isolate unwanted lights from the unconverted beam. It is also useful to place a photodiode (PD) to monitor the cavity output power.

4) Carefully locate a pair of iris outside of the cavity system to mark this alignment. Farther the iris, preciser the alignment. If the beam gets spread out, place a suitable collimating lens.

5) Place the last mirror (M_4) to make the beam travels a round trip inside the cavity. When a perfect round trip beam path forms, one can observe a bright spot flickering at the cavity (mirror and output).

6) Tweak the mirrors before the input coupler (M_1) and make the alignment agrees with the iris placed. Then, tweak again the M_4 to form a round trip.

7) Scan the PZT voltage at the rate $80 \sim 100$ Hz and observe the signal from the cavity mode monitor PD.

8) Tweak M_1 and M_4 to make the spatial mode of the output beam as Gaussian 00 mode.

9) The conversion efficiency can be monitored through the cavity mode monitor PD. Tweak M_2 and M_3 to reach the maximum conversion efficiency. When alignment of the cavity changes, the PD may show you the fake signal because of the misalignment to the PD. Do not get confused–Always check the beam goes to the PD correctly.

10) Tweak the position of the crystal if necessary. In my experience, the sequences 9 and 10 are almost unnecessary.

11) Make the cavity air-tight and wait for the temperature stabilization. Place the optics for Hänsch-Couillaud cavity lock.

12) Try cavity lock and monitor the output power stabilization. In my experience, the laser beam may change temperature of the environment, which yields conversion efficiency drop. In this case, tweak the mirrors before the input coupler to find the maximum conversion efficiency when the cavity length is fixed.

The whole sequence is just one-day job, and the typical conversion efficiency reached in this way for a LBO crystal is about $\approx 20\%$.

Appendix D

Numerical Codes for Experimental Parameters

This Appendix contains information on the numerical code for calculating AC Stark shift, Rabi frequencies for the Raman beams, and the real tunneling matrix element in 1D optical lattice.

Default constants

```
(*basic*)
hbar = 1.054 × 10^-34;
h = 6.626 * 10^-34;
kb = 1.38 × 10^-23;
c = 299 792 458;
m0 = 1.66 * 10^-27;
a0 = 5.292 * 10^-11;
elec = 1.60217646 * 10^-19; (*in Coulomb*)
epsilon0 = 8.854187 * 10^-12; (*in F/m*)
(*Ytterbium*)
λYb1 = 555.8 * 10^-9;(*MOT beam*)
λYb2 = 398.9 * 10^-9;(*Slowing beam*)
λYb3 = 507.0 * 10^-9;
λYb4 = 578.0 * 10^-9;
IsatYb1 = 0.1388 (*in mW/cm^2*);
IsatYb2 = 59.97(*in mW/cm^2*);
mYb = 173 m0;
ΓYb1 = 2 π * 0.1824 * 10^6;
ΓYb2 = 2 π * 29.13 * 10^6;
ΓYb3 = 2 π * 15 * 10^-3;
ΓYb4 = 2 π * 10 * 10^-3;
PSD[N_, ω_, T_] := N/6 * (hbar * ω)^3 / (kb * T)^3
(*optical potential*)
Clear[λ];
Pol = (3 π c^2)/(2 ω0^3) Γ/Δ /. {ω0 -> (2 π c)/λ0, Δ -> (2 π c)/λ0 - (2 π c)/λ};
Er = h^2/(2 m λ^2);
grav = 9.8;
u = 10^-6;
μB = 9.27300968 * 10^-24;(* Bohr magneton in SI unit J*T^-1 *)
μI = μB * (9.10938291 * 10^-31)/(1.67262178 * 10^-27);(* Nucleus magneton in SI unit J*T^-1 *)
μB0 = μB / (2 π * hbar * 10^4);(* Bohr magneton in Hz/G *)
μI0 = μB0 * (9.10938291 * 10^-31)/(1.67262178 * 10^-27);(* Nucleus magneton in Hz/G *)
(*gFYb3P1=0.42626;
gFYb3P1*μB0/10^3(*kHz/G Zeeman splitting 3P1*)
*)
gIYb1S0 = 0.6776;
gIYb1S0 * μI0 * 2/5;(*Hz/G Zeeman splitting 1S0*)
gJYb3P1 = 1.493;
```

```
gFYb3P1[F_] := gJYb3P1 * (F (F + 1) - (5/2) ((5/2) + 1) + 1 (1 + 1))/(2 * F (F + 1)) +
    μI0/(μB0 * 5/2) * (F (F + 1) + (5/2) ((5/2) + 1) - 1 (1 + 1))/(2 * F (F + 1))
gFYb3P1[5/2] * μB0/10^3;(*kHz/G Zeeman splitting 3P1*)
gJYb1P1 = 1.035;

gFYb1P1[F_] := gJYb1P1 * (F (F + 1) - (5/2) ((5/2) + 1) + 1 (1 + 1))/(2 * F (F + 1)) +
    μI0/(μB0 * 5/2) * (F (F + 1) + (5/2) ((5/2) + 1) - 1 (1 + 1))/(2 * F (F + 1))
gFYb1P1[5/2] * μB0/10^3;(*kHz/G Zeeman splitting 1P1*)
```

Optical beams

```
Icirc[λ_, P_, bx_, by_, bz_, w0_, x_, y_, z_] :=
  Module[{bpd, nbpd, r, axial, radial, w, U},
    bpd = {bx, by, bz}; (*beam propagation direction*)
    nbpd = bpd / Norm[bpd]; (*normalized beam propagation direction*)
    r = {x, y, z}; (*point of interest*)
    axial = nbpd.r; (*axial distance from center*)
    radial = Norm[Cross[nbpd, r]]; (*transverse distance from center*)
    w = w0 Sqrt[1 + (λ axial/(π w0^2))^2] ;
    U = 2 P/(π w^2) * Exp[-2 (radial)^2/w^2]
  ];
```

183

```
Iellip[λ_, P_, zx_, zy_, zz_, xx_, xy_, xz_, w0_, e_, x_, y_, z_] :=
  Module[{nz, temp, nx, ny, r, axial, xradial, yradial, wx, wy, U},
    nz = {zx, zy, zz} / Sqrt[zx² + zy² + zz²]; (*beam propagation axis*)
    temp = Cross[nz, {xx, xy, xz}];
    ny = temp / Norm[temp]; (*beam minor axis*)
    nx = Cross[ny, nz]; (*beam major axis*)
    r = {x, y, z}; (*point of interest*)
    axial = nz.r;
    xradial = nx.r;
    yradial = ny.r;
```

$$wx = w0 \sqrt{1 + \left(\frac{\lambda \, axial}{\pi \, w0^2}\right)^2} \; ;$$

$$wy = e * w0 \sqrt{1 + \left(\frac{\lambda \, axial}{\pi \, (e * w0)^2}\right)^2} \; ;$$

$$U = \frac{2 \, P}{\pi \, wx * wy} * Exp\left[-2 \left(\frac{xradial^2}{wx^2} + \frac{yradial^2}{wy^2}\right)\right]\Big]$$

```
  ];
(*The dipole potential is given at
 "OPTICAL DIPOLE TRAPS FOR NEUTRAL ATOMS (36)" or "ATOMIC PHYSICS, (9.46)"*)
```

184

Rabi frequency of Raman beams

```
CG[Fe_, mf_, q_] := (-1)^(2*Fe+5/2+mf) Sqrt[3 * (2 * 5 / 2 + 1) * (2 * Fe + 1)] *
    SixJSymbol[{1, 1, 0}, {0, 0, 1}] * SixJSymbol[{1, Fe, 5 / 2}, {5 / 2, 0, 1}] *
    ThreeJSymbol[{5 / 2, mf}, {1, q}, {Fe, - (mf + q)}]];
(* Rabi frequency with δ: fine structure detuning w.r.t F=7/2,
mf: initial spin state, q1&q2: Raman beam polarization *)
ΩR[Bfield_, δ_, mf_, q1_, q2_, I1_, I2_] := 3 π * c^2 * ΓYb1 / (2 (2 π * c / (λYb1))^3) *
    ((-1)^(1+q1+1+q2) * ClebschGordan[{5 / 2, mf}, {1, q1}, {7 / 2, mf + q1}] *
      ClebschGordan[{5 / 2, mf + q1 - q2}, {1, q2}, {7 / 2, mf + q1}] /
      (2 π * (δ * 10^9 - μB0 * gFYb3P1[7 / 2] * Bfield * (mf + q1) +
          μI0 * gIYb1S0 * 2 / 5 * (mf) * Bfield))


      (* Bfield in gauss, detuning in GHz *)
      (* Factor 3 absorbed into ClebschGordan coefficient normalization *)


    + (-1)^(1+q1+1+q2) * ClebschGordan[{5 / 2, mf}, {1, q1}, {5 / 2, mf + q1}] *
     ClebschGordan[{5 / 2, mf + q1 - q2}, {1, q2}, {5 / 2, mf + q1}] /
      (2 π * ((δ - 4.698) * 10^9 - μB0 * gFYb3P1[5 / 2] * Bfield * (mf + q1) +
          μI0 * gIYb1S0 * 2 / 5 * (mf) * Bfield))
    + (-1)^(1+q1+1+q2) * ClebschGordan[{5 / 2, mf}, {1, q1}, {3 / 2, mf + q1}] *
     ClebschGordan[{5 / 2, mf + q1 - q2}, {1, q2}, {3 / 2, mf + q1}] /
      (2 π * ((δ - 6.193) * 10^9 - μB0 * gFYb3P1[3 / 2] * Bfield * (mf + q1) +
          μI0 * gIYb1S0 * 2 / 5 * (mf) * Bfield))
    ) * Sqrt[I1 * I2] / hbar;
(* Raman laser intensities *)
I1 = Iellip[λYb1, 100 * 10^-6, 0, 0, 1, 0, 1, 0, 150 u, 1, 0, 0, 0];
I2 = Iellip[λYb1, 100 * 10^-6, 0, 0, 1, 0, 1, 0, 150 u, 1, 0, 0, 0];
Plot[{ΩR[0, δ, -5 / 2, 1, -1, I1 / 2, I2 / 2] / (2 π),
  ΩR[0, δ, -3 / 2, 1, -1, I1 / 2, I2 / 2] / (2 π), ΩR[0, δ, -1 / 2, 1, -1] / (2 π)},
 {δ, -6, 8}, PlotRange -> {-8 * 10^3, 8 * 10^3}, Frame → True,
 FrameLabel → "ΩR(σ+σ-)/2π (Hz)", ImageSize → Large]
```
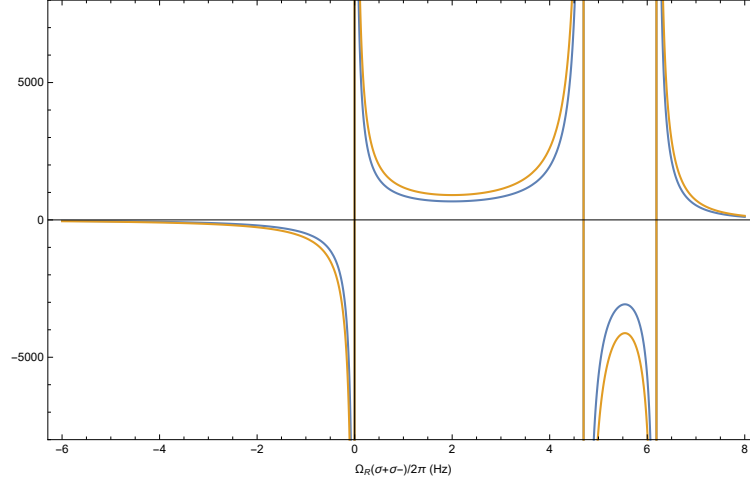
AC Stark shift of Raman beams

```
αpolYb[Bfield_, δ_, mf_, q_] := Module[{Δ1, Δ2, Δ3, Fe, Fg, trs7, trs5, trs3, pot},
  Δ1 = (2 π * δ * 10^9 - 2 π * μB0 * gFYb3P1[7/2] * Bfield * (mf + q) +
     2 π * μI0 * gIYb1S0 * 2/5 * (mf) * Bfield);
  (* detuning of beam, with respect to Fe=7/2 *)
  Δ2 = (2 π * δ * 10^9 - 2 π * μB0 * gFYb3P1[5/2] * Bfield * (mf + q) +
     2 π * μI0 * gIYb1S0 * 2/5 * (mf) * Bfield - 2 π * 4698/u);
  (* detuning of beam, with respect to Fe=5/2 *)
  Δ3 = (2 π * δ * 10^9 - 2 π * μB0 * gFYb3P1[3/2] * Bfield * (mf + q) +
     2 π * μI0 * gIYb1S0 * 2/5 * (mf) * Bfield - 2 π * 6193/u);
  (* detuning of beam, with respect to Fe=3/2 *)

  Fg = 5/2;
  (* transition strength *)
  Fe = 7/2;
  trs7 = 3 * (2 * Fg + 1) * (2 * Fe + 1) *
    (SixJSymbol[{1, 1, 0}, {0, 0, 1}])^2 * (SixJSymbol[{1, Fe, 5/2}, {Fg, 0, 1}])^2
    (ThreeJSymbol[{Fg, mf}, {1, q}, {Fe, -(mf + q)}])^2;
  Fe = 5/2;
  trs5 = 3 * (2 * Fg + 1) * (2 * Fe + 1) *
    (SixJSymbol[{1, 1, 0}, {0, 0, 1}])^2 * (SixJSymbol[{1, Fe, 5/2}, {Fg, 0, 1}])^2
    (ThreeJSymbol[{Fg, mf}, {1, q}, {Fe, -(mf + q)}])^2;
  Fe = 3/2;
  trs3 = 3 * (2 * Fg + 1) * (2 * Fe + 1) *
    (SixJSymbol[{1, 1, 0}, {0, 0, 1}])^2 * (SixJSymbol[{1, Fe, 5/2}, {Fg, 0, 1}])^2
```

```mathematica
      (ThreeJSymbol[{Fg, mf}, {1, q}, {Fe, - (mf + q)}])^2;

   (*optical dipole potential for each spin component*)
   pot = (3 π * c^2 * 3 * ΓYb1 / (2 * (2 π * c / (λYb1))^3)) *
      ((trs7 / Δ1) + (trs5 / Δ2) + (trs3 / Δ3));
   pot
 ]
(* Exact dipole potential using non-pertervative picture *)
αpolYbExact[Bfield_, δ_, mf_, q_] :=
 Module[{Δ1, Δ2, Δ3, Fe, Fg, trs7, trs5, trs3, pot},
   Δ1 = (2 π * δ * 10^9 - 2 π * μB0 * gFYb3P1[7/2] * Bfield * (mf + q) +
       2 π * μI0 * gIYb1S0 * 2 / 5 * (mf) * Bfield);
   (* detuning of beam, with respect to Fe=7/2 *)
   Δ2 = (2 π * δ * 10^9 - 2 π * μB0 * gFYb3P1[5/2] * Bfield * (mf + q) +
       2 π * μI0 * gIYb1S0 * 2 / 5 * (mf) * Bfield - 2 π * 4698 / u);
   (* detuning of beam, with respect to Fe=5/2 *)
   Δ3 = (2 π * δ * 10^9 - 2 π * μB0 * gFYb3P1[3/2] * Bfield * (mf + q) +
       2 π * μI0 * gIYb1S0 * 2 / 5 * (mf) * Bfield - 2 π * 6193 / u);
   (* detuning of beam, with respect to Fe=3/2 *)

   Fg = 5 / 2;
   (* transition strength *)
   Fe = 7 / 2;
   trs7 = 3 * (2 * Fg + 1) * (2 * Fe + 1) *
      (SixJSymbol[{1, 1, 0}, {0, 0, 1}])^2 * (SixJSymbol[{1, Fe, 5/2}, {Fg, 0, 1}])^2
      (ThreeJSymbol[{Fg, mf}, {1, q}, {Fe, - (mf + q)}])^2;
   Fe = 5 / 2;
   trs5 = 3 * (2 * Fg + 1) * (2 * Fe + 1) *
      (SixJSymbol[{1, 1, 0}, {0, 0, 1}])^2 * (SixJSymbol[{1, Fe, 5/2}, {Fg, 0, 1}])^2
      (ThreeJSymbol[{Fg, mf}, {1, q}, {Fe, - (mf + q)}])^2;
   Fe = 3 / 2;
   trs3 = 3 * (2 * Fg + 1) * (2 * Fe + 1) *
      (SixJSymbol[{1, 1, 0}, {0, 0, 1}])^2 * (SixJSymbol[{1, Fe, 5/2}, {Fg, 0, 1}])^2
      (ThreeJSymbol[{Fg, mf}, {1, q}, {Fe, - (mf + q)}])^2;

   (*optical dipole potential for each spin component*)

   pot = hbar / 2 * 3 * ((trs7 * Δ1 * Log[1 + (1 / (IsatYb1 * 10)) / (1 + 4 * (Δ1)^2 / ΓYb1^2)]) + (trs5 * Δ2 *
         Log[1 + (1 / (IsatYb1 * 10)) / (1 + 4 * (Δ2)^2 / ΓYb1^2)]) + (trs3 * Δ3 * Log[1 + (1 / (IsatYb1 * 10)) / (1 + 4 * (Δ3)^2 / ΓYb1^2)]));
   pot
 ]
I1 = Iellip[λYb1, 1 * 10^-6, 0, 0, 1, 0, 1, 0, 150 u, 1, 0, 0, 0];
BarChart[Table[(αpolYb[150, 1.876, mf, 1] + αpolYb[150, 1.876, mf, -1]) / 2 * I1 / h,
```
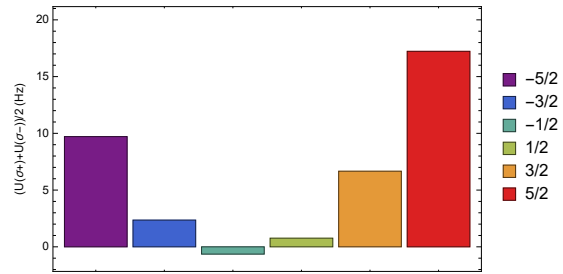
```
  {mf, -5/2, 5/2, 1}], Frame → True, PlotRange → {{0.5, 6.5}, {-1, 20}},
 FrameTicksStyle → {{Automatic, Automatic},
    {Directive[FontOpacity → 0, FontSize → 0], Automatic}}, ChartStyle → "Rainbow",
  ChartLegends → {"-5/2", "-3/2", "-1/2", "1/2", "3/2", "5/2"},
  FrameLabel → "(U(σ+)+U(σ-))/2 (Hz)"]
Off[ClebschGordan::phy]
```


Tunneling matix coefficient t

```
hbar = 1.054 × 10^-34;
h = 6.626 * 10^-34;
Er = h²/(2 m λ²);
λYb1 = 555.8 * 10⁻⁹; (*MOT beam*)
λYb2 = 398.9 * 10⁻⁹; (*Slowing beam*)
a0 = 5.292 * 10⁻¹¹;
m0 = 1.66 * 10⁻²⁷;
as = 199.4 a0; (*scattering length 173Yb-173Yb*)
mYb = 173 m0;
```

188

```
V = 6.25; (*lattice depth in Er*)
s = -V / 4; (*-V/4Er*)
ν[q_, n_] := q + Sign[q] (-1)^n * (n + Mod[n, 2]); (*characteristic exponent*)
BandE[q_, n_, s_] := MathieuCharacteristicA[ν[q, n], s] - 2 * s;
(*E^n_q as a function of qd/π where d=λ/2 is the lattice constant, in E_R*)
Plot[{BandE[q, 0, s], BandE[q, 1, s], BandE[q, 2, s],
  BandE[q, 3, s], BandE[q, 4, s], BandE[q, 5, s]}, {q, -0.999, 0.999},
 AxesOrigin → {-1, -0.1}, PlotRange → {-0.1, 30}, PlotStyle → Thick,
 Frame → True, FrameLabel → {"q (π/d)", "E (E_R)"}, AspectRatio → 1.6]
```


189
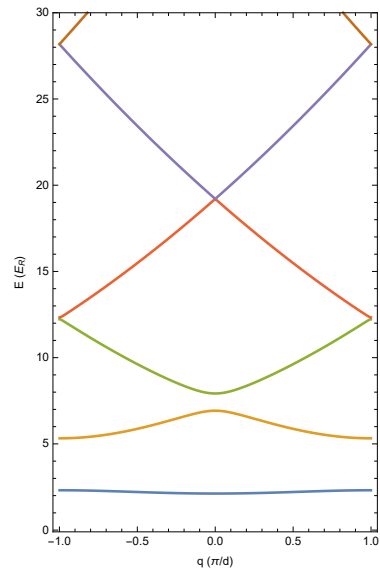
```mathematica
(*Wannier wave*)
L = 1 / Sqrt[4]; (*Normalizaing factor with
   Total[Table[Ws[1,x,0]^2,{x,-Infinity,Infinity,dx}]]*dx=1*)
d = 1; (*Lattice constant*)
ν[q_, n_] := q + Sign[q] (-1)^n * (n + Mod[n, 2]); (*characteristic exponent*)
Ws[Vlat_, x_, xi_] :=
 2 * L * NIntegrate[Cos[q * xi] MathieuC[MathieuCharacteristicA[ν[q, 0], -Vlat / 4],
      -Vlat / 4, π * x / d] + Sin[q * xi]
    MathieuS[MathieuCharacteristicA[ν[q, 0], -Vlat / 4], -Vlat / 4, π * x / d],
   {q, 0, 0.999999999}, AccuracyGoal → 9]
dx = 0.1; (*differential factor*)
Infty = 5 d;
V = 5.0;
WsDev[Vlat_, x_, xi_] :=
   (Ws[Vlat, x + dx, xi] - Ws[Vlat, x - dx, xi]) / 2 / dx / (π * d);
t1s = Sum[Ws[V, x, π * d] * ((WsDev[V, x + dx, 0] - WsDev[V, x - dx, 0]) / 2 / dx / (π * d) +
        V * Cos[π * x / d]^2 * Ws[V, x, 0]), {x, -Infty, Infty, dx}] * dx;
t1s * Er / h /. m → mYb /. λ → 532 * 10^-9 (* in Hz *)
```

263.695

초   록

위상이란 연속적인 변형에도 변하지 않는 시스템의 기하학적 속성이다. 예를 들어, 띠를 한 번 꼬아서 양 끝을 붙인 유명한 뫼비우스의 띠가 있다. 자르는 행위 없이, 어떠한 연속적인 변형도 뫼비우스의 띠의 꼬임을 제거할 수 없다. 여기서 꼬인 횟수는 "위상적 불변 수"로서, 시스템의 위상적인 질서를 특징짓는다. 최근에 이러한 위상적인 성질은 우주론부터 응집물리학 등에 이르기까지 현대 물리학에서 중요한 개념이 되었다. 특히, 고체 내 전자들의 경우, 특정 상황에서 블로흐 밴드가 위상적인 질서를 안정화시키는 유한한 위상 수를 가질 수 있다. 이 때 밴드 갭을 닫지 않는 이상 위상 수는 변하지 않는다. 놀랍게도, 이러한 물질의 위상적인 특성은 물질의 특별한 물리적인 성질이 미세한 세부 변화에 둔감하고 준정적인 변수 변화에 강력한 저항성을 가지게 한다. 따라서 위상적 물질은 새로운 종류의 물질이 될 후보로 꼽히고 있다. 양자 홀 효과의 발견 이래로, 이러한 아이디어는 지난 수십 년 동안 널리 연구되어 왔다.

양자 기체 시스템은 이러한 모델 해밀토니안을 고립되고 쉽게 조절가능하며 불순물 없이 실험해볼 수 있는 좋은 테스트 환경을 제공한다. 위상적인 물질에 대해 연구하기 위해, 우리는 2색 교차 쌍극자 트랩 내 173 이터븀 원자로 이루어진 $T/T_\mathrm{F} = 0.1$ 정도 온도의 페르미 축퇴 기체(DFG)를 25초 안에 생성할 수 있는 장치를 제작하였다. 이터븀 페르미온은 무거운 알칼리-토금속-류 원소로 라만 전이를 이용하여 인공 게이지 포텐셜을 생성하는데 유리한 조건을 제공한다. 첫 번째 연구로서, 스핀 편향된 샘플의 운동량 분해 라만 스펙트럼을 측정하였다. 특정 실험 조건에서, 라만 전이의 이중 공명 현상이 관찰되었고, 스펙트럼은 Autler-Townes 효과와 유사한 이중선 분열을 보여주었다.

위상적 물질을 연구하기 좋은 출발점은 Harper-Hofstadter (HH) 해밀토니안이다. 이 모델은 직교하는 자기장 아래의 사각 격자 내 전하를 띤 입자의

191

움직임을 기술한다. HH 해밀토니안을 다루기 위해, 3개의 다리로 이루어진 인공 홀 튜브가 1차원 광격자에 페르미온 173 이터븀 원자를 담아 순환적인 이맞는 라만 전이 연결을 통해 구현되었다. 인공 차원 프레임에서, 이것은 주기적인 경계 조건을 가지는 2차원 HH 해밀토니안 내 스핀없는 페르미온과 동일하다. 경계 조건이 주기적에서 열린 상태로 변화함에 따라 홀 튜브 시스템은 위상적인 상태 또는 일반적인 상태를 가진다. 시스템을 갑작스럽게 변화시켰을 때 나타나는 동역학으로부터, 홀 튜브 시스템의 밴드 구조를 조사하였으며, 밴드 갭이 닫히는 임계점은 홀 튜브 시스템에 대해 이론적으로 예측된 위상 상전이 지점과 일치하였다.

위상 물리학의 최전방 분야 중 하나는, 위상 물질 시스템 내 입자 간 상호작용의 효과이다. 위 연구를 입자 간 상호작용을 포함하는 방향으로 확장하기 위해, 173 이터븀 DFG의 상호결합 전이선을 이용한 해리 한계 근처의 광연합 (PA) 스펙트럼을 이용하여 원자 간 포텐셜 조사하였다. 본 연구에서는 $F = 5/2 \rightarrow F' = 7/2$ 기준으로 -1 GHz 까지의 원자 손실 스펙트럼으로부터, 80개의 PA 공명 상태를 관측하였다. 들뜬 분자 상태를 조사하기 위해, -0.8 GHz 근처의 PA 공명의 지만 효과와 원자 손실률을 조사하였고, 다양한 스핀 혼합 샘플을 이용하여 각 공명의 양자 수를 결정하였다.